TARGET-ORIENTED ELASTIC FULL-WAVEFORM INVERSION

A DISSERTATION
SUBMITTED TO THE DEPARTMENT OF GEOPHYSICS
AND THE COMMITTEE ON GRADUATE STUDIES
OF STANFORD UNIVERSITY
IN PARTIAL FULFILLMENT OF THE REQUIREMENTS
FOR THE DEGREE OF
DOCTOR OF PHILOSOPHY

Ettore Biondi
January 2021

I certify that I have read this dissertation and that, in my opinion, it is fully adequate in scope and quality as a dissertation for the degree of Doctor of Philosophy.

(Biondo Biondi) Principal Adviser

I certify that I have read this dissertation and that, in my opinion, it is fully adequate in scope and quality as a dissertation for the degree of Doctor of Philosophy.

(Howard Zebker)

I certify that I have read this dissertation and that, in my opinion, it is fully adequate in scope and quality as a dissertation for the degree of Doctor of Philosophy.

(Eric Dunham)

Approved for the Stanford University Committee on Graduate Studies

Abstract

Wave-equation-based parameter estimation techniques can retrieve accurate and high-resolution subsurface physical properties from seismic data acquired close to the surface of the Earth. In fact, multiple acoustic full-waveform inversion methods have been proposed over the years to retrieve the P-wave velocity of the subsurface. Moreover, researchers have extended full-waveform inversion approaches to estimate anisotropic and absorption parameters as well. Nowadays, some applications of elastic full-waveform inversion can also be found. However, given its prohibitive computational cost compared to the acoustic counterpart, elastic wave-equation inversion workflows still have limited applicability within seismic exploration datasets. To tackle this challenge, I propose a novel wave-equation-based elastic parameter estimation workflow based on wave-equation operators. I refer to the entire approach as target-oriented elastic full-waveform inversion. The method is composed of two steps. In the first one, I apply an extended linearized waveform inversion to the surface data. The obtained subsurface image is then employed to synthesize data as if they were acquired close to a target area. Finally, this dataset is inverted using an elastic full-waveform inversion workflow to estimate the subsurface elastic parameters. I demonstrate its efficacy on a 2D synthetic test and an ocean-bottom-node dataset acquired in the Gulf of Mexico, showing its ability to retrieve the elastic parameters of potential subsurface prospects. Compared to the elastic inversion of the surface dataset, the proposed method has a computational cost lower by two orders of magnitude.

Preface

The electronic version of this report[1] makes the input programs and applications available to the reader. The markings **ER**, **CR**, and **NR** are promises by the author about the reproducibility of each figure result. Reproducibility is a way of organizing computational research that allows both the author and the reader of a publication to verify the reported results. Reproducibility facilitates the transfer of knowledge within the Stanford Exploration Projection (SEP) and between SEP and its sponsors.

ER denotes Easily Reproducible and are the results of processing described in the paper. The author claims that you can reproduce such a figure from the programs, parameters, and makefiles input in the electronic document. The data must either be input in the electronic distribution, be easily available to all researchers (e.g., SEG-EAGE data sets), or be available in the SEP data library[2]. We assume you have a UNIX workstation with Fortran, Fortran90, C, X-Windows system and the software downloadable from our website (SEP makerules, SEPScons, SEPlib, and the SEP latex package), or other free software such as SU. Before the publication of the electronic document, someone other than the author tests the author's claim by destroying and rebuilding all ER figures. Some ER figures may not be reproducible by outsiders because they depend on data sets that are too large to distribute, or data that we do not have permission to redistribute but are in the SEP data library, or that the rules depend on commercial packages such as Matlab or Mathematica.

CR denotes Conditional Reproducibility. The author certifies that the commands are in place to reproduce the figure if certain resources are available. The primary reasons for the CR designation is that the processing requires 20 minutes or more.

NR denotes Non-Reproducible figures. SEP discourages authors from flagging their figures as NR except for figures that are used solely for motivation, comparison, or illustration of the theory, such as: artist drawings, scannings, or figures taken from SEP reports not by the authors or from non-SEP publications.

---

[1] http://sepwww.stanford.edu/public/docs/sep154

[2] http://sepwww.stanford.edu/public/docs/sepdatalib/toc_html/

Acknowledgments

Contents

List of Tables

List of Figures

Chapter 1

Introduction

Within the field of seismic data analysis, it has been recognized the advantage of relying on wave-equation-based methods to process recorded events (Williamson and Worthington, 1993). As a matter of fact, researchers have developed a variety of processing algorithms based on different approximations of a given wave equation (Berryhill, 1979; Ronen, 1987; Woodward, 1992; Kühl and Sacchi, 2003; Sava and Biondi, 2004; Shen, 2005).

One of the most studied approaches related to wave-equation data inversion is the method commonly called full-waveform inversion (FWI) (Tarantola, 1984). FWI can retrieve high-resolution subsurface parameters when an accurate initial guess is provided to an inversion workflow. Within the field of seismic exploration, FWI has been extensively investigated (Virieux and Operto, 2009), and it has been extended to multi-parametric wave equations (Operto et al., 2013). FWI has also demonstrated its potential within the field of global seismology (Fichtner et al., 2008), where multiple applications of this inversion framework have been reported (Fichtner, 2010). However, for seismic 3D exploration applications, its computational cost is still prohibitive when an elastic isotropic assumption is considered to predict the observed data (Alves, 2017).

Despite its high computational cost, elastic FWI has the ability to estimate accurate and data-consistent subsurface parameters (Brossier et al., 2009). These properties can be ultimately employed to characterize the rock-physicals parameters of the subsurface (Grana and Della Rossa, 2010). Thus, it is fundamental to enable the inversion of seismic data by an elastic FWI methodology; especially, given the increasing interest in understanding fine-scale physical phenomena (Lumley, 2010; Jaglan et al., 2015).

Limitations of Zoeppritz-based amplitude-versus-offset analysis and inversion

When reflected events are employed to estimate the elastic parameters of the subsurface, the standard processing tool is to follow an amplitude-versus-offset (AVO) analysis or inversion procedure (Yilmaz, 2001). This step commonly relies on the reflection coefficients predicted by the Zoeppritz equations to predict the amplitude response of the recorded data (Aki and Richards, 2002). However, this assumption limits the inversion capabilities for high-frequency data. I employ a simple example to highlight the Zoeppritz equation's limitation when fairly complex geological interfaces are reflecting energy back to the surface. I generate 2D elastic pressure data using one source and various receivers. I assume that the subsurface is composed of two layers with different variations in each of the three elastic parameters. Figure 1.1 shows the profiles of such model, where a decrease in S-wave and density is occurring, while the P-wave is increasing across the interface. Such elastic parameter variations correspond to an AVO class 4 (Castagna and Backus, 1993).

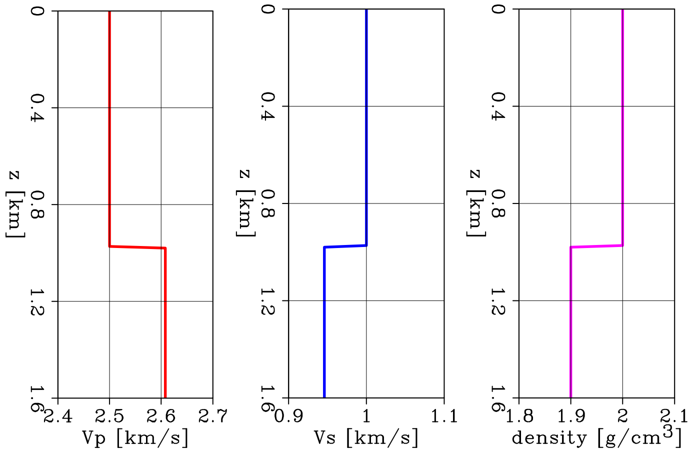

(a) (b) (c)

Figure 1.1: Elastic parameter profiles of the flat-interface model used to test the AVO response of elastic pressure data. The three panels show the (a) P-wave, (b) S-wave, and (c) density profiles, respectively. [**ER**]

I generate data considering two geological scenarios, one where the interface is flat and the other where the two layers are separated by a sinusoidal or wavy interface (Figure 1.2). The explosive source is placed at the surface at $x = 0$ m, and the various receivers are positioned with an increasing offset from it. As a source signature, I use a Ricker wavelet with a dominant frequency of 10 Hz. The panels in Figures 1.3a and 1.3b display the recorded pressure data in the two cases. In both panels, I have removed the direct arrival to display the single reflected event better. The amplitude of the reflected energy is increasing as the source-receiver distance is increasing. Additionally, other scattered events follow the main reflected event from the wavy interface (Figure 1.3b).

I compute the AVO response of the main reflected event using the Zoeppritz equation and is depicted by the blue curve in Figure 1.3c. As expected, the recorded amplitude variation extracted from the reflection in Figure 1.3a perfectly follows the predicted Zoeppritz response. On the other hand, the response extracted from the reflection in Figure 1.3b differs from the theoretical prediction.

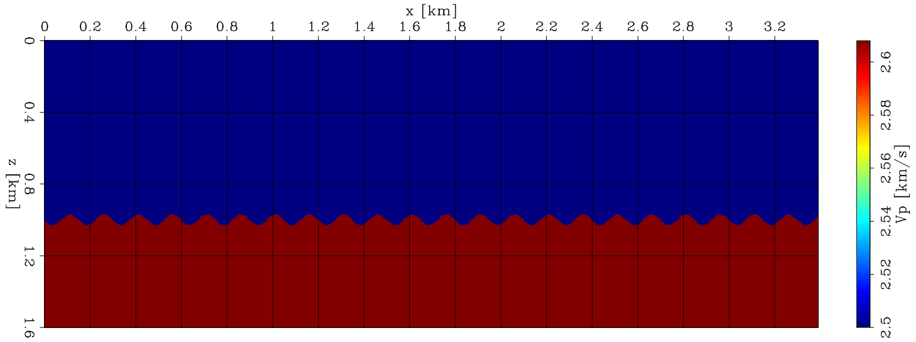

Figure 1.2: P-wave component of the elastic model in which the interface follows a sinusoidal pattern. [**ER**]

The features present on the interface, comparable with certain wavelengths of the signal, clearly affect the primary reflection's amplitude behavior. The amplitude response approaches the theoretical one by limiting this signal's frequency content to a maximum of 10 Hz. In this case, the interface effectively acts as flat because the interface variations are not comparable with the given injected wavelengths. However, this prediction error would prevent any inversion method to utilize the data's full bandwidth correctly. Therefore, any Zoeppritz-based approach's resolution capabilities are limited to retrieving the low-wavenumber component of the subsurface. On the contrary, an elastic FWI algorithm would correctly predict and use the entire signal's bandwidth.

Proposed solution

In most seismic exploration applications, high-resolution elastic parameters are necessary only within a limited portion of the subsurface (i.e., gas hazard, potential prospects, or known reservoirs). Hence, I propose a novel target-oriented elastic FWI algorithm based on the usage of the extended-image space. This image domain has been employed by many authors to invert for a subsurface migration velocity based on optimal focusing of the image when the correct velocity is used during migration (Symes and Kern, 1994; Yang and Sava, 2009; Alkhalifah, 2014; Biondi and Almomin, 2014). In other applications, a form of extended-image space based on ray parameter is used to generate angle gathers that preserve the amplitude information of the migrated events (Kuehl and Sacchi, 2002; Wang et al., 2005). The ability to preserve the amplitude behavior of primary reflected events allows for the analysis of the amplitude-versus-angle (AVA) information and its subsequent inversion to retrieve the elastic subsurface parameters (Schleicher et al., 1993; Albertin et al., 2004; Gray and Bleistein, 2009).

In the proposed approach, the elastic pressure data are employed within an extended linearized waveform inversion. The solution to this optimization problem is then used to synthesize a new dataset as if the acquisition geometry was placed in proximity of a target area; hence, effectively

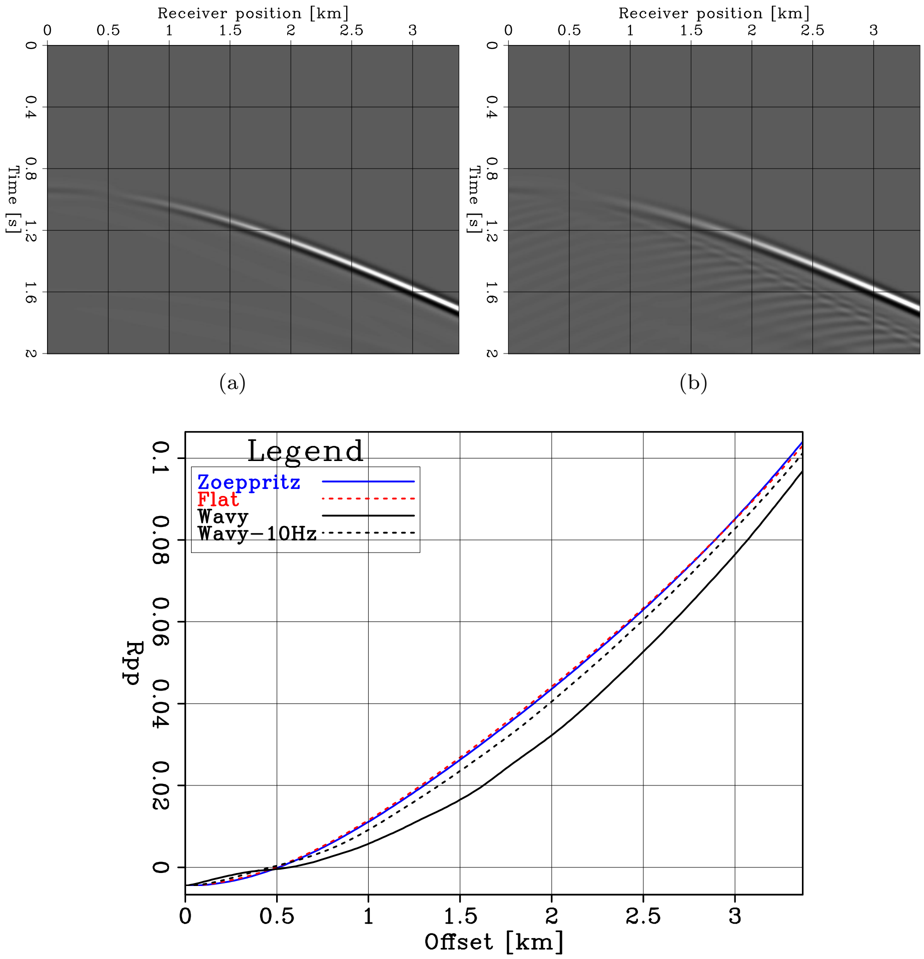

(a)

(b)

(c)

Figure 1.3: Elastic pressure reflected from the (a) flat and the (b) wavy interfaces, respectively. In both panels the direct arrival has been removed. (c) Comparison of the AVO responses extracted from the data against the theoretical Zoeppritz (blue curve). The red and solid black curves denote the amplitude variation extracted from the flat- and wavy-interface models, respectively. The dashed black curve is the AVO of the wavy-interface data but for a maximum frequency content of 10 Hz. [**ER**]

move the observed data from the surface to a new subsurface level. The process of moving the data from one acquisition depth to a new one is known as *redatuming* within the field of seismic exploration (Schuster and Zhou, 2006). The redatuming step permits to limit the simulation domain of an elastic FWI problem to a small region of the subsurface; thus, diminishing its overall computational cost and memory usage.

Thesis overview

I start by describing the theory of wave-equation modeling for the elastic and acoustic isotropic cases and derive the corresponding linearized wave-equation operators. I employ these non-linear and linear operators to define the linearized and full waveform inversion problems. Finally, I illustrate how an extended linearized waveform inversion procedure is employed to redatum the elastic data that are the input for an elastic FWI procedure to estimate the subsurface parameters of a target area.

Using various 2D synthetic examples, I first show the ability of an acoustic extended linearized waveform inversion to preserve the elastic amplitude variations of pressure data. These variations ultimately contain the information necessary to retrieve the subsurface elastic parameters. Then, I explain, using a simple example, how the extended space is used to perform the redatuming step of the proposed inversion workflow. Finally, I apply the target-oriented elastic FWI method to retrieve a gas-bearing sand lens's elastic properties and highlight the computational and memory cost-saving factors.

In the field-application chapter, I apply the entire inversion workflow to an active source survey acquired in the Gulf of Mexico. First, I estimate an accurate velocity model using an acoustic FWI process. I use the inverted velocity model to obtain an interpretable subsurface image on which I identify a potential prospect whose elastic parameters are unknown. I then employ the proposed target-oriented approach to this target and estimate its properties with a faction of the computational cost of applying an elastic FWI process to the entire dataset. The retrieved parameters are consistent with the existence of gas accumulation at the top of a potential reservoir.

Chapter 2

Theory

I describe the theory behind wave-equation-based imaging and inversion. I start by writing the acoustic and elastic isotropic wave equations for both continuous and discrete cases. Then, I derive the linearization of both wave equations and form the corresponding forward and adjoint Born operators. These matrices represent the fundamental operators employed within the imaging methods presented in this section. Moreover, using the solution to the isotropic wave equations and their linearization, I define the non-convex optimization problem called full-waveform inversion. Finally, I describe a redatuming technique based on an extended linearized waveform inversion approach, where surface data are used to reconstruct data generated by a subsurface target. Any redatuming technique aims to synthesize or reconstruct the data as if the data have been acquired by sources and receivers placed to a greater depth compared to the original one (Schuster and Zhou, 2006). Once the redatuming step is applied, the new dataset can be used to perform a waveform inversion of the elastic properties of a target area (Richard et al., 1994; Wapenaar, 2014; Ravasi, 2017; Guo and Alkhalifah, 2019; Garg and Verschuur, 2020). The advantage of performing a target-oriented inversion is the computational saving factor, compared to apply a waveform inversion process to the surface data, obtained by limiting the simulation domain to only the area of interest.

Table 2.1 displays the fundamental continuous wave-equation variables used within this section along with their units and dependency with respect to the spatial and time coordinates.

2.1 Wave-equation modeling

A common assumption when processing seismic data is to consider the subsurface as an elastic isotropic medium. Therefore, to predict or model seismic recording, I can solve the elastic isotropic

Table 2.1: Wave-equation variable naming and definitions.

Variable	**Name**	**Dependency**	**Units**
ρ	Density	space	kg/m^3
μ	Shear modulus	space	Pa
λ	Lamé parameter	space	Pa
v_i	Particle velocity	space and time	m/s
σ_{ij}	Stress-tensor component	space and time	Pa
f_i	Volumetric force	space and time	N/m^3
m_{ij}	Moment tensor component	space and time	Pa/s
p	Pressure field	space and time	Pa
K	Bulk modulus	space	Pa
s	Acoustic source	space and time	Pa/s^2

wave equation that is written as follows:

$$\begin{aligned}\rho(\mathbf{x})\frac{\partial v_i(\mathbf{x},t)}{\partial t} &= \frac{\partial \sigma_{ik}(\mathbf{x},t)}{\partial x_k} + f_i(\mathbf{x},t), \\ \frac{\partial \sigma_{ij}(\mathbf{x},t)}{\partial t} &= \lambda(\mathbf{x})\frac{\partial v_k(\mathbf{x},t)}{\partial x_k}\delta_{ij} + \mu(\mathbf{x})\left[\frac{\partial v_i(\mathbf{x},t)}{\partial x_j} + \frac{\partial v_j(\mathbf{x},t)}{\partial x_i}\right] + m_{ij}(\mathbf{x},t),\end{aligned} \tag{2.1}$$

where I employ the Einstein notation. The spatial and temporal coordinates are denoted by $\mathbf{x}$ and t, respectively, and δ_{ij} is the Kronecker delta. The subsurface is fully characterized by the three elastic parameters: density ρ, first Lamé parameter λ, and shear modulus μ. The wavefield variables in this equation are given by the particle velocities v_i and the stress tensor components σ_{ij}, which are symmetric (i.e., $\sigma_{ij} = \sigma_{ji}$) (Chadwick, 1976). The wave propagation is due to the presence of the source terms f_i and m_{ij} that represent a volumetric force field and the time derivative of the moment tensor, respectively (Aki and Richards, 2002). When the shear modulus is null (i.e., $\mu = 0$), the elastic wave equation simplifies to the acoustic isotropic form that can be written as the following partial differential equation (PDE):

$$\frac{\partial^2 p(\mathbf{x},t)}{\partial t^2} - \lambda(\mathbf{x})\nabla\cdot\frac{1}{\rho(\mathbf{x})}\nabla p(\mathbf{x},t) = s'(\mathbf{x},t), \tag{2.2}$$

where ∇ denotes the gradient operator, $\nabla\cdot$ is the divergence, and the pressure field p represents the symmetric component of the stress tensor. The source term s' is given by:

$$s'(\mathbf{x},t) = \frac{\partial m_{kk}(\mathbf{x},t)}{\partial t} + \frac{\partial}{\partial x_k}\left(\frac{f_k(\mathbf{x},t)}{\rho(\mathbf{x})}\right). \tag{2.3}$$

In most applications, the decomposition of source term is neglected and a single function is employed. If I consider only the symmetric component of the stress tensor, I can derive the same wave equation where λ becomes $K = \lambda + 2/3\mu$, which is referred to as bulk modulus. One common additional assumption for equation 2.2 is to consider the density function ρ to be spatially constant. Under this assumption, the wave equation simplifies even further and becomes:

$$\frac{1}{v^2(\mathbf{x})}\frac{\partial^2 p(\mathbf{x},t)}{\partial t^2} - \nabla^2 p(\mathbf{x},t) = s(\mathbf{x},t), \tag{2.4}$$

where v represents the acoustic wave speed and $s = s'/v^2$. In this approximation, the subsurface is fully characterized by a single parameter.

To model seismic recording it is commonly assumed that the source term (e.g., m_{ij} or s) is known. However, it can also be retrieved by applying an estimation technique (Song et al., 1995; Minson and Dreger, 2008). Moreover, within seismic exploration applications, the source term is commonly assumed to be a point source characterized by a source signature $w(t)$. For instance, the source term in equation 2.4 can be written as follows:

$$s(\mathbf{x},t) = \delta(\mathbf{x} - \mathbf{x}_s)w(t), \tag{2.5}$$

where δ denotes the Dirac delta, and $\mathbf{x}_s$ represents the source position. In field applications, the wavefield variables (e.g., p or v_i and σ_{ij}) are not known everywhere in the subsurface position $\mathbf{x}$, but they are sampled by recording devices, such as geophones or hydrophones. For examples, in the acoustic case, the recorded data are given by:

$$d(\mathbf{x}_r,t) = \int_\Omega \delta(\mathbf{x} - \mathbf{x}_r)p(\mathbf{x},t)\mathbf{dx}, \tag{2.6}$$

where $\mathbf{x}_r$ is the recording coordinates, and Ω is the propagation domain considered.

To solve any wave equation, I discretize the previous PDEs and use an explicit finite-difference (FD) approach. For the elastic case (equation 2.1), I employ a staggered-grid method (Virieux, 1986), while for the constant density acoustic wave equation, I follow a central-grid finite-difference scheme.

The discretization of the elastic 3D wave equation leads to the following linear system:

$$\begin{aligned} \mathbf{B}^{-1}\mathbf{D}_{t,\mathbf{v}}\mathbf{v} &= \mathbf{D}_{s,\boldsymbol{\sigma}}\boldsymbol{\sigma} + \mathbf{s}_f, \\ \mathbf{D}_{t,\boldsymbol{\sigma}}\boldsymbol{\sigma} &= \mathbf{C}\mathbf{D}_{s,\mathbf{v}}\mathbf{v} + \mathbf{s}_m, \end{aligned} \tag{2.7}$$

where particle velocities and stress components are written as the following vectors:

$$\mathbf{v} = \begin{bmatrix} \mathbf{v}_x & \mathbf{v}_y & \mathbf{v}_z \end{bmatrix}^T, \tag{2.8}$$

$$\boldsymbol{\sigma} = \begin{bmatrix} \boldsymbol{\sigma}_{xx} & \boldsymbol{\sigma}_{yy} & \boldsymbol{\sigma}_{zz} & \boldsymbol{\sigma}_{xz} & \boldsymbol{\sigma}_{xy} & \boldsymbol{\sigma}_{yz} \end{bmatrix}^T, \tag{2.9}$$

where ^{T} denotes the transposition operation. The source terms are given by the following vectors:

$$\mathbf{s}_f = \begin{bmatrix} \mathbf{f}_x & \mathbf{f}_y & \mathbf{f}_z \end{bmatrix}^T, \tag{2.10}$$

$$\mathbf{s}_m = \begin{bmatrix} \mathbf{m}_{xx} & \mathbf{m}_{yy} & \mathbf{m}_{zz} & \mathbf{m}_{xz} & \mathbf{m}_{xy} & \mathbf{m}_{yz} \end{bmatrix}^T. \tag{2.11}$$

The time derivative operators are written as follows:

$$\mathbf{D}_{t,\mathbf{v}} = \begin{bmatrix} \mathbf{D}_t & \mathbf{0} & \mathbf{0} \\ \mathbf{0} & \mathbf{D}_t & \mathbf{0} \\ \mathbf{0} & \mathbf{0} & \mathbf{D}_t \end{bmatrix}, \tag{2.12}$$

$$\mathbf{D}_{t,\boldsymbol{\sigma}} = \begin{bmatrix} \mathbf{D}_t & \mathbf{0} & \mathbf{0} & \mathbf{0} & \mathbf{0} & \mathbf{0} \\ \mathbf{0} & \mathbf{D}_t & \mathbf{0} & \mathbf{0} & \mathbf{0} & \mathbf{0} \\ \mathbf{0} & \mathbf{0} & \mathbf{D}_t & \mathbf{0} & \mathbf{0} & \mathbf{0} \\ \mathbf{0} & \mathbf{0} & \mathbf{0} & \mathbf{D}_t & \mathbf{0} & \mathbf{0} \\ \mathbf{0} & \mathbf{0} & \mathbf{0} & \mathbf{0} & \mathbf{D}_t & \mathbf{0} \\ \mathbf{0} & \mathbf{0} & \mathbf{0} & \mathbf{0} & \mathbf{0} & \mathbf{D}_t \end{bmatrix}, \tag{2.13}$$

where $\mathbf{D}_t$ is a central-difference time-derivative operator. The matrix $\mathbf{C}$ represents the stiffness tensor and is written as follows:

$$\mathbf{C} = \begin{bmatrix} \boldsymbol{\Lambda} + 2\boldsymbol{M} & \boldsymbol{\Lambda} & \boldsymbol{\Lambda} & \mathbf{0} & \mathbf{0} & \mathbf{0} \\ \boldsymbol{\Lambda} & \boldsymbol{\Lambda} + 2\boldsymbol{M} & \boldsymbol{\Lambda} & \mathbf{0} & \mathbf{0} & \mathbf{0} \\ \boldsymbol{\Lambda} & \boldsymbol{\Lambda} & \boldsymbol{\Lambda} + 2\boldsymbol{M} & \mathbf{0} & \mathbf{0} & \mathbf{0} \\ \mathbf{0} & \mathbf{0} & \mathbf{0} & \boldsymbol{M}_{xz} & \mathbf{0} & \mathbf{0} \\ \mathbf{0} & \mathbf{0} & \mathbf{0} & \mathbf{0} & \boldsymbol{M}_{xy} & \mathbf{0} \\ \mathbf{0} & \mathbf{0} & \mathbf{0} & \mathbf{0} & \mathbf{0} & \boldsymbol{M}_{yz} \end{bmatrix}. \tag{2.14}$$

and the inverse of the buoyancy matrix $\mathbf{B}$ is written as:

$$\mathbf{B}^{-1} = \begin{bmatrix} \mathbf{P}_x & \mathbf{0} & \mathbf{0} \\ \mathbf{0} & \mathbf{P}_y & \mathbf{0} \\ \mathbf{0} & \mathbf{0} & \mathbf{P}_z \end{bmatrix}, \tag{2.15}$$

where $\boldsymbol{\Lambda}$ and $\boldsymbol{M}$ are diagonal matrices containing repeated values of the discretized Lamé parameter and shear modulus $\boldsymbol{\lambda}$ and $\boldsymbol{\mu}$, respectively. The other diagonal matrices $\boldsymbol{M}_{ij}$ and $\mathbf{P}_i$ are constructed in a similar manner but using $\boldsymbol{\mu}_{ij}$ and $\boldsymbol{\rho}_i$, respectively. These latter vectors represent the discretized shear modulus and density staggered on the respective directions indicated by the subscripts, respectively. Figure 2.1 shows a diagram describing the staggered grids where each wavefield component and elastic parameter are defined. By employing a staggering operator $\mathbf{S}_i$, which shifts a given vector along the i axis (Moczo et al., 2002), I can define the staggered elastic parameters as:

$$\begin{aligned} \boldsymbol{\rho}_i &= \mathbf{S}_i\boldsymbol{\rho}, \\ \boldsymbol{\mu}_{ij} &= \mathbf{S}_i\mathbf{S}_j\boldsymbol{\mu}, \end{aligned} \tag{2.16}$$

which can be used to form the operators $\mathbf{B}$ and $\mathbf{C}$ from the central-grid parameters $\boldsymbol{\lambda}$, $\boldsymbol{\mu}$, and $\boldsymbol{\mu}$. With this definition of the staggered grids, the spatial derivative operators $\mathbf{D}_{s,\boldsymbol{\sigma}}$ and $\mathbf{D}_{s,\mathbf{v}}$ are written as follows:

$$\mathbf{D}_{s,\boldsymbol{\sigma}} = \begin{bmatrix} \mathbf{D}_x^- & \mathbf{0} & \mathbf{0} & \mathbf{D}_z^+ & \mathbf{D}_y^+ & \mathbf{0} \\ \mathbf{0} & \mathbf{D}_y^- & \mathbf{0} & \mathbf{0} & \mathbf{D}_x^+ & \mathbf{D}_z^+ \\ \mathbf{0} & \mathbf{0} & \mathbf{D}_z^- & \mathbf{D}_x^+ & \mathbf{0} & \mathbf{D}_y^+ \end{bmatrix}, \tag{2.17}$$

$$\mathbf{D}_{s,\mathbf{v}} = \begin{bmatrix} \mathbf{D}_x^+ & \mathbf{0} & \mathbf{0} \\ \mathbf{0} & \mathbf{D}_y^+ & \mathbf{0} \\ \mathbf{0} & \mathbf{0} & \mathbf{D}_z^+ \\ \mathbf{D}_z^- & \mathbf{0} & \mathbf{D}_x^- \\ \mathbf{D}_y^- & \mathbf{D}_x^- & \mathbf{0} \\ \mathbf{0} & \mathbf{D}_z^- & \mathbf{D}_y^- \end{bmatrix}, \tag{2.18}$$

where $\mathbf{D}_i^+$ and $\mathbf{D}_i^-$ are FD forward and backward spatial derivative operators along the i axis, respectively.

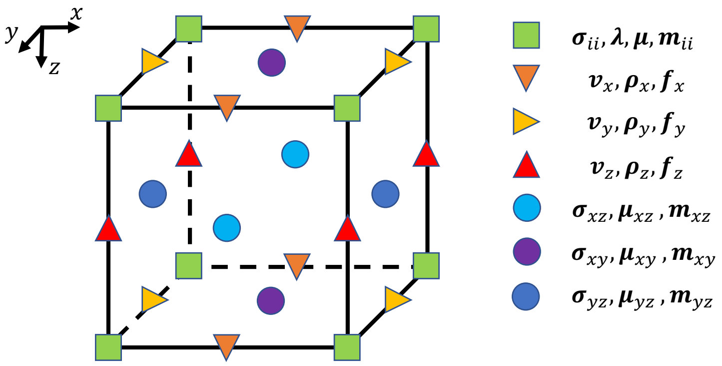

Figure 2.1: Diagram showing how each wavefield component and elastic parameter are distributed on the different grids within a 3D elastic staggered-grid scheme. [**NR**]

Equation 2.7 can be rewritten as the following linear system:

$$\mathbf{A}_{ela}(\boldsymbol{\lambda}, \boldsymbol{\mu}, \boldsymbol{\rho})\mathbf{w}_{ela} = \mathbf{s}_{ela}, \tag{2.19}$$

where the wavefield vector is defined as:

$$\mathbf{w}_{ela} = \begin{bmatrix} \mathbf{v} & \boldsymbol{\sigma} \end{bmatrix}^T, \tag{2.20}$$

and the source vector as:

$$\mathbf{s}_{ela} = \begin{bmatrix} \mathbf{s}_f & \mathbf{s}_m \end{bmatrix}^T. \tag{2.21}$$

The operator $\mathbf{A}_{ela}$ is written as the following matrix:

$$\mathbf{A}_{ela}(\boldsymbol{\lambda}, \boldsymbol{\mu}, \boldsymbol{\rho}) = \begin{bmatrix} \mathbf{B}^{-1}\mathbf{D}_{t,\mathbf{v}} & -\mathbf{D}_{s,\boldsymbol{\sigma}} \\ -\mathbf{C}\mathbf{D}_{s,\mathbf{v}} & \mathbf{D}_{t,\boldsymbol{\sigma}} \end{bmatrix}, \tag{2.22}$$

which non-linearly depends on the elastic parameters $\boldsymbol{\lambda}$, $\boldsymbol{\mu}$, and $\boldsymbol{\rho}$.

Under certain conditions, this operator represents a positive-definite matrix that can be solved by forward substitution when initial time-boundary conditions are assumed. Therefore, elastically propagating a source vector can be expressed as follows:

$$\mathbf{w}_{ela} = \mathbf{A}_{ela}^{-1}(\boldsymbol{\lambda}, \boldsymbol{\mu}, \boldsymbol{\rho})\mathbf{s}_{ela}, \tag{2.23}$$

which represents a linear operator with respect to the source term $\mathbf{s}_{ela}$. The elastic parameters $\boldsymbol{\lambda}, \boldsymbol{\mu}, \boldsymbol{\rho} \in \mathbb{R}^{N_m}$, with $N_m = N_x \times N_y \times N_z$, while the elastic wavefield and source vectors $\mathbf{w}_{ela}$ and $\mathbf{s}_{ela}$ belong to $\mathbb{R}^{N_w^{ela}}$ and $A_{ela} \in \mathbb{R}^{N_w^{ela} \times N_w^{ela}}$, with $N_w^{ela} = 9 \times N_m \times N_t$, where N_i represents the number of points along the i axis and N_t is the number of time samples.

Equation 2.23 also defines a non-linear function of the elastic parameters as follows:

$$\begin{aligned} \mathbf{f}_{ela}: \quad & \mathbb{R}^{3 \times N_m} && \mapsto \mathbb{R}^{N_w^{ela}} \\ & \boldsymbol{\lambda}, \boldsymbol{\mu}, \boldsymbol{\rho} && \mapsto \mathbf{f}_{ela}(\boldsymbol{\lambda}, \boldsymbol{\mu}, \boldsymbol{\rho}). \end{aligned} \tag{2.24}$$

For the acoustic constant-density wave equation, I discretize equation 2.4 using a central-difference scheme and write the following expression:

$$\left[\mathbf{V}^{-2}\mathbf{D}_t^2 - \boldsymbol{\nabla}^2\right] \mathbf{p} = \mathbf{s}_{aco}, \tag{2.25}$$

where $\mathbf{D}_t^2$ is a second-order central-difference time derivative operator, $\boldsymbol{\nabla}^2$ is a high-order Laplacian operator, $\mathbf{V}$ is a diagonal matrix that depends on the velocity vector $\mathbf{v}$, and the pressure field $\mathbf{p}$ and the acoustic source vector $\mathbf{s}_{aco}$ belong to $\mathbb{R}^{N_m^{aco}}$, with $N_m^{aco} = N_m \times N_t$. Similarly to equation 2.23, the acoustic propagation of an acoustic source vector can be written as:

$$\mathbf{p} = \mathbf{A}_{aco}^{-1}(\mathbf{v})\mathbf{s}_{aco}, \tag{2.26}$$

where $\mathbf{A}_{aco}(\mathbf{v}) = \left[\mathbf{V}^{-2}\mathbf{D}_t^2 - \boldsymbol{\nabla}^2\right]$, which can also be inverted using a forward substitution scheme when initial time-boundary conditions are assumed. Finally, I define a non-linear function with respect to the velocity vector as follows:

$$\begin{aligned} \mathbf{f}_{aco}: \quad & \mathbb{R}^{N_m} && \mapsto \mathbb{R}^{N_w^{aco}} \\ & \mathbf{v} && \mapsto \mathbf{f}_{aco}(\mathbf{v}). \end{aligned} \tag{2.27}$$

I represent the data sampling operation of equation 2.6 by using a restriction operator K applied to $\mathbf{f}_{aco}$. Thus, I can write the modeling of acoustic data for a single source as follows:

$$\mathbf{d}_{aco}(\mathbf{v}) = \mathbf{K}\mathbf{f}_{aco}(\mathbf{v}), \tag{2.28}$$

where $\mathbf{d}_{aco} \in \mathbb{R}^{N_d}$ and $\mathbf{K} \in \mathbb{R}^{N_d \times N_w^{aco}}$, with $N_d = N_r \times N_t$. N_d represents the discrete number of spatial points of the wavefield $\mathbf{p}$. This sampling operation can be a be performed by using Kronecker deltas or through discretization of the delta function (Fichtner, 2010).

When dealing with the elastic wave equation, the data sampling is performed in a similar fashion.

For instance, three-component (3-C) geophone is represented as:

$$\mathbf{d}_{ela}^{geo}(\boldsymbol{\lambda}, \boldsymbol{\mu}, \boldsymbol{\rho}) = \mathbf{K}_{geo}\mathbf{f}_{ela}(\boldsymbol{\lambda}, \boldsymbol{\mu}, \boldsymbol{\rho}), \tag{2.29}$$

where:

$$\mathbf{K}_{geo} = \begin{bmatrix} \textsc{k} & \mathbf{0} & \mathbf{0} & \mathbf{0} & \mathbf{0} & \mathbf{0} & \mathbf{0} & \mathbf{0} & \mathbf{0} \\ \mathbf{0} & \textsc{k} & \mathbf{0} & \mathbf{0} & \mathbf{0} & \mathbf{0} & \mathbf{0} & \mathbf{0} & \mathbf{0} \\ \mathbf{0} & \mathbf{0} & \textsc{k} & \mathbf{0} & \mathbf{0} & \mathbf{0} & \mathbf{0} & \mathbf{0} & \mathbf{0} \end{bmatrix}. \tag{2.30}$$

On the other hand, the recording of pressure data is expressed as:

$$\mathbf{d}_{ela}^{p}(\boldsymbol{\lambda}, \boldsymbol{\mu}, \boldsymbol{\rho}) = \mathbf{K}_{p}\mathbf{f}_{ela}(\boldsymbol{\lambda}, \boldsymbol{\mu}, \boldsymbol{\rho}), \tag{2.31}$$

with:

$$\mathbf{K}_{p} = \frac{1}{3}\begin{bmatrix} \mathbf{0} & \mathbf{0} & \mathbf{0} & \textsc{k} & \textsc{k} & \textsc{k} & \mathbf{0} & \mathbf{0} & \mathbf{0} \end{bmatrix}. \tag{2.32}$$

The extension of the previously defined non-linear operators when multiple sources are employed is performed by simply defining the following vector:

$$\begin{bmatrix} \mathbf{d}_1 \\ \vdots \\ \mathbf{d}_{N_s} \end{bmatrix} = \begin{bmatrix} \mathbf{K}_1\mathbf{f}_1(\mathbf{m}) \\ \vdots \\ \mathbf{K}_{N_s}\mathbf{f}_{N_s}(\mathbf{m}) \end{bmatrix}, \tag{2.33}$$

where N_s represents the number of sources, $\mathbf{m}$ is the vector of the subsurface parameters, and K_i and $\mathbf{f}_i$ are the sampling and modeling operators for the i-th source. In the following discussion, I refer to the single-shot case but it is trivial to extend to the multiple source using the vector defined in equation 2.33.

2.2 Wave-equation-based imaging and inversion

The theory of any wave-equation-based imaging is constructed on different forms of linearization of a considered wave equation. I first derive the linearized forms of the acoustic and elastic wave equations and show how their linearized forms are used to construct the corresponding Born operators. Then, by modifying the imaging condition for the acoustic case, I describe how extended images are obtained from seismic data by means of an extended adjoint Born operator. Finally, using the derived Born operators, I define the convex inverse problem known as linearized waveform inversion or least-squares reverse time migration (LSRTM) (Baysal et al., 1983).

2.2.1 Linearized wave equations

I begin by deriving the linearization of the acoustic wave equation using a perturbative approach. I then proceed by linearizing the elastic isotropic case by employing the same strategy.

Acoustic linearized wave equation

To linearize the acoustic wave equation I add a velocity perturbation δv to a velocity model v_0. Thus, I can write equation 2.4 as follows:

$$[v_0(\mathbf{x}) + \delta v(\mathbf{x})]^{-2} \frac{\partial^2 [p_0(\mathbf{x},t) + \delta p(\mathbf{x},t)]}{\partial t^2} - \nabla^2 [p_0(\mathbf{x},t) + \delta p(\mathbf{x},t)] = s(\mathbf{x},t), \tag{2.34}$$

where the background pressure field p_0 is perturbed by the field δp. The expansion of equation 2.34 yields:

$$\frac{1}{v_0^2(\mathbf{x})} \frac{\partial^2 p_0(\mathbf{x},t)}{\partial t^2} - \nabla^2 p_0(\mathbf{x},t) = s(\mathbf{x},t), \tag{2.35}$$

$$\frac{1}{v_0^2(\mathbf{x})} \frac{\partial^2 \delta p(\mathbf{x},t)}{\partial t^2} - \nabla^2 \delta p(\mathbf{x},t) = -\frac{2\delta v(\mathbf{x})}{v_0^3(\mathbf{x})} \frac{\partial^2 p_0(\mathbf{x},t)}{\partial t^2}, \tag{2.36}$$

where I neglected the higher-order terms. Equation 2.36 linearly relates a perturbation of the velocity δv with a perturbation in the pressure field δp, which in turn results in a perturbation of the recorded data δd as follows:

$$\delta d(\mathbf{x}_r, t) = \int_\Omega \delta(\mathbf{x} - \mathbf{x}_r) \delta p(\mathbf{x},t) \mathbf{dx}. \tag{2.37}$$

By discretizing equations 2.36 and 2.37, I can write the following linear operator:

$$\Delta \mathbf{d}_{aco}(\mathbf{v}_0) = \mathbf{K} \mathbf{A}_{aco}^{-1}(\mathbf{v}_0) \mathbf{P}_0(\mathbf{v}_0) \Delta \mathbf{v}, \tag{2.38}$$

that maps a discrete perturbation of the velocity $\Delta \mathbf{v}$ into a perturbation into the data space $\Delta \mathbf{d}$ and is based on the background velocity vector $\mathbf{v}_0$. The matrix $\mathbf{P}_0(\mathbf{v}) \in \mathbb{R}^{N_w^{aco} \times N_m}$ represents the discretization of the term $-2v_0^{-3}(\mathbf{x})\ddot{p_0}(\mathbf{x},t)$, where $\ddot{}$ denotes the second-order time derivative of a function. This operator is based on the discretized solution $\mathbf{p}_0$ of equation 2.35 , which is given by:

$$\mathbf{p}_0 = \mathbf{A}_{aco}^{-1}(\mathbf{v}_0) \mathbf{s}_{aco}. \tag{2.39}$$

In the seismic-exploration literature, the matrix product of equation 2.38 is commonly referred to as Born operator and is written as follows:

$$\mathbf{B}_{aco}(\mathbf{v}) = \mathbf{K}\mathbf{A}_{aco}^{-1}(\mathbf{v})\mathbf{P}_0(\mathbf{v}), \tag{2.40}$$

with $\mathbf{B}_{aco}(\mathbf{v}) \in \mathbb{R}^{N_d \times N_m}$.

Elastic linearized wave equation

To derive the linearized elastic wave-equation I follow the same approach. The perturbation of the elastic parameters λ, μ, and ρ of equation 2.1 yields:

$$\begin{aligned}
(\rho_0 + \delta\rho)\left(\frac{\partial v_{0,i}}{\partial t} + \frac{\partial \delta v_i}{\partial t}\right) &= \frac{\partial \sigma_{0,ij}}{\partial x_j} + \frac{\partial \delta\sigma_{ij}}{\partial x_j} + f_i, & (2.41)\\
\frac{\partial \sigma_{0,ij}}{\partial t} + \frac{\partial \delta\sigma_{ij}}{\partial t} &= (\lambda_0 + \delta\lambda)\left(\frac{\partial v_{0,k}}{\partial x_k} + \frac{\partial \delta v_k}{\partial x_k}\right)\delta_{ij} & (2.42)\\
&+ (\mu_0 + \delta\mu)\left(\frac{\partial v_{0,i}}{\partial x_j} + \frac{\partial \delta v_i}{\partial x_j} + \frac{\partial v_{0,j}}{\partial x_i} + \frac{\partial \delta v_j}{\partial x_i}\right)\\
&+ m_{ij}
\end{aligned}$$

where I dropped the function dependency and λ_0, μ_0, and ρ_0 are the background elastic parameters, while $\delta\lambda$, $\delta\mu$, and $\delta\rho$ are their corresponding perturbations. The background elastic fields $v_{0,i}$ and $\sigma_{0,ij}$ are perturbed by the fields δv_i and $\delta\sigma_{ij}$, respectively. By expanding these equations and reordering their terms, I write the following system of equations:

$$\begin{aligned}
\rho_0 \frac{\partial v_{0,i}}{\partial t} &= \frac{\partial \sigma_{0,ij}}{\partial x_j} + f_i, & (2.43)\\
\frac{\partial \sigma_{0,ij}}{\partial t} &= \lambda_0 \frac{\partial v_{0,k}}{\partial x_k}\delta_{ij} + \mu_0\left(\frac{\partial v_{0,i}}{\partial x_j} + \frac{\partial v_{0,j}}{\partial x_i}\right) + m_{ij}\\
\rho_0 \frac{\partial \delta v_i}{\partial t} &= \frac{\partial \delta\sigma_{ij}}{\partial x_j} - \delta\rho_0 \frac{\partial v_{0,i}}{\partial t}, & (2.44)\\
\frac{\partial \delta\sigma_{ij}}{\partial t} &= \lambda_0 \frac{\partial \delta v_k}{\partial x_k}\delta_{ij} + \mu_0\left(\frac{\partial \delta v_i}{\partial x_j} + \frac{\partial \delta v_j}{\partial x_i}\right) + \delta\lambda \frac{\partial v_{0,k}}{\partial x_k}\delta_{ij} + \delta\mu\left(\frac{\partial v_{0,i}}{\partial x_j} + \frac{\partial v_{0,j}}{\partial x_i}\right)
\end{aligned}$$

where the higher-order terms have been neglected. The discrete solution to the previous system of equations can be written as follows:

$$\mathbf{w}_{0,ela} = A_{ela}^{-1}(\boldsymbol{\lambda}_0, \boldsymbol{\mu}_0, \boldsymbol{\rho}_0)\mathbf{s}_{ela}, \tag{2.45}$$

$$\Delta\mathbf{w}_{ela} = \mathbf{A}_{ela}^{-1}(\boldsymbol{\lambda}_0, \boldsymbol{\mu}_0, \boldsymbol{\rho}_0)\mathbf{W}_{ela}(\boldsymbol{\lambda}_0, \boldsymbol{\mu}_0, \boldsymbol{\rho}_0)\mathbf{S}\Delta\mathbf{m}_{ela}, \tag{2.46}$$

where $\boldsymbol{\lambda}_0$, $\boldsymbol{\mu}_0$, and $\boldsymbol{\rho}_0$ represent the elastic background parameters and the elastic perturbations $\Delta\boldsymbol{\lambda}$, $\Delta\boldsymbol{\mu}$, and $\Delta\boldsymbol{\rho}$ are placed within the vector:

$$\Delta\mathbf{m}_{ela} = \begin{bmatrix} \Delta\boldsymbol{\lambda} & \Delta\boldsymbol{\mu} & \Delta\boldsymbol{\rho} \end{bmatrix}^T . \tag{2.47}$$

The matrix $\mathbf{W}_{ela}$ is constructed using the elastic background field $\mathbf{w}_{0,ela}$ as follows:

$$\mathbf{W}_{ela} = \begin{bmatrix} -\dot{\mathbf{V}}_x & \mathbf{0} & \mathbf{0} & \mathbf{0} & \mathbf{0} & \mathbf{0} & \mathbf{0} & \mathbf{0} \\ \mathbf{0} & -\dot{\mathbf{V}}_y & \mathbf{0} & \mathbf{0} & \mathbf{0} & \mathbf{0} & \mathbf{0} & \mathbf{0} \\ \mathbf{0} & \mathbf{0} & -\dot{\mathbf{V}}_z & \mathbf{0} & \mathbf{0} & \mathbf{0} & \mathbf{0} & \mathbf{0} \\ \mathbf{0} & \mathbf{0} & \mathbf{0} & (\mathbf{V}_x^{dx} + \mathbf{V}_y^{dy} + \mathbf{V}_z^{dz}) & 2\mathbf{V}_x^{dx} & \mathbf{0} & \mathbf{0} & \mathbf{0} \\ \mathbf{0} & \mathbf{0} & \mathbf{0} & (\mathbf{V}_x^{dx} + \mathbf{V}_y^{dy} + \mathbf{V}_z^{dz}) & 2\mathbf{V}_y^{dy} & \mathbf{0} & \mathbf{0} & \mathbf{0} \\ \mathbf{0} & \mathbf{0} & \mathbf{0} & (\mathbf{V}_x^{dx} + \mathbf{V}_y^{dy} + \mathbf{V}_z^{dz}) & 2\mathbf{V}_z^{dz} & \mathbf{0} & \mathbf{0} & \mathbf{0} \\ \mathbf{0} & \mathbf{0} & \mathbf{0} & \mathbf{0} & \mathbf{0} & 2(\mathbf{V}_x^{dz} + \mathbf{V}_z^{dx}) & \mathbf{0} & \mathbf{0} \\ \mathbf{0} & \mathbf{0} & \mathbf{0} & \mathbf{0} & \mathbf{0} & \mathbf{0} & 2(\mathbf{V}_x^{dy} + \mathbf{V}_y^{dx}) & \mathbf{0} \\ \mathbf{0} & \mathbf{0} & \mathbf{0} & \mathbf{0} & \mathbf{0} & \mathbf{0} & \mathbf{0} & 2(\mathbf{V}_y^{dz} + \mathbf{V}_z^{dy}) \end{bmatrix}, \tag{2.48}$$

where $\dot{\mathbf{V}}_i$ and $\mathbf{V}_i^{dj}$ are matrices containing the time derivative and spatial derivatives along the j-th axis of the particle velocity v_i. The scattering matrix $\mathbf{W}_{0,ela}$ shows that only the background particle velocities must be stored during the computation of the elastic field perturbation $\Delta\mathbf{w}_{ela}$. The matrix staggering $\mathbf{S}$ is necessary because of the usage of the staggering-grid approach. The operators composing this matrix is formed by following Figure 2.1 and is written as:

$$\mathbf{S} = \begin{bmatrix} \mathbf{0} & \mathbf{0} & \mathbf{S}_x \\ \mathbf{0} & \mathbf{0} & \mathbf{S}_y \\ \mathbf{0} & \mathbf{0} & \mathbf{S}_z \\ \mathbf{I} & \mathbf{0} & \mathbf{0} \\ \mathbf{0} & \mathbf{I} & \mathbf{0} \\ \mathbf{0} & \mathbf{S}_x\mathbf{S}_z & \mathbf{0} \\ \mathbf{0} & \mathbf{S}_x\mathbf{S}_y & \mathbf{0} \\ \mathbf{0} & \mathbf{S}_y\mathbf{S}_z & \mathbf{0} \end{bmatrix} . \tag{2.49}$$

Depending on the recorded data type, I can write the data perturbation vector by applying any sampling operator defined in equations 2.30 and 2.32 to equation 2.46. For instance, the elastic pressude data perturbation can be written as

$$\mathbf{B}_{ela}(\mathbf{m}_{ela}) = \mathbf{K}_p \mathbf{A}_{ela}^{-1}(\mathbf{m}_{ela})\mathbf{W}_{ela}(\mathbf{m}_{ela})\mathbf{S}, \tag{2.50}$$

where $\mathbf{m}_{ela} \in \mathbb{R}^{N_m^{ela}}$, with $N_m^{ela} = 3 \times N_m$, and is defined as:

$$\mathbf{m}_{ela} = \begin{bmatrix} \boldsymbol{\lambda} & \boldsymbol{\mu} & \boldsymbol{\rho} \end{bmatrix}^T. \tag{2.51}$$

Thus, $\mathbf{B}_{ela} \in \mathbb{R}^{N_d \times N_m^{ela}}$. Furthermore, by following the previously mentioned naming convention, I call $\mathbf{B}_{ela}$ the elastic Born operator for pressure data.

2.2.2 Wave-equation imaging

Conventional imaging

Using the acoustic and elastic Born operators, I can define the process of creating a seismic image of the subsurface using wave-equation-based migration methods (Mulder and Plessix, 2004). In this work, the imaging process is performed by applying the adjoint Born operator to the observed pressure data $\mathbf{d}_{obs}$. When the acoustic constant-density wave-equation is used during the migration process, the subsurface image $\mathbf{m}_a$ is obtained as follows:

$$\mathbf{m}_a = \mathbf{B}_{aco}^* \mathbf{d}_{obs} = \mathbf{P}_0^* (\mathbf{A}_{aco}^*)^{-1} \mathbf{K}^* \mathbf{d}_{obs}, \tag{2.52}$$

where * denotes the adjoint operation and the non-linear dependency on the velocity model $\mathbf{v}$ has been dropped. In this process, the observed data are used as the forcing term of the adjoint wave equation and is written as follows:

$$\mathbf{A}_{aco}^* \mathbf{q} = \left[\mathbf{V}^{-2}\mathbf{D}_t^2 - \boldsymbol{\nabla}^2\right]^* \mathbf{q} = \mathbf{K}^* \mathbf{d}_{obs}, \tag{2.53}$$

where $\mathbf{q}$ is commonly referred to as adjoint or receiver wavefield. As explained in Appendix A, depending on the assumed time and spatial boundary conditions the square matrix $\mathbf{A}_{aco}$ is lower triangular or symmetric (i.e., $\mathbf{A}_{aco} = \mathbf{A}_{aco}^*$). Finally, to form the image $\mathbf{m}_a$, the operator $\mathbf{P}_0$ is then applied to the adjoint wavefield $\mathbf{q}$. In the continuous case, this operator is represented by the following relation:

$$m(\mathbf{x}) = -2v_0^{-3}(\mathbf{x}) \int_\Gamma \ddot{p}_0(\mathbf{x}, t) q(\mathbf{x}, t) dt, \tag{2.54}$$

where Γ represents the time interval of the field q and p_0. Thus, the image m is formed by computing the zero-lag cross-correlation between two pressure fields. In a similar fashion, I define the same process for the elastic Born operator defined in equation 2.50:

$$\mathbf{m}_e = \mathbf{B}^*_{ela}\mathbf{d}_{obs} = \mathbf{S}^*\mathbf{W}^*_{ela}(\mathbf{A}^*_{ela})^{-1}\mathbf{K}^*_p\mathbf{d}_{obs}, \tag{2.55}$$

where $\mathbf{m}_e$ represents the elastic image of the subsurface and the adjoint elastic wave equation $\mathbf{A}^*_{ela}$ is written as follows (Alves, 2017):

$$\mathbf{A}^*_{ela} = \begin{bmatrix} \mathbf{B}^{-1}\mathbf{D}^*_{t,\mathbf{v}} & -\mathbf{D}^*_{s,\mathbf{v}}\mathbf{C} \\ -\mathbf{D}^*_{s,\boldsymbol{\sigma}} & \mathbf{D}_{t,\boldsymbol{\sigma}} \end{bmatrix}. \tag{2.56}$$

Under certain spatial boundary conditions, $\mathbf{D}^*_{s,\boldsymbol{\sigma}} = -\mathbf{D}_{s,\mathbf{v}}$ and $\mathbf{D}^*_{s,\mathbf{v}} = -\mathbf{D}_{s,\boldsymbol{\sigma}}$.

Extended imaging

The imaging condition of equation 2.54 can be modified to allow additional degree of freedom. When this modification is introduced, the subsurface image is referred to as an extended image (Symes and Kern, 1994; Symes, 2008; Biondi and Almomin, 2014). This extended-image domain has been employed by many authors to invert for the subsurface velocity based on the optimal focusing of an image when the correct velocity is used during the migration process (Symes and Carazzone, 1991; Sava and Biondi, 2004; Shen, 2005). The imaging condition for the extension called subsurface offsets is written as follow:

$$\tilde{m}_h(\mathbf{x},\mathbf{h}) = -2v_0^{-3}(\mathbf{x}) \int_\Gamma \ddot{p}_0(\mathbf{x}-\mathbf{h},t)q(\mathbf{x}+\mathbf{h},t)dt, \tag{2.57}$$

where $\tilde{m}_h$ represents the extended image and $\mathbf{h}$ the subsurface offset variable (Rickett and Sava, 2002). By using this imaging condition, I can define the extended Born operator $\tilde{\mathbf{B}}_{aco}$ as follows:

$$\tilde{\mathbf{B}}_{aco} = \mathbf{K}\mathbf{A}^{-1}_{aco}\tilde{P}_0, \tag{2.58}$$

where $\tilde{\mathbf{B}}_{aco} \in \mathbb{R}^{N_d \times \tilde{N}^{aco}_m}$, with $\tilde{N}^{aco}_m = N^{aco}_m \times N_h$ in which N_h is the is number of discrete points along the extended axis. The matrix $\tilde{P}_0$ represents the discretization of the subsurface-offset scattering conditions, which is given by:

$$q(\mathbf{x},t) = -2v_0^{-3}(\mathbf{x}) \int_{\Omega_h} \ddot{p}_0(\mathbf{x}-2\mathbf{h},t)\tilde{m}_h(\mathbf{x}-\mathbf{h},\mathbf{h})\mathbf{dh}, \tag{2.59}$$

where Ω_h represents the domain of $\mathbf{h}$.

The extended image in the subsurface-offset domain can be mapped into the subsurface-angle domain by applying the following transformation (Sava and Fomel, 2003):

$$\tilde{m}_{\gamma}(x, y, z, \gamma_x, \gamma_y) = \int_{\Omega_h} \tilde{m}_h(x, y, z + \tan(\gamma_x)h_x + \tan(\gamma_y)h_y, h_x, h_y)dh_x dh_y, \tag{2.60}$$

where h_x and h_y represent the subsurface-offset axis variables and γ_i is the angle between the integration plane and the axis h_i. Equation 2.60 represents a 3D Radon transform (Averbuch and Shkolnisky, 2003) and can also be written in terms of a dipping angle γ and an azimuth angle ϕ as follows (Biondi and Tisserant, 2004):

$$\tilde{m}_{\gamma}(x, y, z, \gamma, \phi) = \int_{\Omega_h} \tilde{m}_h(x, y, z + \tan(\gamma)[\cos(\phi)h_x - \sin(\phi)h_y], h_x, h_y)dh_x dh_y. \tag{2.61}$$

Additionally, under certain conditions, Biondi and Tisserant (2004) demonstrate that γ represent the reflection angle for a direction defined by the azimuth angle ϕ. In Appendix B, I derive the 2D and 3D forward and adjoint transformations as well as the corresponding pseudo-inverse operators.

2.2.3 Linearized waveform inversion

Using the Born operators or linearized wave equations, I define a wave-equation imaging process by solving the following convex inverse problem:

$$\mathbf{m}_{opt} = \underset{\mathbf{m}}{\operatorname{argmin}} \frac{1}{2}\|\mathbf{B}\mathbf{m} - \mathbf{d}_{mig}\|_2^2, \tag{2.62}$$

where $\mathbf{B}$ can be an elastic or acoustic or extended Born operator, $\mathbf{d}_{mig}$ represents a subset of the observed data (e.g., the reflected events), and $\mathbf{m}$ is the migrated image. The goal is to retrieve an image of the interfaces between rock layers of the subsurface $\mathbf{m}_{opt}$ from seismograms recorded at the surface $\mathbf{d}_{mig}$. Since this migration process is performed using the linearization of a wave equation and the full bandwidth of the data is considered, it is also referred to as linearized waveform inversion (Østmo et al., 2002). The solution to this problem can be also written using the following closed-form equation:

$$\mathbf{m}_{opt} = (\mathbf{B}^*\mathbf{B})^{-1}\mathbf{B}^*\mathbf{d}_{mig}. \tag{2.63}$$

Despite the simplicity of the previous equation, the solution to the problem posed in equation 2.62 is computationally demanding and its Hessian is often singular and ill-conditioned. The matrix $\mathbf{B}^*\mathbf{B}$ easily reaches the billions of rows and columns; especially, in the 3D case. Therefore, to solve this problem, one must rely on iterative solvers for linear problems (Kelley, 1999; Nocedal and Wright, 2006). Moreover, when certain acquisition geometries are considered or complex geological scenarios are explored (e.g., underneath a salt body), then additional regularization terms must be added to improve the quality of the subsurface image. For instance, when an extended Born modeling operator is considered, then the focus of the optimal image $\tilde{\mathbf{m}}_{opt}$ can be improved by solving the following regularized problem:

$$\tilde{\mathbf{m}}_{opt} = \underset{\tilde{\mathbf{m}}}{\operatorname{argmin}} \frac{1}{2}\|\tilde{\mathbf{B}}_{aco}\tilde{\mathbf{m}} - \mathbf{d}_{mig}\|_2^2 + \frac{\epsilon^2}{2}\|\mathbf{D}\tilde{\mathbf{m}}\|_2^2, \tag{2.64}$$

where ϵ is a scalar trade-off parameter, and $\mathbf{D}$ denotes the differential-semblance-optimization (DSO) operator (Symes and Kern, 1994), whose continuous form for single extension h_x is given by:

$$D\tilde{m}_h(\mathbf{x}, h_x) = h_x \tilde{m}_h(\mathbf{x}, h_x). \tag{2.65}$$

The optimal image obtained by solving the convex problem of equation 2.64 presents improved coherency of poorly illuminated reflection angles from an irregular surface acquisition geometry within the angle-domain image space (Prucha and Biondi, 2002). In fact, as shown in Appendix B, the DSO operator is equivalent to a derivative operator when transformed to the subsurface-angle domain (Shen, 2005).

2.2.4 Full-waveform inversion

The ideal method to employ most of the information contained within recorded seismograms during an optimization problem was first proposed by Tarantola (1984), and it is commonly referred to as full-waveform inversion (FWI). The FWI problem is defined as follows:

$$\mathbf{m}_{FWI} = \underset{\mathbf{m}}{\operatorname{argmin}}\, \phi_{FWI}(\mathbf{m}) = \underset{\mathbf{m}}{\operatorname{argmin}} \frac{1}{2}\|\mathbf{K}_d\mathbf{f}(\mathbf{m}) - \mathbf{d}_{obs}\|_2^2, \tag{2.66}$$

where $\mathbf{f}$ represents the acoustic or elastic modeling operator (equations 2.27 and 2.24), $\mathbf{K}_d$ is a data sampling operator (e.g., equation 2.32), and $\mathbf{m}$ in this case represents the subsurface unknown property vector (e.g., equation 2.51). The optimization problem of equation 2.66 falls into the class of non-convex or non-linear optimization problems. Therefore, it does not have a closed-form solution as opposed to the linearized waveform inversion process. Furthermore, the cost of solving this optimization problem permits only the applications of gradient-based methods to find the optimal solution $\mathbf{m}_{FWI}$. In fact, the evaluation of the FWI objective function usually requires to find the solution of thousands of PDEs. Finally, the objective function ϕ_{FWI} presents multiple local minima and it is likely that the optimal solution is not unique (Virieux and Operto, 2009), which makes the final FWI solution sensitive to the initial model guess.

The gradient of the FWI objective function can be derived using the adjoint-state method (Chavent et al., 1975), and its derivation for the acoustic constant-density case is shown in Appendix A. The same result can be obtained by linearizing the considered wave equation and constructing the Jacobian of the operator $K_d\mathbf{f}$. By doing so, the gradient of ϕ_{FWI} can be written as:

$$\nabla\phi_{FWI}(\mathbf{m}) = \mathbf{B}(\mathbf{m})^*[\mathbf{K}_d\mathbf{f}(\mathbf{m}) - \mathbf{d}_{obs}], \tag{2.67}$$

where $\mathbf{B}$ denotes the Jacobian of the non-linear operator $\mathbf{K}_d\mathbf{f}$, which has the same form of the Born operators previously defined (i.e., equations 2.40 and 2.50).

As previously mentioned, the solution to the FWI problem is unlikely to be unique, given the ill-posed nature of the problem. Therefore, the application of regularization techniques is necessary to obtain useful FWI results. Here, I employ the ability of changing the basis functions representing the model vector $\mathbf{m}$. Specifically, I represent the model parameters using B-spline basis functions (De Boor, 1986; Bartels et al., 1995), and write the FWI problem as follows:

$$\mathbf{m}_{c,FWI} = \underset{\mathbf{m}_c}{\operatorname{argmin}} \frac{1}{2}\|\mathbf{K}_d\mathbf{f}(\mathbf{S}_c\mathbf{m}_c) - \mathbf{d}_{obs}\|_2^2, \tag{2.68}$$

where $\mathbf{m}_c \in \mathbb{R}^{N_m^c}$ represents the B-spline coefficients, and $\mathbf{S}_c$ is the operator that maps the spline coefficients into the FD model space necessary for the modeling step. This procedure reduces the number of inversion parameters. For example, in the acoustic case, $\mathbf{S}_c \in \mathbb{R}^{N_m \times N_m^c}$, with $N_m^c < N_m$. Additionally, Barnier et al. (2019) demonstrate the ability of this approach to improve the convergence properties of the FWI problem by effectively removing some of the local minima present in the original FWI problem of equation 2.66. To start the inversion process in this framework given an initial guess $\mathbf{m}_0$, defined on the FD-grid space (e.g., $\mathbb{R}^{N_m}$), I obtain the corresponding spline-grid initial model as follows:

$$\mathbf{m}_{c,0} = \mathbf{S}_c^{\dagger}\mathbf{m}_0, \tag{2.69}$$

where † represents the pseudo-inverse of an operator. Under certain spline-grid conditions, I can write $\mathbf{S}_c^{\dagger} = (\mathbf{S}_c^*\mathbf{S}_c)^{-1}\mathbf{S}_c^*$.

When an elastic FWI problem is considered, other parameterizations of the elastic model can be employed to solve the optimization problem. For instance, I can minimize the elastic FWI objective function with respect to the P- and S-wave velocities $\mathbf{v}_p$ and $\mathbf{v}_s$ and density $\boldsymbol{\rho}$. To do so without changing the non-linear modeling operator (equation 2.23), one can define the following non-linear composition of functions:

$$\mathbf{f}_{ela,v}(\mathbf{v}_p, \mathbf{v}_s, \boldsymbol{\rho}) = \mathbf{f}_{ela}[\mathbf{g}(\mathbf{v}_p, \mathbf{v}_s, \boldsymbol{\rho})], \tag{2.70}$$

where:

$$\begin{aligned}\mathbf{g}: \quad & \mathbb{R}^{3\times N_m} && \mapsto \mathbb{R}^{3\times N_m} \\ & \mathbf{g}(\mathbf{v}_p, \mathbf{v}_s, \boldsymbol{\rho}) && \mapsto \boldsymbol{\lambda}, \boldsymbol{\mu}, \boldsymbol{\rho}.\end{aligned} \tag{2.71}$$

The mapping function $\mathbf{g}$ is given by the following relations:

$$\begin{aligned}\lambda &= (v_p^2 - 2v_s^2)\rho, \\ \mu &= v_s^2\rho, \\ \rho' &= \rho.\end{aligned} \tag{2.72}$$

The Jacobian matrix of $\mathbf{f}_{ela,v}$ is given by the product of Jacobians of $\mathbf{f}_{ela}$ and $\mathbf{g}$. The former is shown in equation 2.46, while the latter is defined by the following equation:

$$\begin{bmatrix}\Delta\lambda \\ \Delta\mu \\ \Delta\rho'\end{bmatrix} = \begin{bmatrix}2v_p\rho & 2v_s\rho & (v_p^2 - 2v_s^2) \\ 0 & 2v_s\rho & v_s^2 \\ 0 & 0 & 1\end{bmatrix} \begin{bmatrix}\Delta v_p \\ \Delta v_s \\ \Delta\rho\end{bmatrix}. \tag{2.73}$$

2.3 Redatuming through extended linearized waveform inversion and target-oriented inversion

The goal of any redatuming method is to transform the observed data acquired at a certain location (e.g., at the surface) into a new dataset as if they had been acquired at a different location in the subsurface (Wapenaar et al., 1992; Mulder, 2005). Here, I seek to reconstruct the data generated from a target area that is recorded with sources and receivers placed directly above the target. This process enables the application of an FWI algorithm only within the target area. If the elastic parameters compose the model vector, then I refer to the redatuming and inversion steps as “target-oriented elastic FWI”.

The data reconstruction or redatuming step is performed by first solving an extended linearized waveform inversion using a subset of the surface data $\mathbf{d}$ (e.g., the data where the direct arrival has been removed), which corresponds to the minimization of the following objective function:

$$\phi(\tilde{\mathbf{p}}) = \frac{1}{2}\|\tilde{\mathbf{B}}_{aco}(\mathbf{v})\tilde{\mathbf{p}} - \mathbf{d}\|_2^2 + \frac{\epsilon^2}{2}\|\mathbf{D}\tilde{\mathbf{p}}\|_2^2, \tag{2.74}$$

where $\mathbf{v}$ represents the acoustic migration velocity, and the regularization term is added to diminish the previously mentioned illumination artifacts. The extended image $\tilde{\mathbf{p}}$ (or extended scattering potential) preserves the amplitude variations of the surface data. In the next chapter, I illustrate this property by using different synthetic tests where elastic pressure data is migrated using acoustic imaging operators.

The optimal solution to the previous imaging problem $\tilde{\mathbf{p}}_{mig}$ is then used to reconstruct the data $\mathbf{d}'$ corresponding to sources and receivers placed at a new subsurface acquisition level. The reconstruction is performed by the following demigration process:

$$\mathbf{d}' = \tilde{\mathbf{B}}'_{aco}(\mathbf{Mv})\tilde{\mathbf{M}}\tilde{\mathbf{p}}_{mig}, \tag{2.75}$$

where $\mathbf{M}$ and $\tilde{\mathbf{M}}$ are restriction operators that limit the model and extended image to only the target area, respectively. The symbol $'$ denotes quantities related to the new acquisition geometry. The success of this reconstruction method depends on the knowledge of an accurate overburden, which is a common assumption within any redatuming technique. The advantage of this redatuming process compared to other methods resides in the usage of the image space to reconstruct the subsurface data. In fact, the usage of the regularization term during this step releases the common strict constraint of having dense source-receiver surface sampling.

Given the redatumed data $\mathbf{d}'$, I design a target-oriented FWI problem as follows:

$$\Phi(\mathbf{m}) = \frac{1}{2}\left\|\mathbf{K}\mathbf{f}'(\mathbf{m}) - \mathbf{d}'\right\|_2^2, \tag{2.76}$$

where $\mathbf{m}$ represents the unknown subsurface parameters of the target area, and $\mathbf{f}'$ is the wave equation non-linear operator. When elastic pressure data are used during the redatuming and inversion steps, then an overall decrease in computational cost is obtained compared to the application of an elastic FWI method directly to the surface data.

To intuitively understand how the redatuming step works, let d_{z_0} represent the subset of the observed data of interest (e.g., reflected events). Furthermore, I assume that d_{z_0} is given by the following relation:

$$d_{z_0}(\mathbf{x}_r, \mathbf{x}_s, t) = \int_{\Omega_p} g(\mathbf{x}_r, \mathbf{x}, t) * g(\mathbf{x}, \mathbf{x}_s, t) p(\mathbf{x}) \mathbf{dx}, \tag{2.77}$$

where $*$ denotes the time convolution, p represents a scattering potential (also referred to subsurface image), and g is the Green's function for the acoustic wave equation. Equation 2.77 represents the solution to the linearized acoustic wave equation (equations 2.35 and 2.36). Furthermore, it is trivial to modify equation 2.77 to employ an extended scattering potential (equation 2.59).

Figure 2.2a schematically illustrates the process of computing the data $\mathbf{D}_{z0,target}$ for a single point in the scattering potential and one source and receiver pair. The source wavefield $G(\vec{x}_p, \vec{x}_s)$ propagates from the source position $\vec{x}_s$ at the surface z_0 and it is then scattered by an image point placed at $\vec{x}_p$. This secondary source is then propagated by the receiver-side Green's function

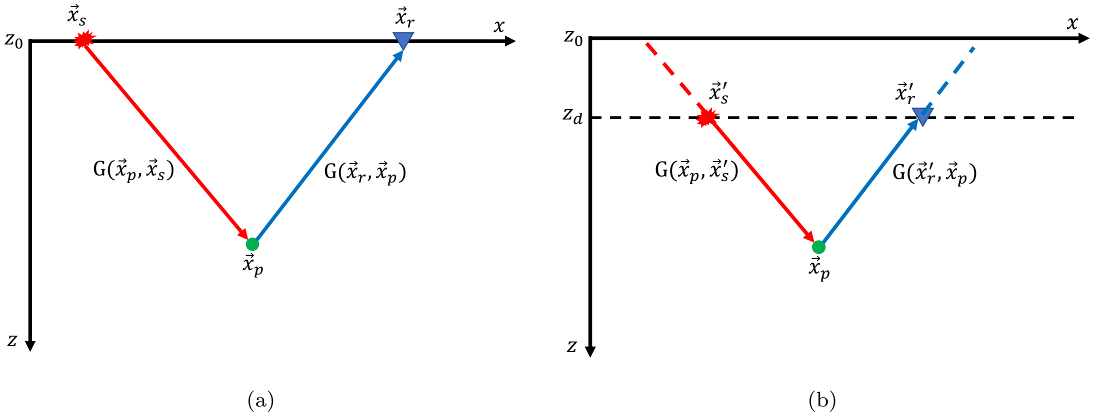

Figure 2.2: (a) Schematic plot of equation 2.77. The data observed at $\vec{x}_r$ are generated by the field propagating from $\vec{x}_s$ impinging on the scattering point at $\vec{x}_p$. (b) The same process can be used to generate the same data but with the source and receiver placed at z_d. [**NR**]

$G(\vec{x}_r, \vec{x}_p)$ and recorded from the device placed at $\vec{x}_r$. To obtain the same data but for the source-receiver pair placed at z_d, deeper than the surface level z_0, the same scattering potential can be used to generate the data for a source-receiver pair placed at $\vec{x}'_s$ and $\vec{x}'_r$ (Figure 2.2b). Hence, the knowledge of the scattering potential p enables the computation of the same event for a given source-receiver pair placed at two different depth levels.

Since this redatuming procedure is based on the formation of an image, the source-receiver distribution at the new datum depends on the maximum extent of the surface acquisition. Figure 2.3 shows how the surface acquisition geometry extent changes when mapped to a deeper subsurface position z_d assuming a constant velocity. The surface and datum acquisition extents $\bar{x}$ and $\bar{x}'$ identically illuminates the image point $\vec{x}_p$. Therefore, an image formed using the data acquired at z_0 with a source-receiver extent $\bar{x}$ can be employed to synthesize the data with an acquisition extent $\bar{x}'$ at z_d. The datumed acquisition geometry is reduced compared to the surface one. Thus, when generating the datumed dataset, a reduced source-receiver distribution must be used to avoid the introduction of data artifacts due to the limited illumination of the surface acquisition.

2.4 Summary

In this chapter, I defined the main terms composing the elastic and acoustic isotropic wave-equations and how they are connected to one another. I discretized them to obtain linear systems of equations that can be inverted so that elastic and acoustic wavefields can be computed within a computer. Then, I linearized them with respect to the subsurface-model parameters and illustrate how their Born approximation is employed within non-linear and linear waveform inversion frameworks. Moreover, I explained how the acoustic linearized wave equation is extended to include additional degree

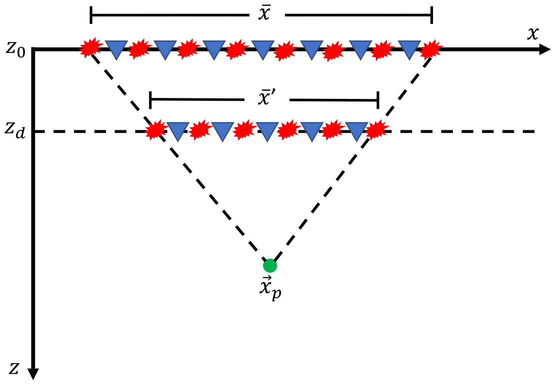

Figure 2.3: Schematic illustrating how the surface acquisition extent $\bar{x}$ at z_0 becomes $\bar{x}'$ when moved to z_d assuming a constant velocity and identical illumination for the point $\vec{x}_p$. [**NR**]

of freedom, compared to the physical axes, within the scattering potential. Finally, I described how an extended linearized waveform inversion process is used to perform a redatuming step in which the surface data are effectively move from the surface acquisition depth to a deeper level close to any area of interest. The redatumed data are then used within an elastic FWI process to retrieve the unknown subsurface parameters.

Chapter 3

Synthetic application of target-oriented elastic FWI

The purpose of this chapter is to illustrate, using various synthetic examples, how the previously described wave-equations operators are employed to retrieve the elastic parameters of the subsurface.

In the first section, I demonstrate using numerical 2D synthetic tests the ability of the extended image space to preserve the elastic amplitude variations present in the reflected events recorded at the surface. I start by showing how the amplitude variations with offsets of a reflected event from a single interface are perfectly mapped into the extended angle-domain image. Then, I solve an extended linearized waveform inversion problem to map elastic pressure data scattered by sediment lenses placed underneath a salt body. This second test shows the extended space's ability to preserve elastic amplitude even with a linearized waveform regime within a complex geological scenario.

In the second section, I describe how the extended migrated volume is used to synthesize a seismic survey as if it had been acquired in the proximity of a target area. To this end, I use the single-interface model and show how the redatuming process works. I demonstrate the independence of the image-based redatuming with respect to the source signal used during the imaging inversion. Then, I illustrate its sensitivity to the velocity of the overburden and the importance of employing a correct migration velocity during the migration process.

In the section of this chapter, I solve an elastic FWI problem using the surface data obtained on a complex subsurface model. This example shows an FWI workflow's ability to estimate the high-wavenumber components of the elastic parameters from seismic data. Then, I apply the redatuming process to synthesize the waveforms generated by a gas-sand target and use a target-oriented elastic FWI workflow to correctly estimate the gas reservoir properties. The target-oriented inversion is approximately 400 times less computationally intensive compared to the surface-data elastic FWI process.

3.1 Amplitude-preserving migration

In seismic exploration, the output of any amplitude-preserving or true-amplitude migration is an image volume whose values are proportional, up to a constant factor, to the P-wave plane-wave reflection coefficients of the subsurface interfaces (Gray and Bleistein, 2009). For instance, in the 2D case, when we fix the spatial coordinates corresponding to a planar geological interface, the image amplitudes as function of the reflection angle must be proportional to the reflection coefficient Rpp predicted by the Zoeppritz equations (Aki and Richards, 2002). These kinds of image volumes are then employed to predict the elastic-parameter contrasts present in the subsurface as well as their petrophysical properties (Buland and Omre, 2003; Grana and Della Rossa, 2010). Using three synthetic 2D numerical tests, I show how the solution to an extended linearized waveform inversion problem corresponds to a true-amplitude image based on the above definition.

3.1.1 Single-interface synthetic example

In this first numerical example, I use two single-interface elastic models to generate elastic pressure data. The elastic-parameter contrast is flat in one case and tilted by 10° in the other.

Flat interface

Figure 3.1 shows the P-wave velocity model for the flat interface test. The change in the elastic parameters is depicted in the three vertical profiles shown in Figure 3.2, where an increase of all the elastic parameters is occurring across the interface. I generate elastic pressure data using an explosive source (i.e., $\mathbf{m}_{ij} \neq 0$ for $i = j$), whose time signature and spectrum is displayed in Figure 3.3.

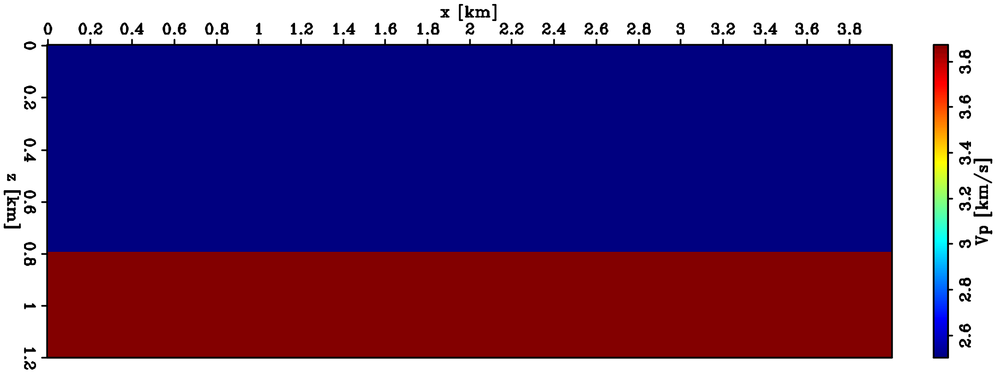

Figure 3.1: P-wave velocity model of the elastic single-interface model used in the first amplitude-preserving numerical test. [**ER**]

I record the pressure using 81 sources and 401 receivers placed at the surface and spaced by 50 and 10 m, respectively. A single reflected event is recorded by the receivers for each experiment,

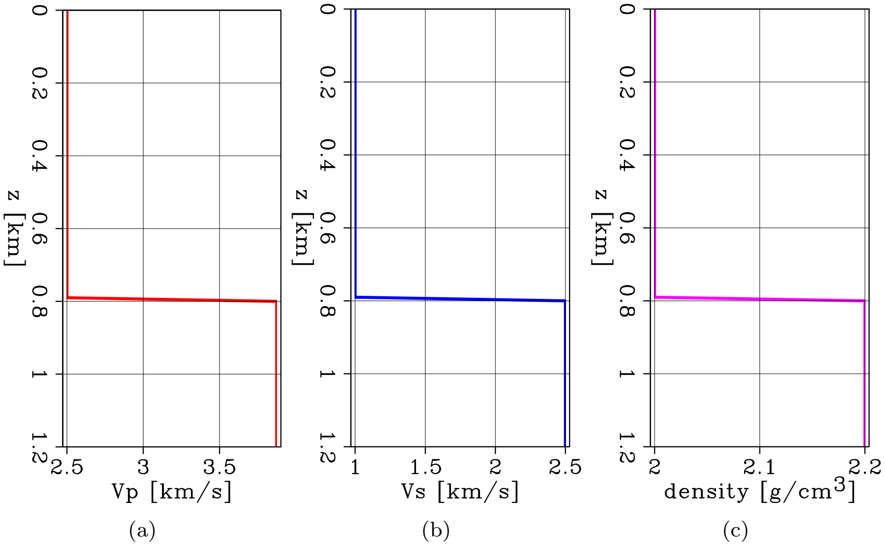

(a) (b) (c)

Figure 3.2: Elastic parameter profiles of the single-interface model. The three panels show the (a) P-wave, (b) S-wave, and (c) density profiles, respectively. [**ER**]

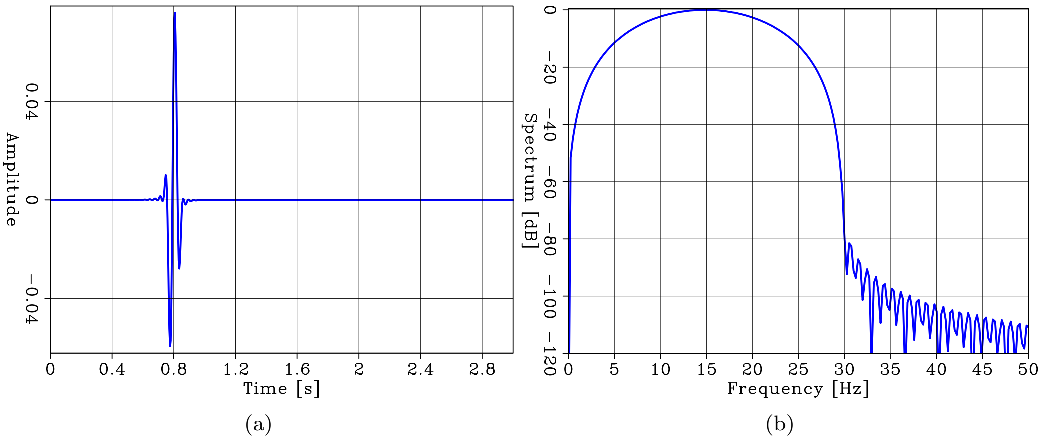

(a) (b)

Figure 3.3: Explosive source used to generate the elastic pressure data for the true-amplitude migration tests. Panel (a) and (b) show the time signature and frequency spectrum, respectively. [**ER**]

where a clear phase rotation is present as the offset between source and receiver pair increases (Figure 3.4)

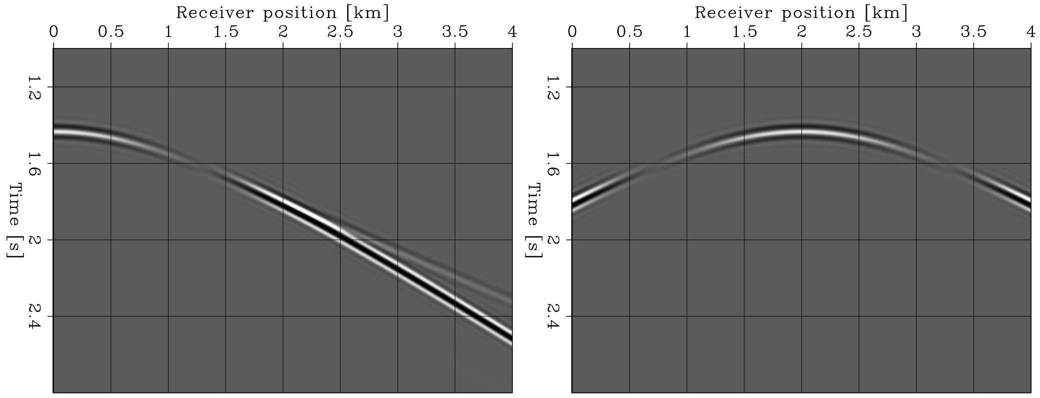

(a) (b)

Figure 3.4: Elastic pressure waves recorded at the surface for a shot placed at (a) $x = 0$ km and (b) $x = 2.0$ km, respectively. The direct arrival has been removed from the observed data. [**ER**]

To perform the migration step, I solve two linearized waveform inversion problems using acoustic Born modeling operators. To show the importance of using an extended imaging condition (equation 2.57), I employ non-extended and extended Born operators and minimize the objective functions using 500 iterations of the linear conjugate gradient (CG) method (Aster et al., 2018). In both cases, the migration velocity model is a constant speed set to 2.5 km/s. Figure 3.5a shows the comparison between the convergence rates when the two operators are employed to generate the subsurface image using the same elastic pressure data shown in Figure 3.4. It is clear that when the extended space is used during the image formation, the relative objective function decrease reaches almost a numerical level of accuracy for single-precision operators (i.e., 10^{-6}). On the other hand, the non-extended migration can only achieve approximately a 10% value compared to the initial objective function. This observation is also highlighted by comparing the data residuals for the two migration processes for a given shot gather (Figures 3.5b and Figures 3.5c). The extended image space can fully preserve all the elastic amplitudes present in the recorded data. On the contrary, the non-extended operator lacks this property, resulting in the non-extended Born operator's inability to model all the elastic pressure variations of the data. This simple comparison demonstrates that elastic amplitude variations cannot be fully projected into the non-extended image space.

The extended linearized waveform inversion problem's solution is a function of the spatial coordinates x and z and of the extended subsurface offset axis h. The shape of the image highly depends on the recorded events and the acquisition geometry employed. Figure 3.6 shows the offset-domain common image gathers (ODCIGs) for two different x coordinates. For $x = 2.0$ km, the ODCIG

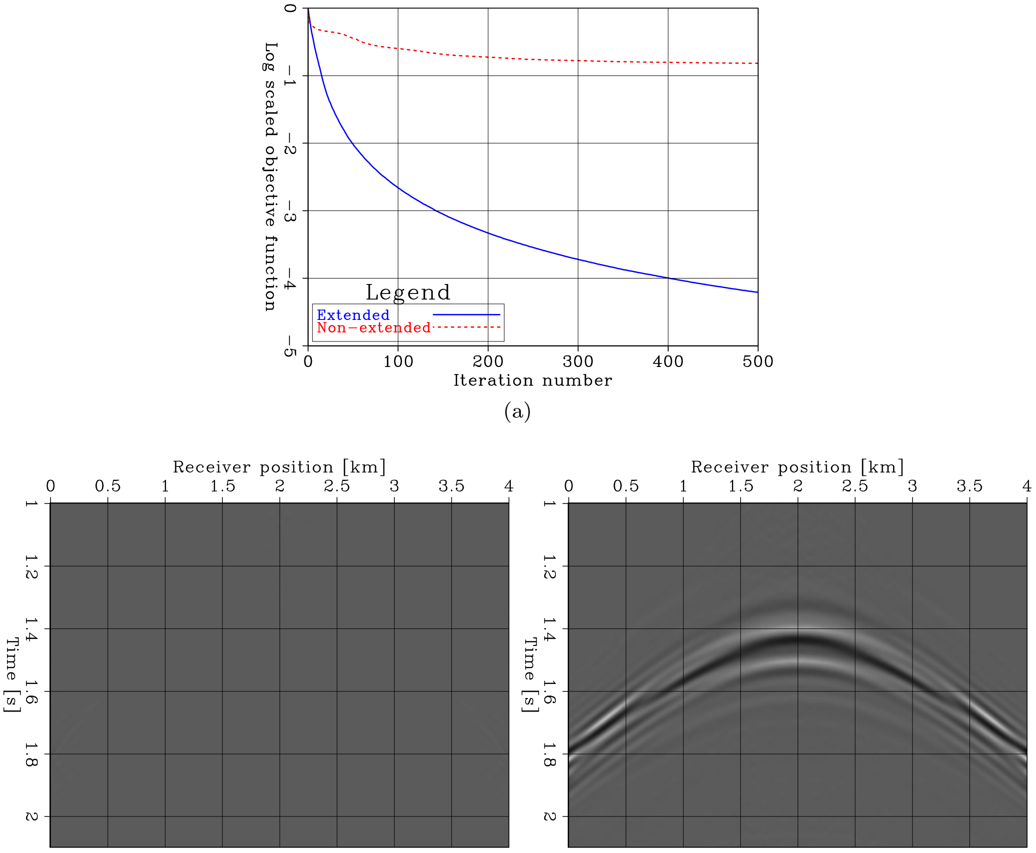

(a)

(b) (c)

Figure 3.5: (a) Comparison of the convergence rate for the extended (blue curve) and non-extended linearized (red dashed curve) waveform inversion problems for the data from the flat interface shown in Figure 3.4. Final data residual vectors for the shot placed at $x = 2.0$ km for the (b) extended and (c) non-extended migration processes. These last two panels have the same dynamic range. [**CR**]

appears to be focused around the zero-offset axis. This behavior is expected since the correct migration velocity has been used during the inversion process (Biondi and Tisserant, 2004). The two linear features below $z = 0.8$ km represent the head waves recorded in the longer offset shot gathers mapped into the image space. The other two faint linear feature above $z = 0.8$ km are caused by the limited acquisition aperture (i.e., the maximum source-receiver offset of 4 km). On the other hand, when an ODCIG is extracted at $x = 0.0$ km (Figure 3.6a), the image does not appear as focused as for the central-model position because fewer reflection angles have been illuminated from the surface acquisition.

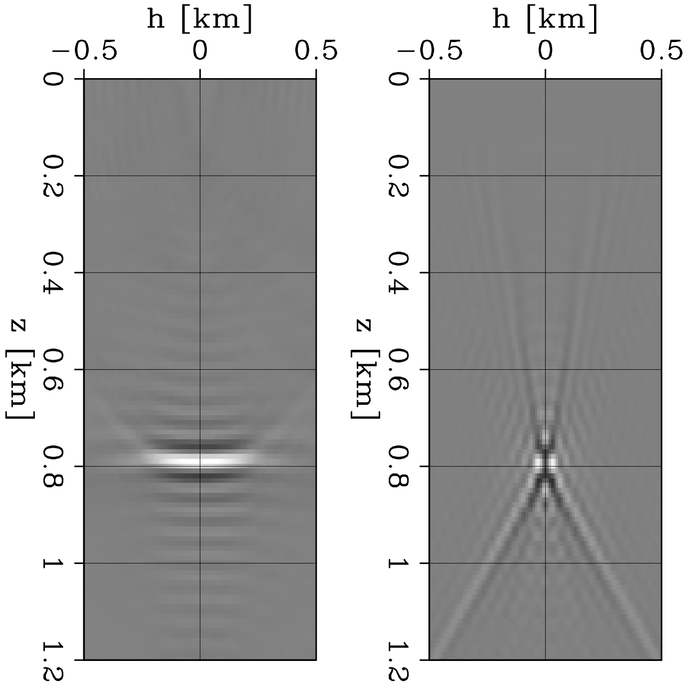

(a) (b)

Figure 3.6: Subsurface-offset common image gathers for the flat-interface example extracted at (a) $x = 0$ km and (b) $x = 2.0$ km, respectively. [**CR**]

To highlight the importance of using the pseudo inverse of the offset to angle transform to obtain angle-domain common image gathers (ADCIGs), I employ a synthetic example in which a single event with constant angle response is present in the subsurface (Figure 3.7a). This ADCIG is transformed into the corresponding ODCIG using the transformation derived in Appendix B (Figure 3.7b). When this ODCIG is mapped back to the angle domain, different results are obtained whether the adjoint or pseudo-inverse operators are employed. Figure 3.7c shows the result of applying the adjoint operator. The shape and amplitude response is different compared to the original angle response of Figure 3.7c; especially, for large reflection angle γ. On the contrary, the pseudo inverse application

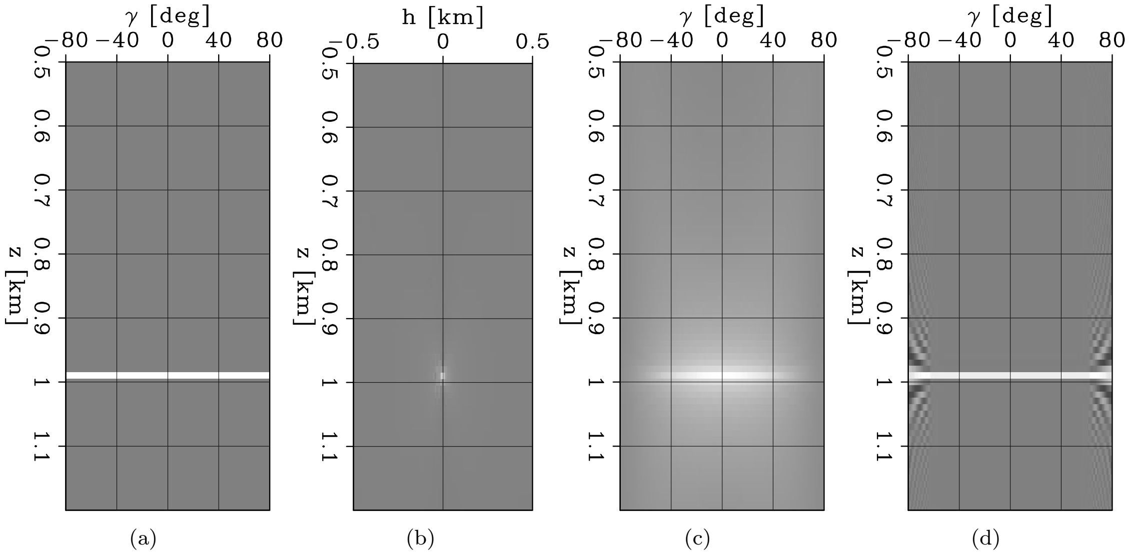

(a) (b) (c) (d)

Figure 3.7: Single-reflector example with constant angle response highlighting the importance of using the pseudo-inverse operator of the subsurface-offset to angle transformation. (a) Original ADCIG. (b) ODCIG obtained from the original AD gather. ADCIGs obtained by applying the (c) adjoint and (d) pseudo-inverse operators of the OD to AD transform, respectively. [**ER**]

can better retrieve the original ADCIG response (Figure 3.7d). The artifacts present above 60° reflection angle are due to the numerical approximation of the oscillatory integral of equation B.5. In fact, this equation can be written as follows:

$$\int_{-\infty}^{\infty} \hat{I}_h(k_z,h)e^{i2\pi k_z \tan(\gamma)h}dh = \int_{-\infty}^{\infty} \hat{I}_h(k_z,h)[\cos(2\pi k_z \tan(\gamma)h) - i\sin(2\pi k_z \tan(\gamma)h)]dh, \quad (3.1)$$

where it is clear that numerical errors would occur for $|k_z \tan(\gamma)| > k_{h,max}$, in which $k_{h,max}$ denotes the Nyquist sampling rate of the subsurface-offset axis. In this case, to diminish such numerical errors, the previous integral has been computed for $|k_z \tan(\gamma)| \leq k_{h,max}$ only.

Figure 3.8 compares the correct angle response against the amplitudes of the ADCIGs in Figures 3.7c and 3.7d extracted at $z = 1.0$ km. As expected, the adjoint provides an angle response that follows a cosine behavior (equation B.12). Conversely, the pseudo inverse is able to retrieve the original amplitude response up to 60° angle, above which the discretization of the integral does not allow a correct reconstruction. This test demonstrates the importance of using the pseudo-inverse operator of the offset to angle transform for obtaining amplitude-preserving angle gathers. In fact, all the ADCIGs shown below are computed by applying the pseudo inverse of this transformation.

The previous observations drawn from Figure 3.6 are more evident when the ODCIGs are transformed into the corresponding ADCIGs. The reflection angles that are illuminated for a given x are

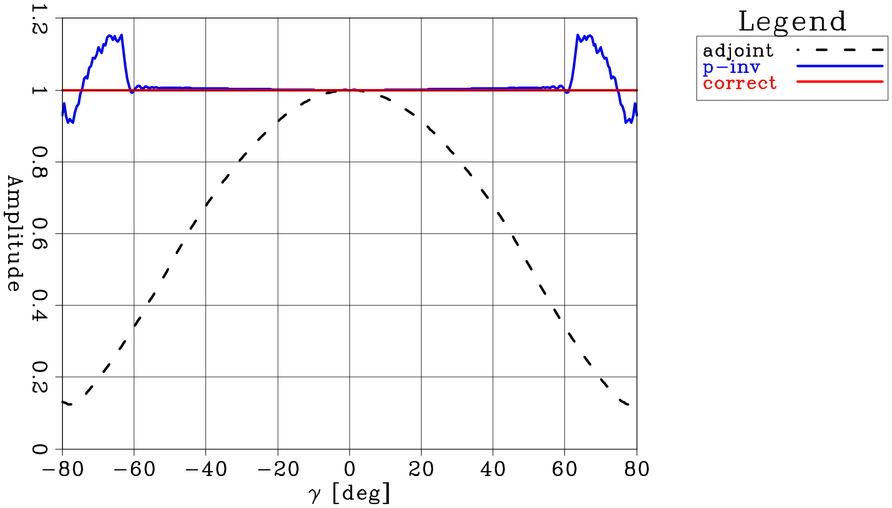

Figure 3.8: Amplitude response extracted at $z = 1.0$ km from the angle-domain gathers of Figure 3.7. The red line represents the correct constant angle response, while the black dashed and blue continuous denote the responses after applying the adjoint and the pseudo-inverse operators, respectively. All responses have been scaled to have the same value for $\gamma = 0$. [**ER**]

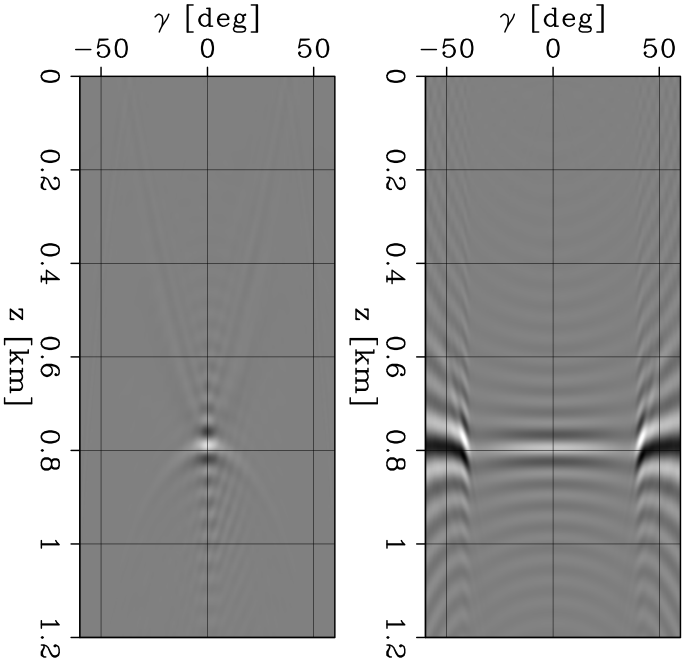

(a) (b)

Figure 3.9: Angle-domain common image gathers for the flat-interface example extracted at (a) $x = 0$ km and (b) $x = 2.0$ km. respectively. [**CR**]

now obvious in the panels of Figure 3.9. As expected, for $x = 0.0$ km, the ADCIG presents energy focused close to the zero reflection angle axis. On the other hand, when the ADCIG is extracted at $x = 2.0$ km, a flat event positioned at the interface depth is present.

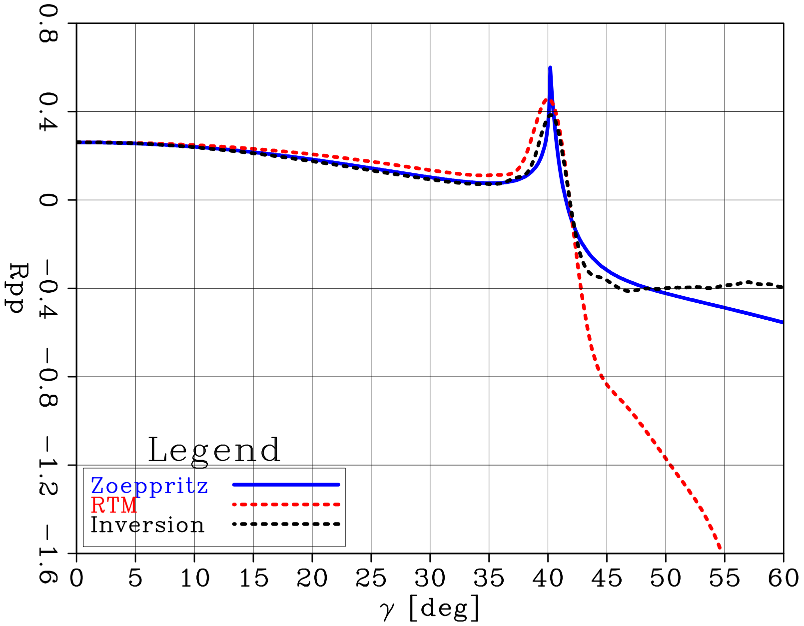

Figure 3.10: Comparison between the angle response extracted at $z = 0.8$ km from the ADCIG generated by 1 iteration (red dashed curve) and 500 iterations (black dashed curve) of extended linearized waveform inversion on the flat-interface model and the theoretical response predicted using Zoeppritz equation (blue curve). The ADCIG amplitudes have been scaled so that the three responses match for $\gamma = 0$. [**CR**]

To verify that the amplitude response of the ADCIG in Figure 3.9b is representing a true-amplitude imaged volume, I extract image amplitude at $z = 0.8$ km and compare it against the plane-wave reflection coefficient Rpp of the planar interface (Figure 3.10). A close fit between the ADCIG response and the theoretical Rpp is obtained for angles up to 42° (compare the blue and black dashed curves), which is beyond the critical angle of 40°. The mismatch at higher angular values is due to the limited acquisition aperture as well as the truncation of the iterative inversion process. To highlight the importance of the iterative process, I plot the ADCIG response obtained with a single iteration of the linearized waveform inversion (i.e., by applying an extended reverse time migration (RTM) process). A close fit is obtained for pre-critical angles. However, for angle beyond 40°, the response suffers from the missing compensation of the propagation effects, which are mitigated by the inversion process.

Tilted

As described by Sava and Fomel (2003), the transformation from subsurface offsets to angles is independent of the geological dip of the subsurface reflectors when the correct migration velocity is considered during the image formation. To show this property, I perform the same synthetic test as in the previous example but where the interface is dipping by 10° (Figure 3.11).

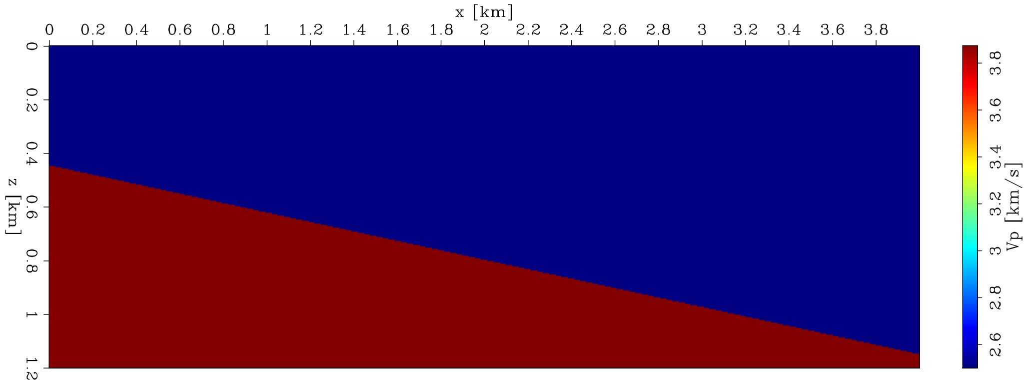

Figure 3.11: P-wave velocity model of the elastic single-interface model tilted by 10°. [**ER**]

By applying the same iterative process to solve the linearized waveform inversion problem based on the slanted-interface data, I obtain the ODCIGs shown in Figures 3.12a and 3.12b. In this case, the focusing depth in the gathers coincides with the interface's position for the considered horizontal coordinate. As in the previous case, the ODCIG at $x = 0.0$ km is not as focused around $h = 0.0$ km as the one extracted at the center of the model due to the angular coverage of the reflected event. The same observations on the ADCIGs as in the flat-interface case are valid when the reflector is tilted (Figures 3.12c and 3.12d). Additionally, even if the interface is dipping, a similar amplitude variation with angles can be observed in the ADCIG of Figure 3.12d when compared to the one of Figure 3.9b. When the amplitude response from the central ADCIG is compared to the theoretical Rpp, a similarly close match is observed (Figure 3.13). The slight dissimilarities compared to Figure 3.10 are due to the different illuminated reflection angles from the surface acquisition as well as the Cartesian coordinate-system approximation of the tilted interface. This synthetic test demonstrates the invariability of the ODCIG to ADCIG transform with respect to the geological dip in the 2D case.

3.1.2 Subsalt synthetic example

When imaging targets are present underneath a salt body, the correct recovery of a true-amplitude migrated volume becomes challenging for multiple reasons (Muerdter and Ratcliff, 2001a; Prucha and Biondi, 2002):

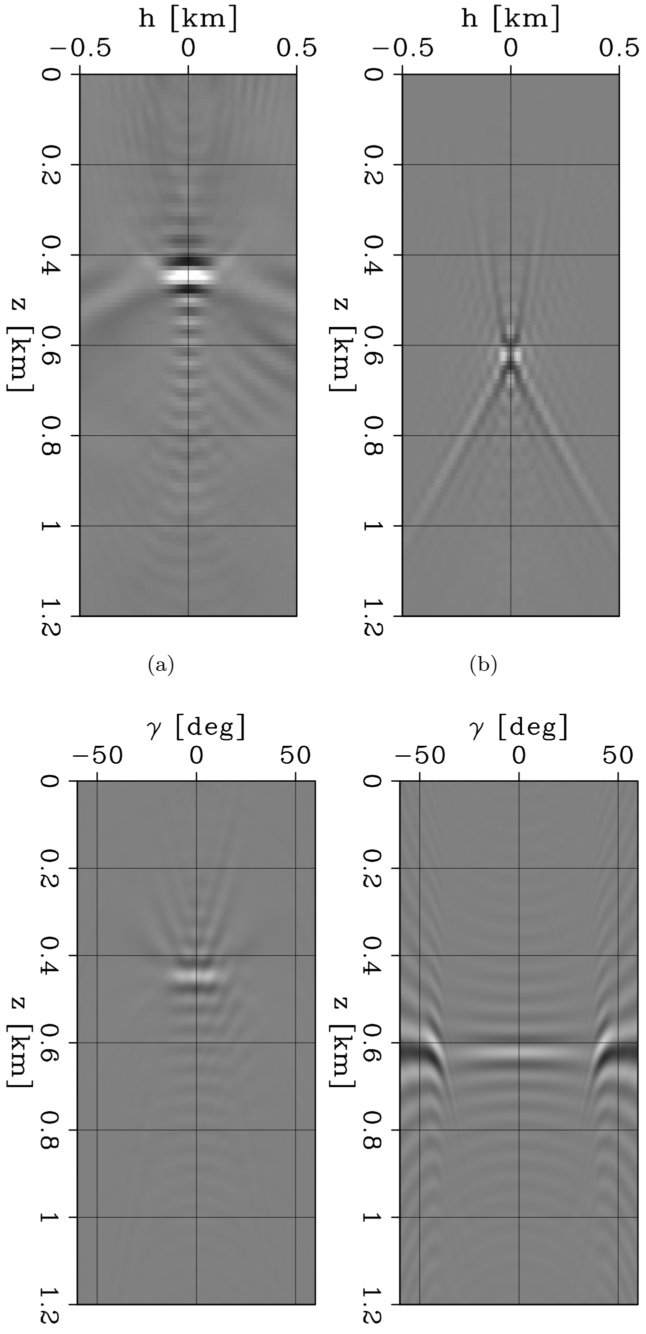

(a) (b)

(c) (d)

Figure 3.12: Subsurface-offset common image gathers for the tilted interface example extracted at (a) $x = 0$ km and (b) $x = 1.0$ km, respectively. The panels (c) and (d) display the previous image gathers in mapped into the angle domain. [**CR**]

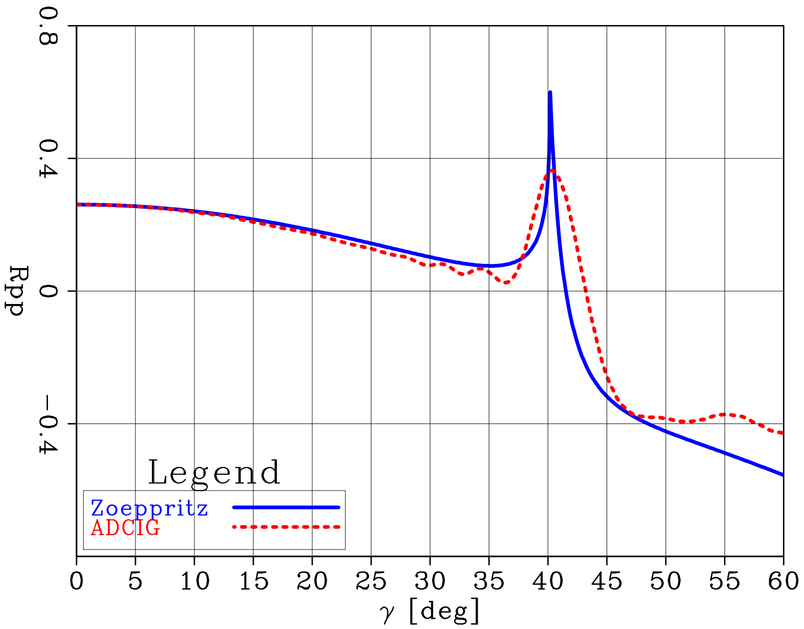

Figure 3.13: Comparison between the angle response extracted at $z = 0.64$ km from the ADCIG (red dashed curve) of Figure 3.12d and the theoretical response predicted using Zoeppritz (blue curve). The ADCIG amplitudes have been scaled so that the two responses match for $\gamma = 0$. [**CR**]

- Any imaging method would be affected by the shadow zones below the salt body, where little energy is reflected.
- Amplitude variations caused by salt structures focusing seismic energy would hamper the constructed subsalt image.
- The subsalt image is significantly impacted by the choice of the acquisition geometry, making the survey design a crucial step in subsalt seismic exploration scenarios (Muerdter and Ratcliff, 2001b).

In this example, I show how a regularized linearized waveform inversion can correctly retrieve the subsalt amplitude variation with angles (AVA) of sand lenses placed underneath a large salt body. Figure 3.14 displays the true P-wave velocity model where a salt body presenting a rugose top interface is placed above three sediment lenses. To understand the variability of other elastic parameters, I plot a vertical profile for $x = 10.0$ km (Figure 3.15). A substantial increase in both P- and S-wave velocities is encountered within the salt body, while a mild decrease in the density is present compared to the surrounding sediments. The sand lenses present a moderate increased S-wave velocity, whereas small variations appear in the other two elastic parameters. The elastic-parameter changes of the lenses correspond to a gas-bearing sand (Castagna and Swan, 1997).

To generate the observed elastic pressure data and simulate a realistic long-offset acquisition

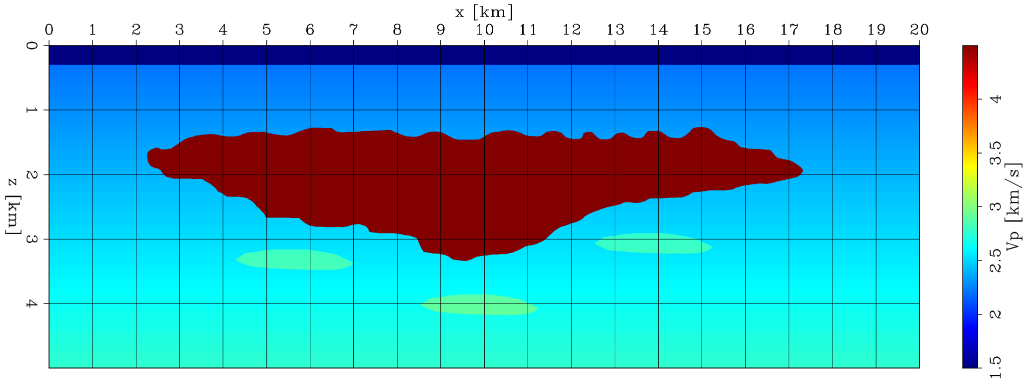

Figure 3.14: P-wave velocity model of the elastic model used in the subsalt amplitude-preserving numerical test for the three sand lenses. [**ER**]

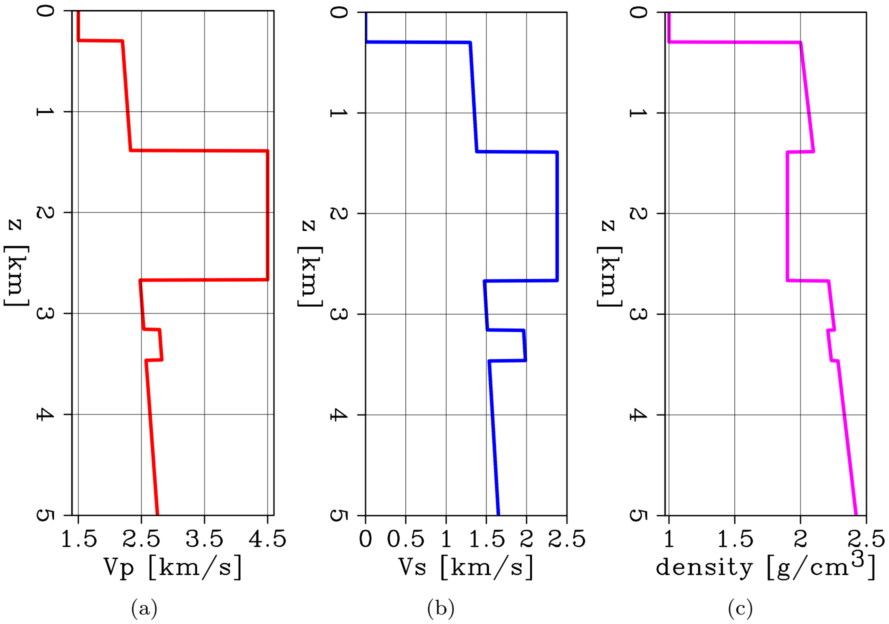

(a) (b) (c)

Figure 3.15: Elastic parameter profiles of the salt model extract at $x = 5.0$ km. The three panels show the (a) P-wave, (b) S-wave, and (c) density profiles, respectively. [**ER**]

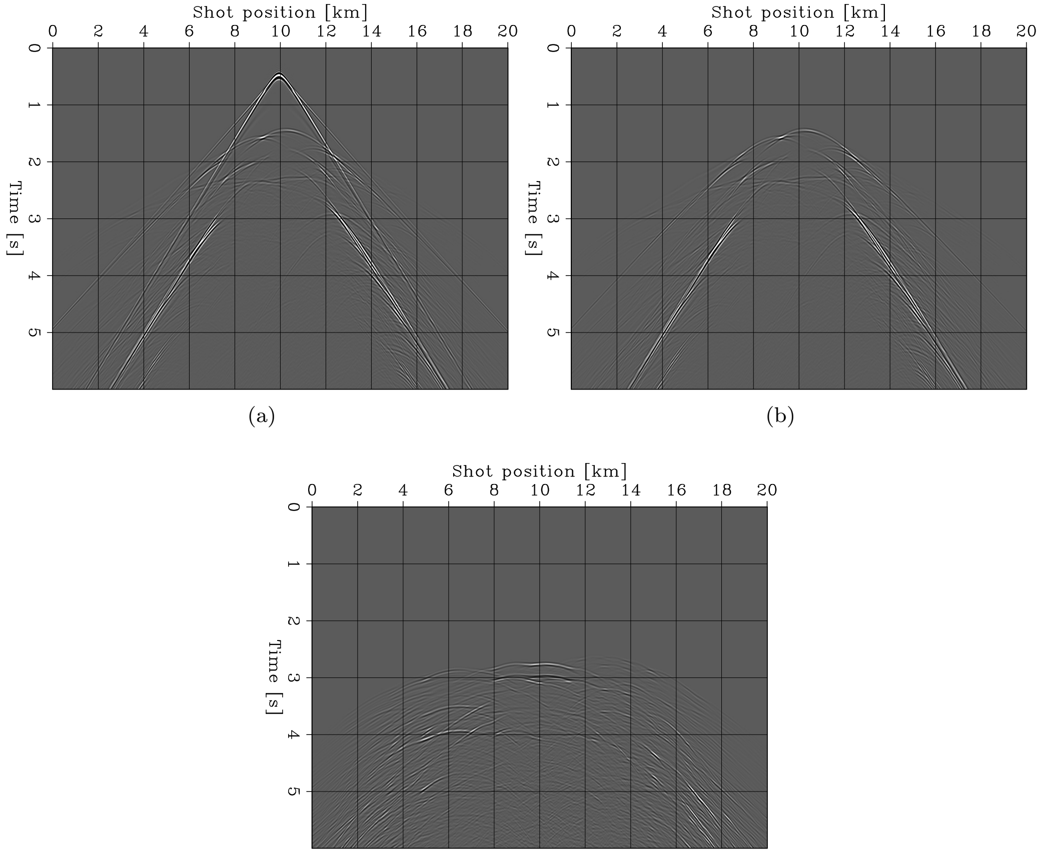

(a) (b)

(c)

Figure 3.16: Elastic pressure waves recorded by a receiver placed at $x = 9.94$ km at the sea floor. (a) Observed pressure. (b) Observed pressure where the direct arrival has been remove. (c) Observed pressure related to the presence of the subsalt lenses. Panels (a) and (b) have the same clipping, while panel (c) has a narrower dynamic range. [**ER**]

geometry, I place 250 ocean-bottom nodes at the water-sediment contact (i.e., $z = 0.3$ km), starting from $x = 2.5$ km and evenly spaced by 60 m. The 1001 sources are placed at the surface and evenly separated by 20 m from each other. A representative receiver gather at $x = 10.0$ km is shown in Figure 3.16a. Multiple scattered events are present underneath the direct arrival due to the presence of the salt body and the sand lenses. To show the effect of the data used during the linearized waveform inversion on the final migrated image, I perform two tests using the observed elastic pressure. In one case, I migrate the data in which the direct arrival has been removed by computing the elastic pressure due to only the water layer and sediments (i.e., without the salt body and the sand lenses) (Figure 3.16b). In the other one, only the events related to the sand lenses' presence are employed during the imaging process (Figure 3.16c). To obtain the second test events, I subtract the elastic pressure modeled using an elastic subsurface that does not contain the sand lenses from the observed data. In both tests, all the non-linear effects are still present (e.g., amplitude variations, converted events, and multiples).

These two datasets are employed within an acoustic extended linearized waveform inversion problems (equation 2.62) and are solved using 500 iterations of linear CG method. As migration velocity, I use the true P-wave model from which I remove the sand lenses. The convergence rates of the two processes are displayed in Figure 3.17a. Contrary to the single-interface example, the optimization does not reach a perfect match. However, they both reach an approximately flat convergence rate for the number of iteration chosen. To understand which events could not be mapped into the extended image space, I plot the final data residual for the receiver gather extracted at $x = 10.0$ km for both datasets (Figures 3.17b and 3.17c). In both panels, most of the events have been mapped into the image space. However, some energy possibly corresponding to converted waves cannot be modeled using the maximum subsurface offset of 0.5 km. In fact, by analyzing three ODCIGs passing through the three lenses (Figures 3.18a, 3.18b, and 3.18c), it is clear that a larger subsurface offset extent is necessary to match the data. The goal of this test is not to match all the recorded events but only the ones corresponding to PP reflections. These events focus on the proximity of the zero-subsurface offset axis since the correct migration velocity has been used during the migration process. As a matter of fact, when these image gathers are transformed into the corresponding ADCIGs (Figures 3.18d, 3.18e, and 3.18f), flat events at depths corresponding to the geological interfaces of the elastic model are present. The continuity of the amplitude across the reflection angle is hampered by the relatively sparse receiver acquisition geometry, as well as the presence of converted waves recorded in the elastic pressure data.

Similar conclusions can be drawn from the image gathers obtained by migrating only the events due to the sand lenses (Figure 3.19). However, in this case, clearly noticeable flat events corresponding to the lens interfaces can be observed in the ADCIGs, which highlights the importance of performing a data selection pre-processing step before migration when dealing with field applications.

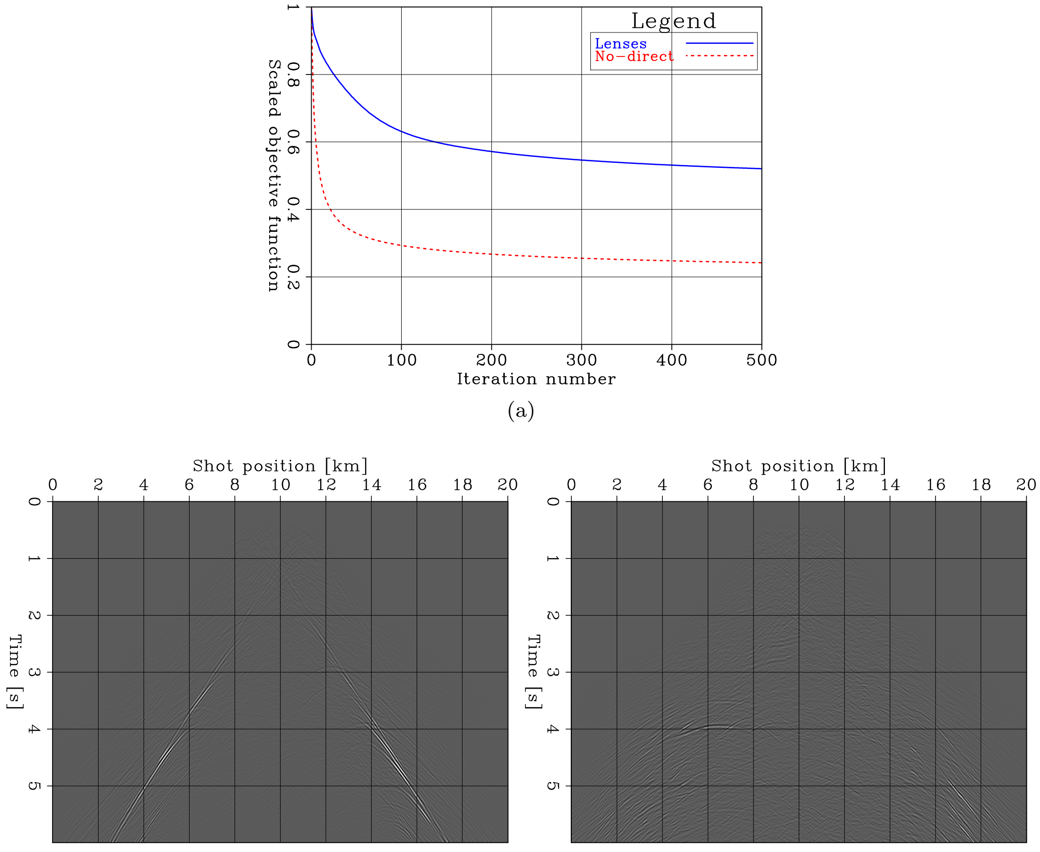

(a)

(b)

(c)

Figure 3.17: (a) Comparison of the convergence rate for the extended linearized waveform inversion when the data shown in Figures 3.16b (blue curve) and 3.16c (red dashed curve) are employed during the migration process. Each curve is scaled separately. The panels (b) and (c) depict the final residual vectors when the data shown in Figures 3.16b and 3.16c are iteratively imaged, respectively. [**CR**]

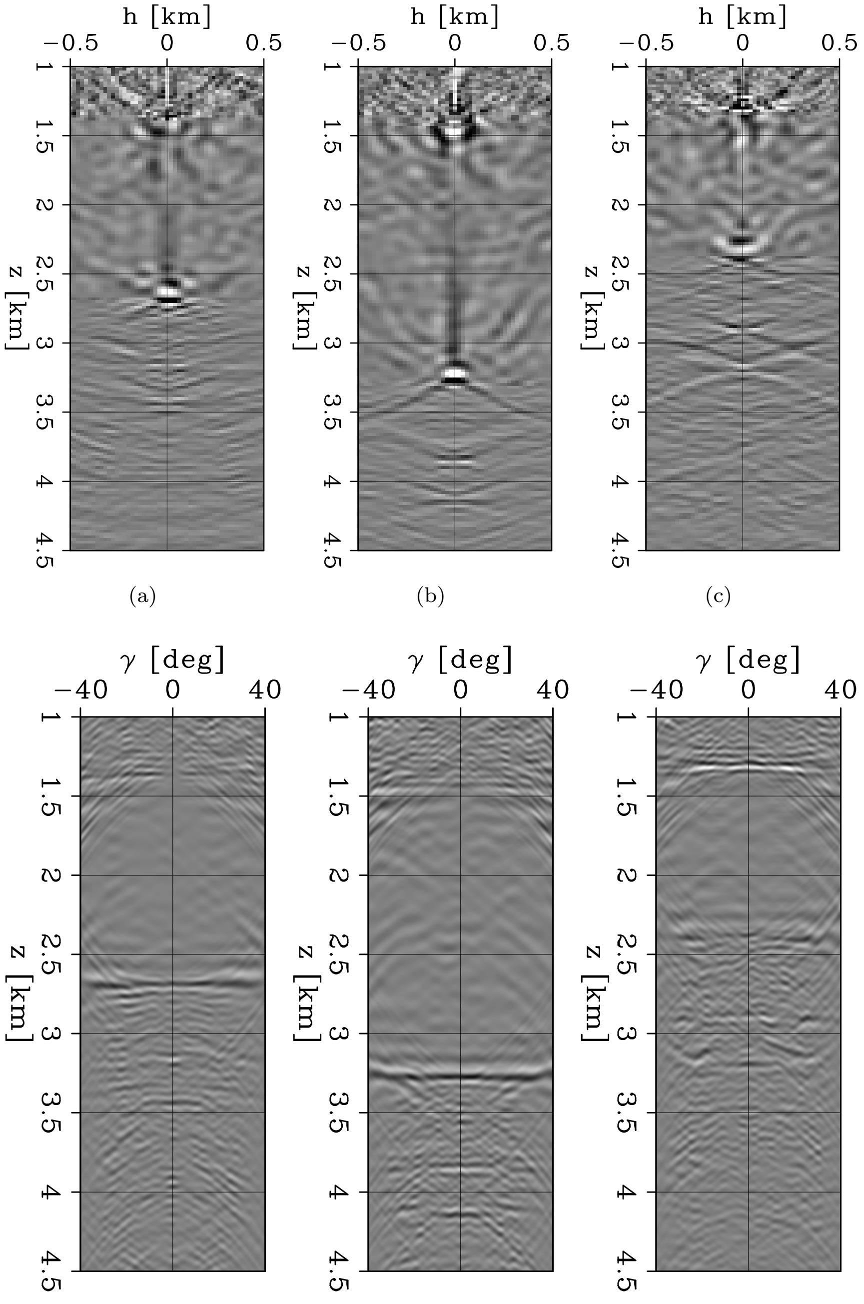

(a) (b) (c)

(d) (e) (f)

Figure 3.18: Final ODCIGs obtained after iteratively migrating the data shown in Figure 3.16b extracted at $x = 5.5$ km (a), $x = 10.0$ km (b), and $x = 14.0$ km (c), respectively. ADCIGs extracted at $x = 5.5$ km (d), $x = 10.0$ km (e), and $x = 14.0$ km (f), respectively. [**CR**]

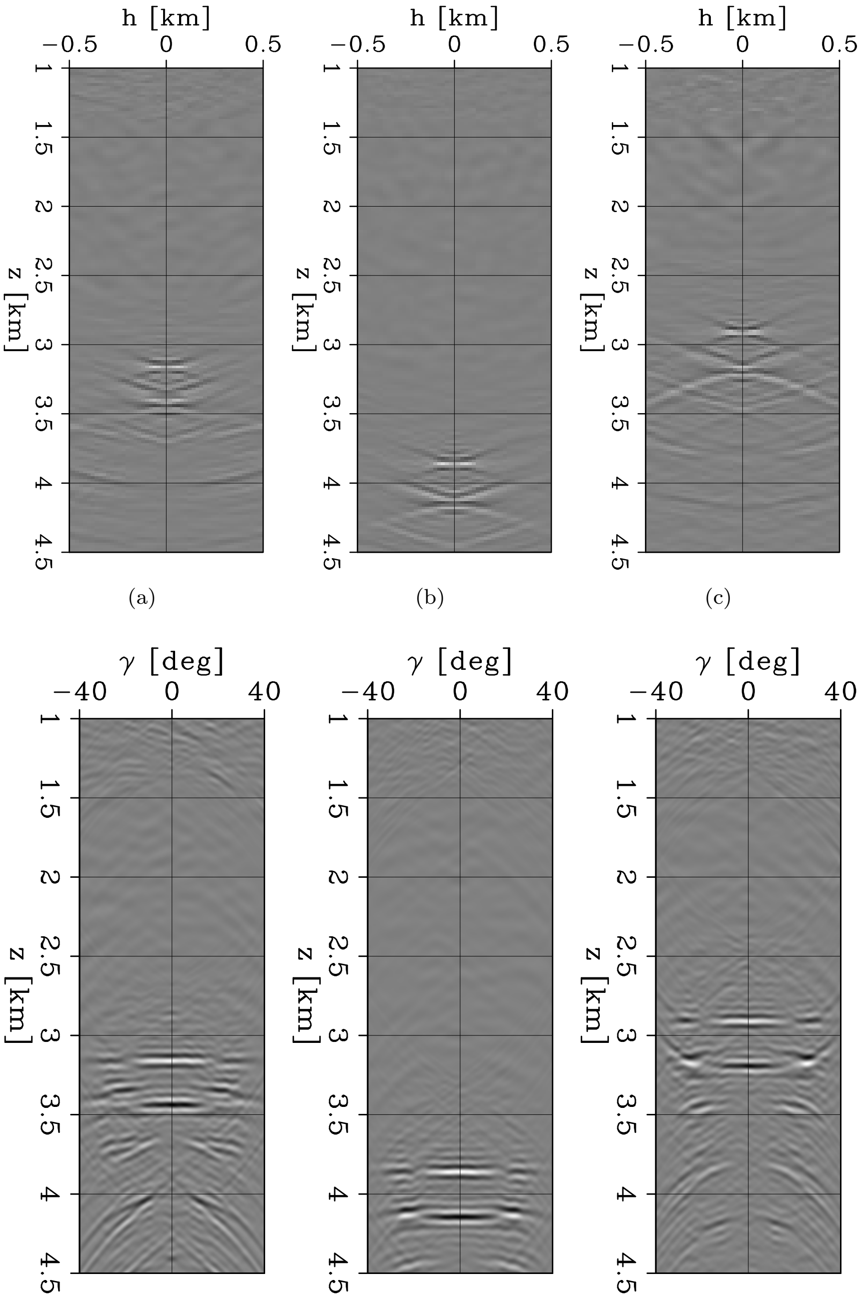

(a) (b) (c)

(d) (e) (f)

Figure 3.19: Final ODCIGs obtained after iteratively migrating the data shown in Figure 3.16c extracted at $x = 5.5$ km (a), $x = 10.0$ km (b), and $x = 14.0$ km (c), respectively. ADCIGs extracted at $x = 5.5$ km (d), $x = 10.0$ km (e), and $x = 14.0$ km (f), respectively. [**CR**]

As shown by Prucha and Biondi (2002), the image artifacts related to shadow zones and incoherent illumination can be mitigated by forcing coherency across reflection angles during the migration step. In this test, to impose such a condition, I add a DSO regularization term to the waveform objective functions (equation 2.64). I solve the regularized imaging problems using 500 iterations of the linear CG approach. The regularization weight ϵ is chosen based on trial and error. An initial guess for this variable is represented by a value that balances the two objective function terms for a non-null reflectivity model. The regularization weights chosen for the two datasets are different. A larger weight has been employed for the dataset shown in Figure 3.16b than the one in Figure 3.16c.

The regularized extended-image solutions in both cases are more focused in the offset domain and present a more coherent angle behavior in the resulting ADCIGs compared when the inversion problems are not regularized (Figure 3.20 and 3.21). Moreover, most of the imaging artifacts are greatly diminished; especially, for the migration of the dataset containing the salt-related events (Figure 3.16b).

To show the importance of forcing coherency across reflection angles, I compare the amplitude responses of the ADCIGs extracted at the depth corresponding to the top of the sand lenses against the theoretical Zoeppritz Rpp coefficients (Figure 3.22). The unregularized process produces an image whose amplitudes are affected by the inconsistent illumination and migration artifacts. On the contrary, the regularized ADCIGs present smoother angle responses that are consistent with the theoretical Rpp. The mismatch at angles greater than 24° is due to the lack of illumination from the surface acquisition geometry.

When only the sand-lenses related events are linearily inverted, the ADCIGs angle response is less impacted by the image artifacts due to salt-related multiples and converted events. In this case, the regularization provides a mild improvement (Figure 3.23). Nevertheless, the addition of regularization permits the formation of an image whose amplitudes show a quasi-perfect matching of the theoretical response up to 24° reflection angles. The comparison of Figures 3.22 and 3.23, underlies even further the dependency of the image amplitudes on the events considered during the migration process.

Figure 3.24 shows the zero-angle image when the entire data volume is imaged without any regularization term (i.e., dataset of Figure 3.16b). The usage of the regularization term within the migration problem greatly diminishes the image artifacts. A simple stacking procedure across angles for the un-regularized inversion result can also diminish such artifacts (Figure 3.24c). Within the stacked and regularized images, the salt shape is perfectly captured, and the contours of the subsalt sand lenses are visible. The regularized zero-angle image is more interpretable than the angle-stacked one. It is generally less affected by artifacts where the bottom interface of the middle lens can be clearly recognized. Some artifacts affect the image quality and could be further diminished with filtering, but this step is out of this work scope. Nonetheless, a useful subsurface image can be obtained without complex workflows and can be employed to perform a structural analysis of the

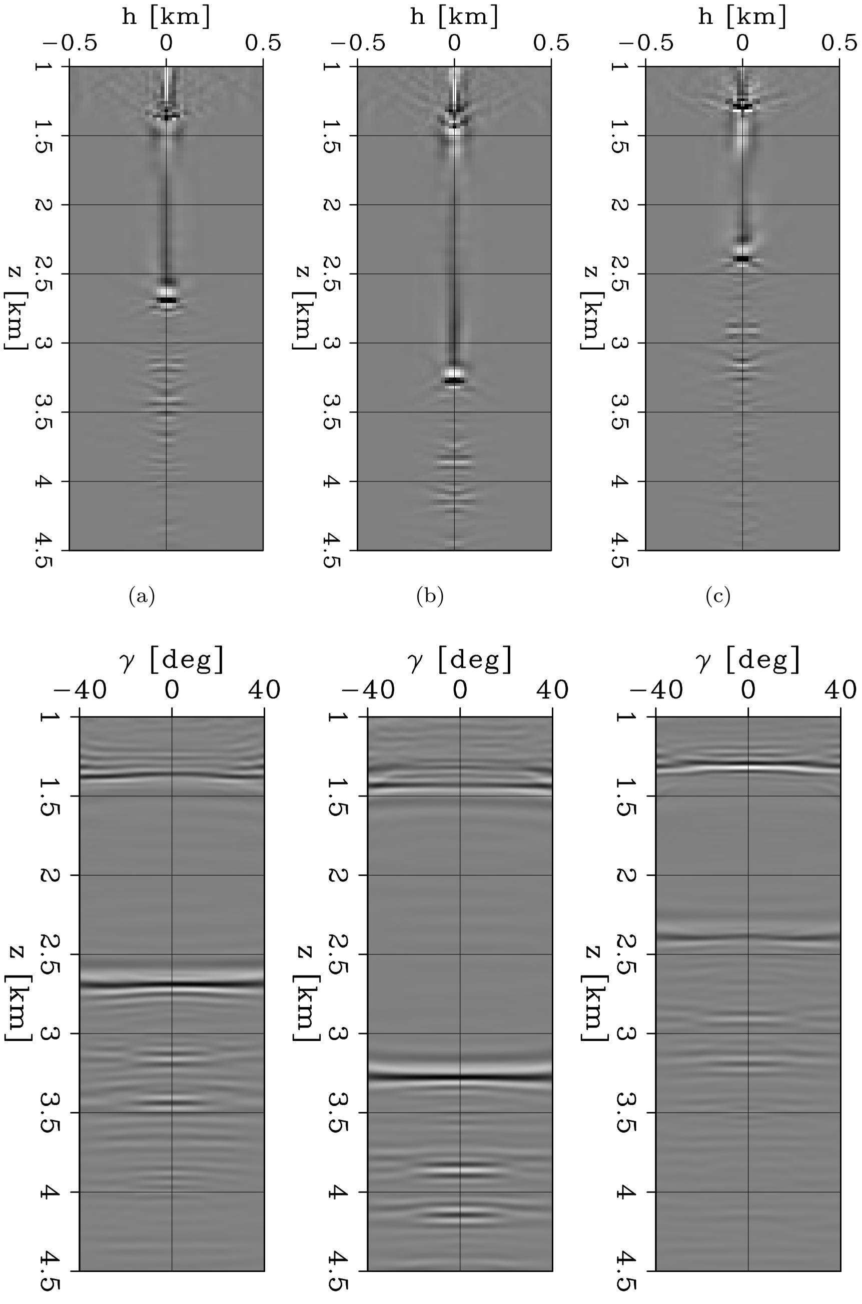

(a) (b) (c)

(d) (e) (f)

Figure 3.20: Final DSO-regularized ODCIGs obtained after iteratively migrating the data shown in Figure 3.16b extracted at $x = 5.5$ km (a), $x = 10.0$ km (b), and $x = 14.0$ km (c), respectively. ADCIGs extracted at $x = 5.5$ km (d), $x = 10.0$ km (e), and $x = 14.0$ km (f), respectively. [**CR**]

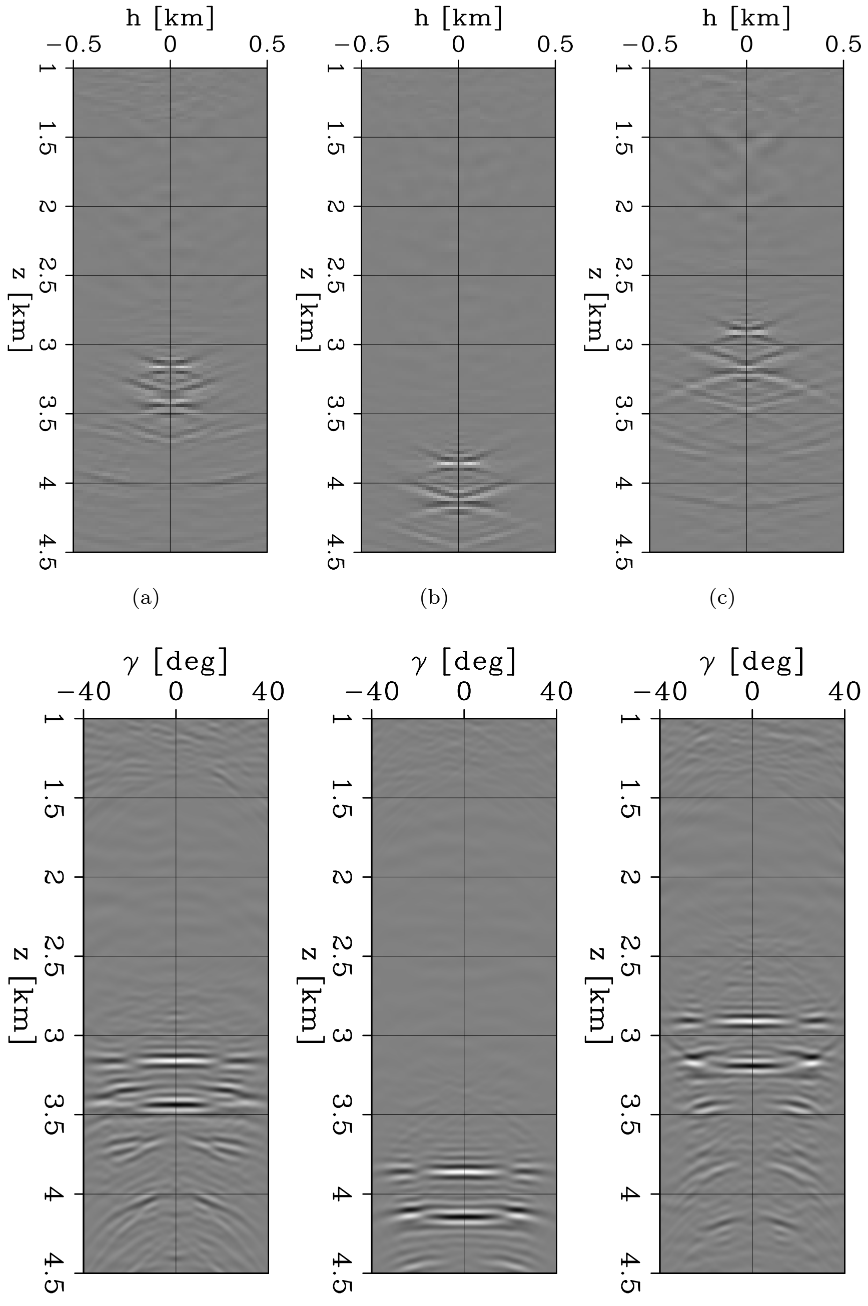

(a) (b) (c)

(d) (e) (f)

Figure 3.21: Final DSO-regularized ODCIGs obtained after iteratively migrating the data shown in Figure 3.16c extracted at $x = 5.5$ km (a), $x = 10.0$ km (b), and $x = 14.0$ km (c), respectively. ADCIGs extracted at $x = 5.5$ km (d), $x = 10.0$ km (e), and $x = 14.0$ km (f), respectively. [**CR**]

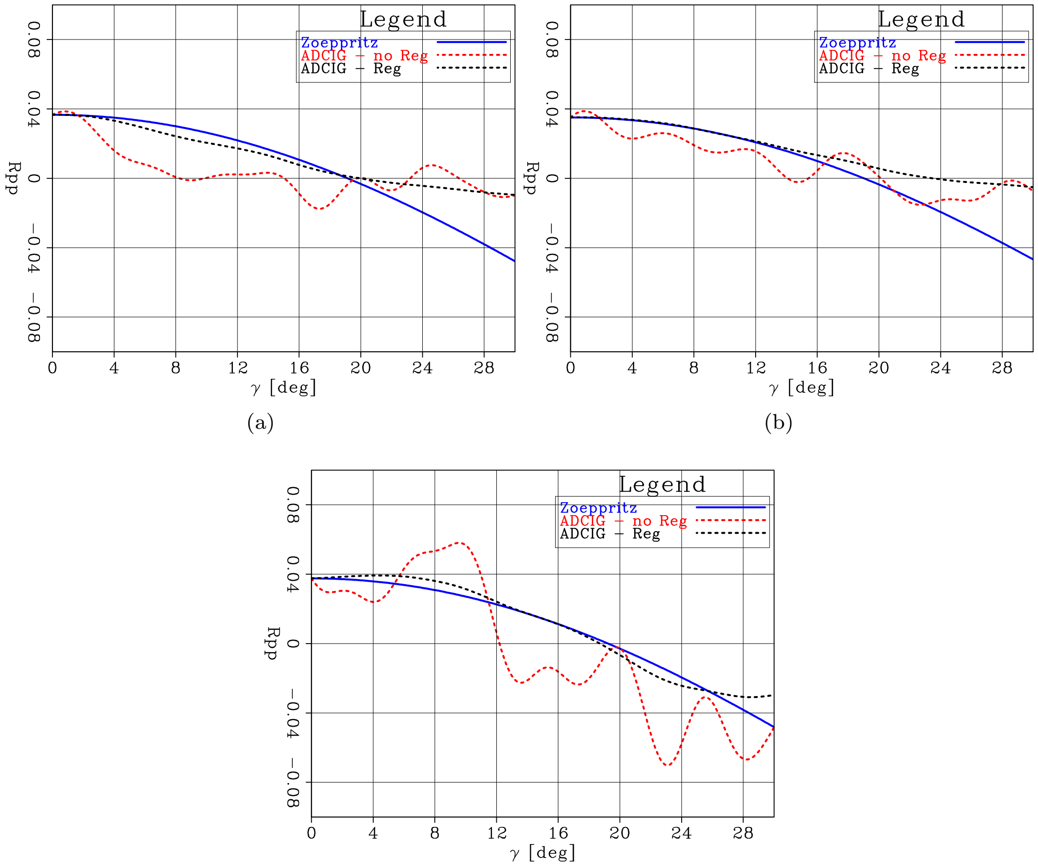

(a) (b)

(c)

Figure 3.22: Comparison between of the PP reflection coefficient of the top of the three lenses when all the events are migrated (Figure 3.16b). Amplitude-response comparison for the left (a), middle (b), and right (c) lenses. Each panel shows the angle responses for Zoeppritz equation prediction (blue curve) and the ADCIG amplitudes without (red dashed) and with DSO regularization (black dashed) extracted at the corresponding lenses top interface. [**CR**]

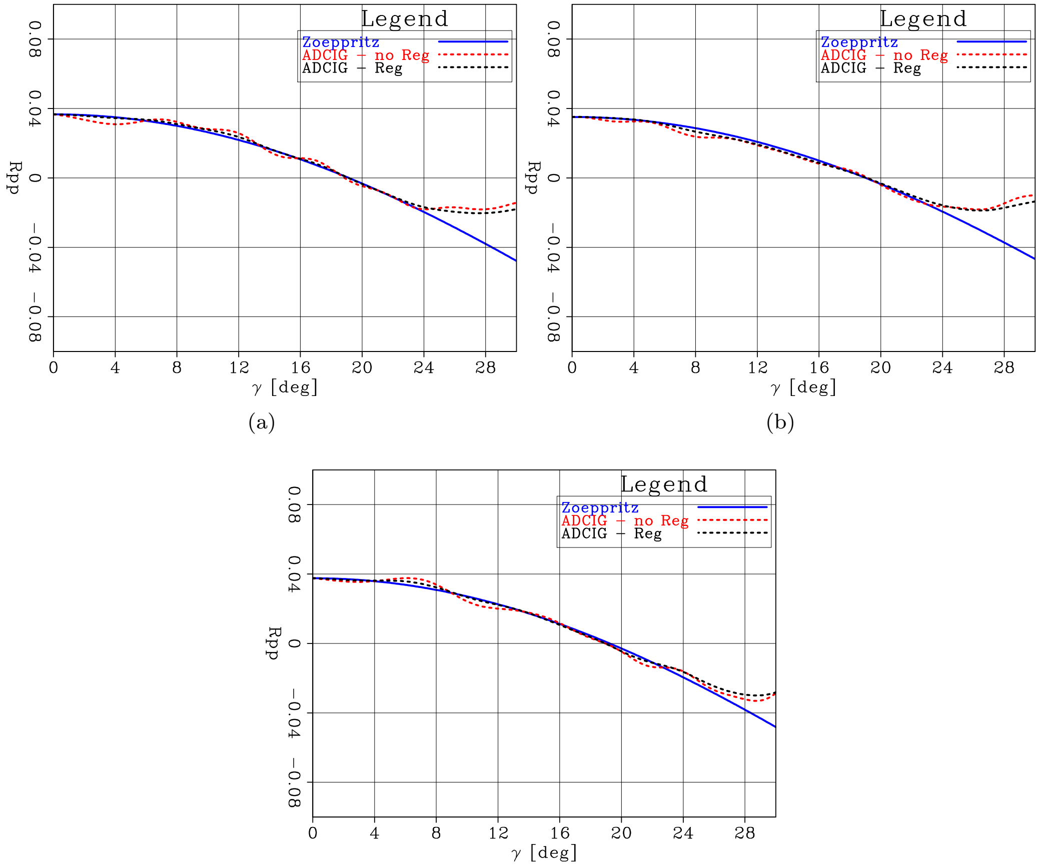

(a) (b)

(c)

Figure 3.23: Comparison between of the PP reflection coefficient of the top of the three lenses when the only lens-related events are migrated (Figure 3.16c). Amplitude-response comparison for the left (a), middle (b), and right (c) lenses. Each panel shows the angle responses for Zoeppritz equation prediction (blue curve) and the ADCIG amplitudes without (red dashed) and with DSO regularization (black dashed) extracted at the corresponding lens top interfaces. [**CR**]

subsurface interfaces.

The subsalt lens test clearly demonstrates the extended-image space's ability to form true-amplitude migrated volumes even when Born acoustic operators are used during linearized inversion of elastic pressure data.

3.2 Target-oriented elastic FWI

In this section, I demonstrate using 2D numerical tests how the extended image space can synthesize elastic pressure data as if the acquisition geometry is sunk into the subsurface. First, I show how this image-based redatuming is applied on the flat-layer model previously described. Then, I use the redatuming technique on elastic pressure data generated on the Marmousi2 to retrieve the elastic properties associated with a gas-bearing sand reservoir only within the target area. I compare elastic FWI results of this target obtained using the surface and the reconstructed data and report the computational speed-up factor achieved by the target-oriented inversion approach (Martin et al., 2006).

3.2.1 Redatuming of elastic pressure waves through extended linearized waveform inversion

As explained in the previous chapter, the extended image space can be used to reconstruct elastic pressure data as if the acquisition geometry was sunk into the subsurface. In this synthetic example, I demonstrate this possibility by synthesizing elastic data obtained from the flat-interface model of Figure 3.1. The goal is to use the elastic pressure data recorded at $z = 0$ km and reconstruct the one as if the sources and the receivers could have been placed at 400 m below the surface. Figure 3.25 displays two representative shot gathers obtained when the acquisition geometry is placed at $z = 400$ m. The same amplitude-versus-offset behavior is observed as in the surface pressure data (Figure 3.4).

The schematic of Figure 2.2 shows that a scattering point can be used to generate the surface and the sunk acquisition datasets. This observation also implies that the images obtained from two acquisitions, assuming infinite source-receiver extent, are identical. To demonstrate this statement, I compare the ODCIGs obtained by inverting the surface and sunk-acquisition data, respectively (Figures 3.26a and 3.26b). The only difference between the two ODCIGs is due to the limited acquisition aperture (Figure 3.26c).

Since the data from the two acquisition geometries maps into the same extended image, I can use the ODCIGs obtained from the surface pressure to synthesize the events recorded by the sunk sources and receivers. Figure 3.27a shows the shot gather at $x = 2.0$ km obtained by demigrating the ODCIGs of Figure 3.26a. A similar amplitude behavior is present compared to the shot gather of Figure 3.25b up to an offset of 1 km. The artifacts above the apex of the reflected event are due

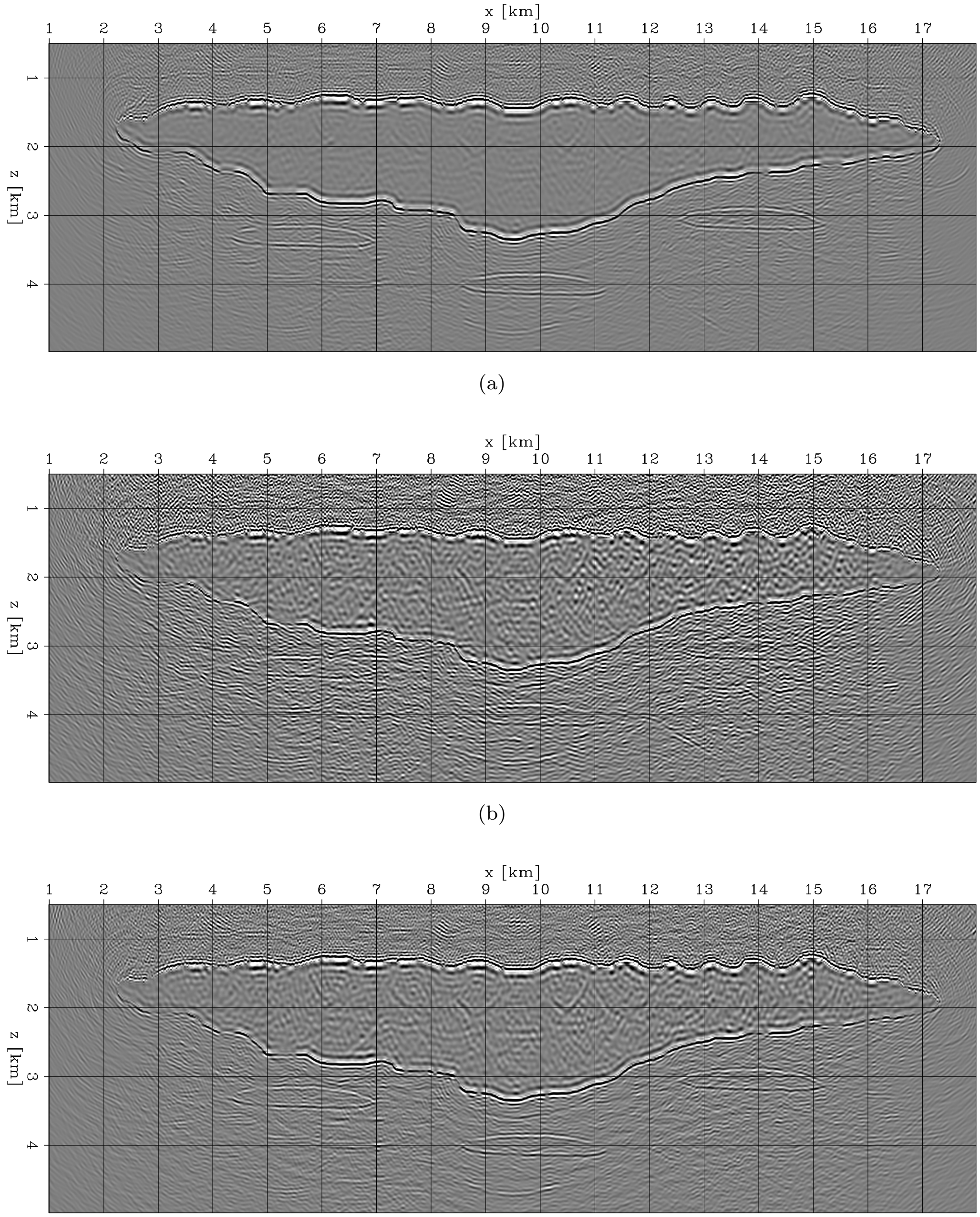

(a)

(b)

(c)

Figure 3.24: Zero-angle image when the entire data volume is imaged with (a) and without (b) a regularization employed during the inversion process. (c) Stacked image obtained by stacking the un-regularized linearized waveform inversion result across reflection angles for $\gamma \leq 10°$. [**CR**]

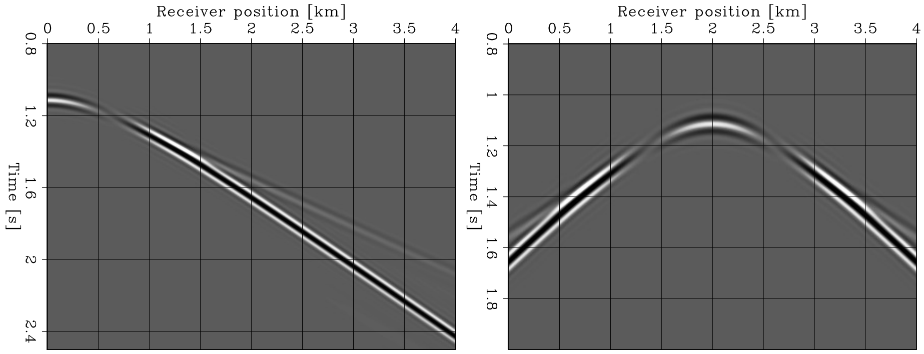

(a) (b)

Figure 3.25: Representative elastic pressure shot gathers for sources placed at (a) $x = 0.0$ km and (b) $x = 2.0$ km generated using the single flat interface model of Figure 3.2 and with an acquisition depth of 400 m. [**ER**]

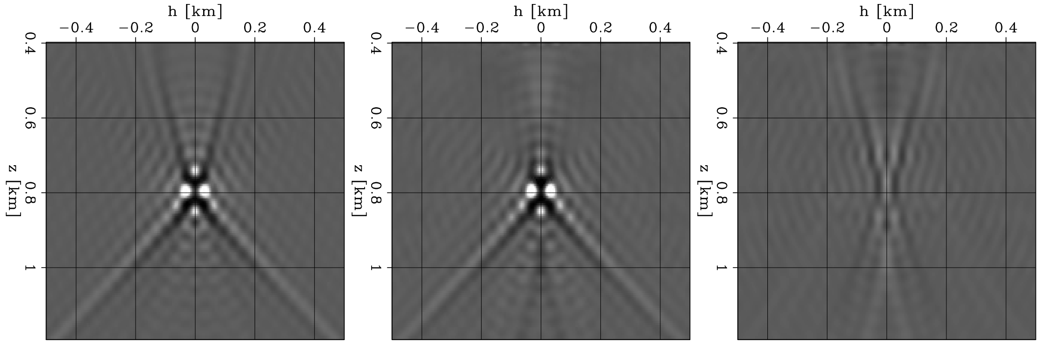

(a) (b) (c)

Figure 3.26: (a) Close-up of the ODCIG of Figure 3.6b. (b) ODCIG generated by solving a linearized waveform inversion using the buried acquisition geometry. (c) Difference between panels (a) and (b). All panels are displayed using the same gain. [**CR**]

to the truncation of the surface acquisition geometry. In fact, when I demigrate the image where those truncation artifacts are masked (Figure 3.27b), the reconstructed reflection does not present any spurious events (Figure 3.27c).

As I described using the schematic of Figure 2.3, not all the events associated to any source-receiver pairs can be reconstructed from an image obtained with surface data. In this case, the maximum illuminated reflection angle from the surface geometry is approximately 64°, which corresponds to a maximum half-offset of 1 km for the sunk acquisition geometry. Figure 3.27d shows the difference between the reference and the reconstructed data of Figures 3.25b and 3.27c, where only energy for an offset greater than 1 km are present as expected.

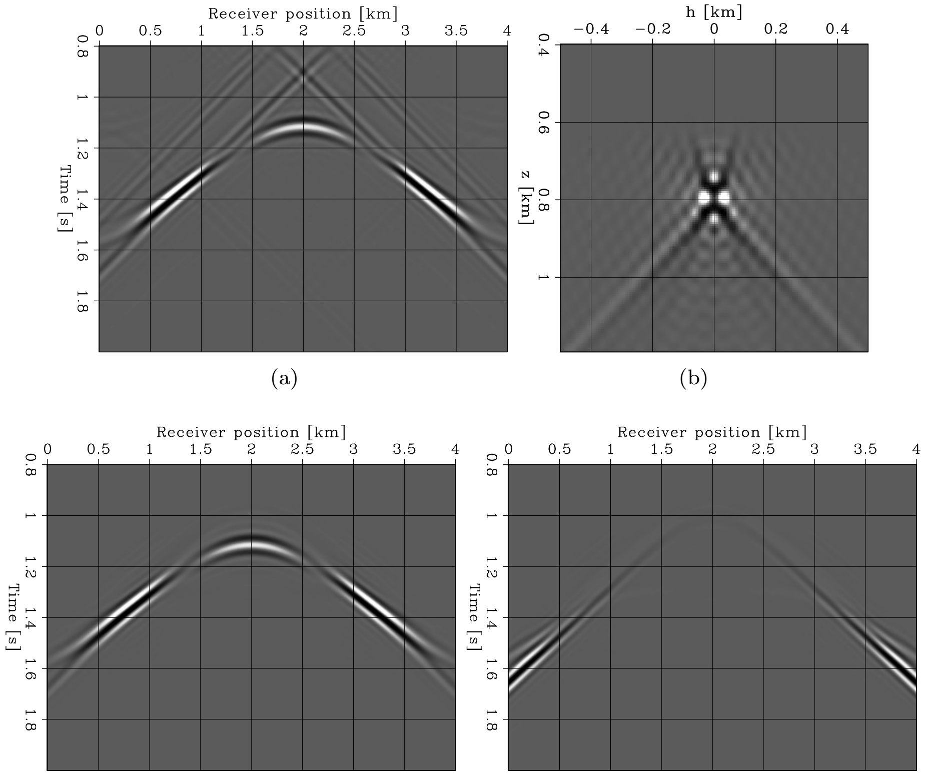

(a) (b)

(c) (d)

Figure 3.27: (a) Elastic pressure reconstructed by demigrating the surface ODCIGs. (b) ODCIG of Figure 3.26a where a muting mask has been applied to dampen the acquisition artifacts above *o*.6 km. (c) Reconstructed pressure data obtained by demigrating the ODCIGs where a image mask has been applied. (d) Difference between panel (c) and the one of Figure 3.25b. [**CR**]

Sensitivity to assumed source wavelet

Since the redatuming technique is based on an imaging step, it is necessary to create a source wavelet signature. However, the data reconstruction is invariable to the choice of the source signature. To numerically verify this statement, I reconstruct the same events of Figure 3.27c, but employing different waveforms during the linearized waveform inversion and demigration steps. Figure 3.28a displays the same wavelet of Figure 3.3a on which a 90-degree phase rotation has been applied. The right panel in Figure 3.28b shows a Ricker wavelet with a domain frequency of 15 Hz. These two waveforms are independently used to solve the extended linearized waveform inversion problem defined on the flat-interface model (Figure 3.1). The extended gathers generated by this process are then used to reconstruct the elastic pressure events at the new datum (i.e., 400 m).

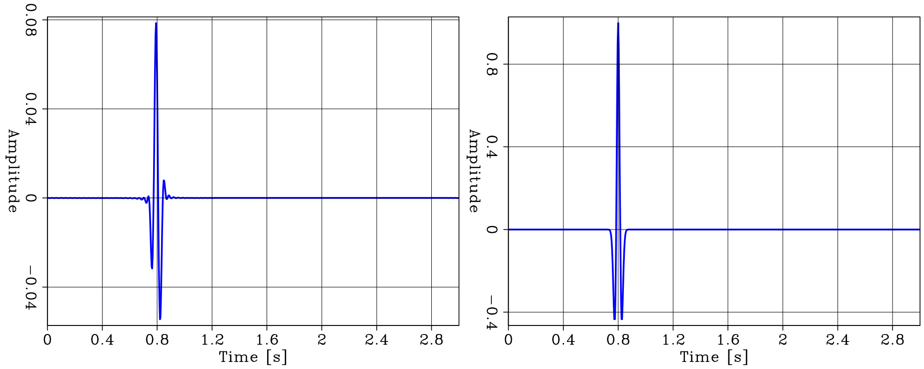

(a) (b)

Figure 3.28: Time-domain wavelet plots for testing invariability of the data reconstruction procedure. (a) Wavelet where a 90-degree phase rotation has been applied to the original signal. (b) Ricker wavelet with dominant frequency of 15 Hz. [**ER**]

Figure 3.29 shows the redatumed pressure when the 90-degree rotated waveform and the Ricket wavelet are employed during the demigration process, respectively. No evident difference is visible when these two panels are compared to the one displayed on Figure 3.27c.

This invariability can also be seen by analyzing the amplitude behavior of the ADCIGs generated by the extended linearized waveform inversion when different wavelets are employed. In fact, the same AVA pattern is visible in the three panels of Figure 3.30 showing the ADCIGs generated with three source signatures described in this section.

Finally, I analyze the sensitivity of the reconstruction process with respect to the migration velocity map used during the linearized waveform inversion step. To this end, I perform the same redatuming steps previously described for the flat-interface case but in which a 5% slower velocity is used compared to the correct one (i.e., 2375 m/s). As expected the ODCIG obtained during the migration process is not as focused as when the correct velocity is employed (compare Figures 3.31a and 3.25a). Moreover, the typical curving effect within the angle gather is observed when analyzing

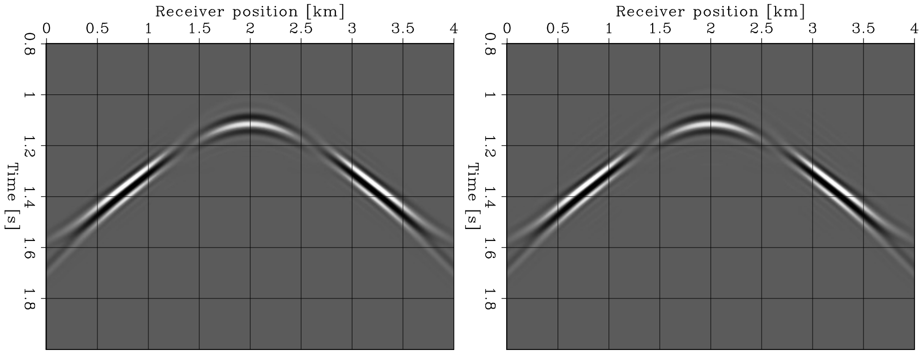

(a) (b)

Figure 3.29: Pressure data reconstructed from the extended images obtained using the wavelets signals of Figure 3.28 [**CR**]

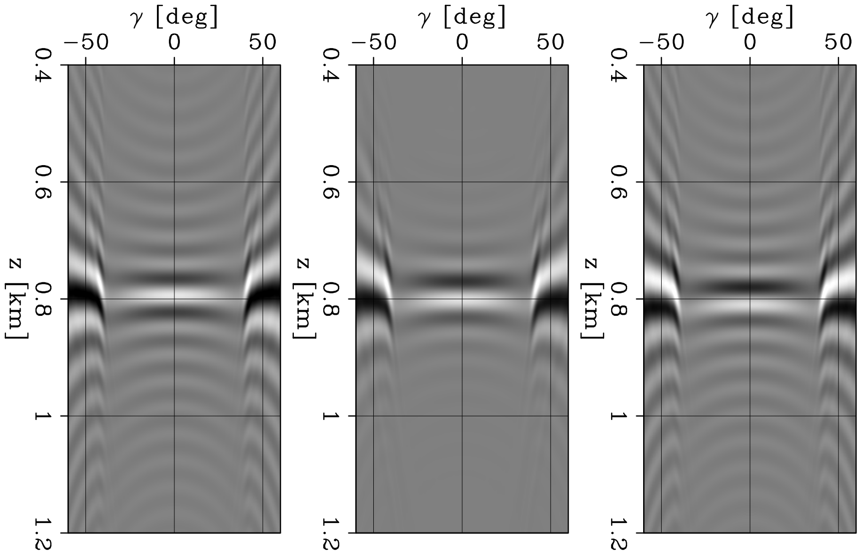

(a) (b) (c)

Figure 3.30: ADCIGs extracted at x = 2.0 km for the extended images obtained using: (a) the correct signature, (b) the 90-degreee rotated signal, and (c) the Ricker wavelet, respectively. [**CR**]

Figure 3.31b (Biondi and Symes, 2004).

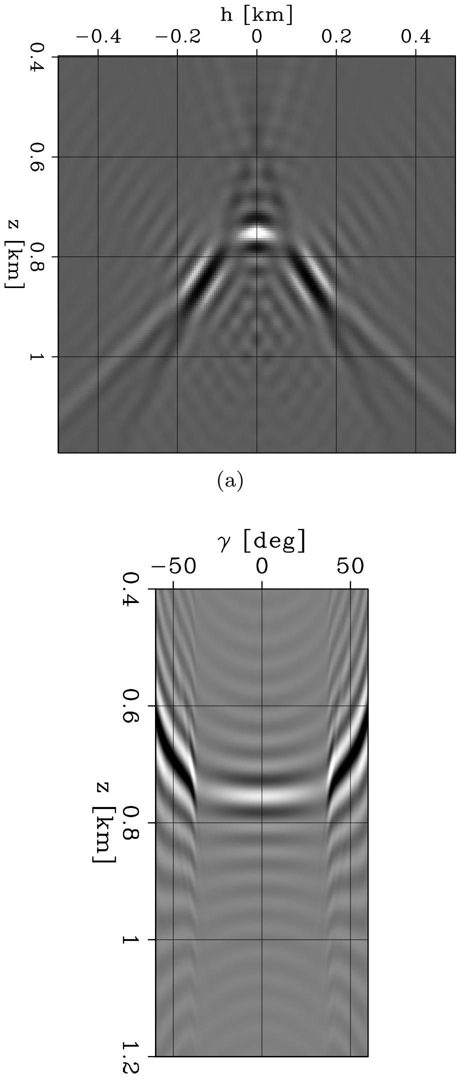

(a)

(b)

Figure 3.31: (a) ODCIG and (b) ADCIG extracted at $x = 2.0$ km on the extended image obtained from the surface pressure migrated employing a constant velocity model of 2375 m/s. [**CR**]

When the ODCGIs obtained using the slower migration velocity are demigrated to reconstruct the datumed elastic pressure, the AVO pattern is reconstructed but the kinematics of the events result incorrect (Figure 3.32).

This test demonstrates the importance of obtaining an accurate migration velocity model of the overburden before performing the redatuming step. This observation is generally true to any other redatuming technique. However, the proposed technique, since it is based on an imaging step,

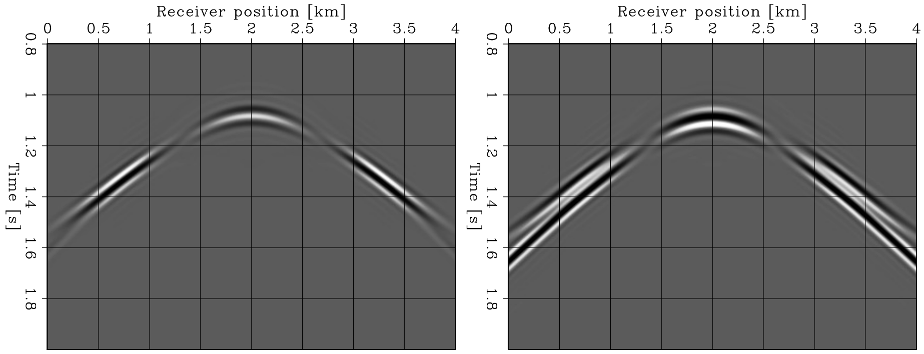

(a) (b)

Figure 3.32: (a) Reconstructed pressure using the extended image obtained using an incorrect velocity model. (b) Difference between panel (a) and the shot gather of Figure 3.25b. [**CR**]

provides a quality control step thanks to the kinematic behavior of the generated ODCIGs and ADCIGs with respect to the migration velocity model.

3.2.2 Elastic target-oriented inversion applied to the Marmousi2 model

I apply the previously described redatuming technique on the Marmousi2 model to estimate the elastic parameters associated with a gas-bearing reservoir located within a faulted anticline structure. The true subsurface elastic parameters are displayed in Figure 3.33. This gas reservoir is located at a depth of 1.1 km and spans approximately 500 m in the horizontal direction, starting from $x = 10$ km.

First, I apply an elastic FWI workflow to a surface dataset to retrieve the entire model's subsurface parameters starting from a smoothed version of the true model. Then, I solve an extended linearized waveform inversion to synthesize the reflected events generated by the gas reservoir recorded with an acquisition located in its vicinity. The redatumed dataset is then used within the same elastic FWI workflow to estimate the reservoir's elastic properties. Finally, I compare the target-oriented results with the elastic FWI applied to the entire surface dataset.

The observed elastic pressure data is generated from a surface acquisition composed of 140 sources and 567 receivers spaced by 120 m and 30 m along the x-axis, respectively. Figure 3.34a shows the time signature of the explosive source employed in this synthetic experiment. This wavelet's frequency content is effectively contained between 4 and 13 Hz with a flat response between 6 and 10 Hz (Figure 3.34b). The choice of the lowest frequency wants to simulate a field scenario in which the low-frequency content is commonly removed given its low signal-noise-ratio (SNR).

Given the amplitude response of the reflected events from the subsurface interfaces, the dataset is mostly dominated by reflections. In fact, by analyzing the two representative shot gathers displayed

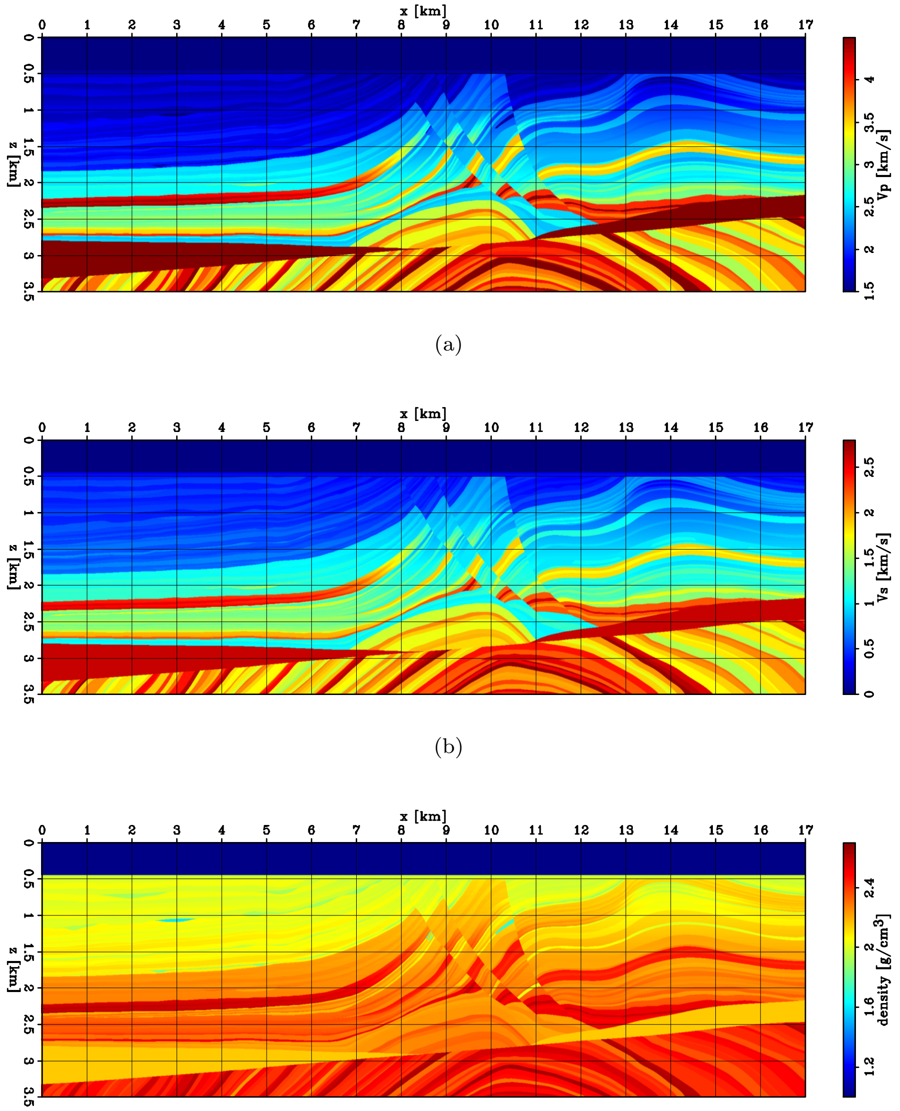

(a)

(b)

(c)

Figure 3.33: Elastic parameters of the Marmousi2 model. From top to bottom: (a) P-wave velocity, (b) S-wave velocity, (c) density. [**ER**]

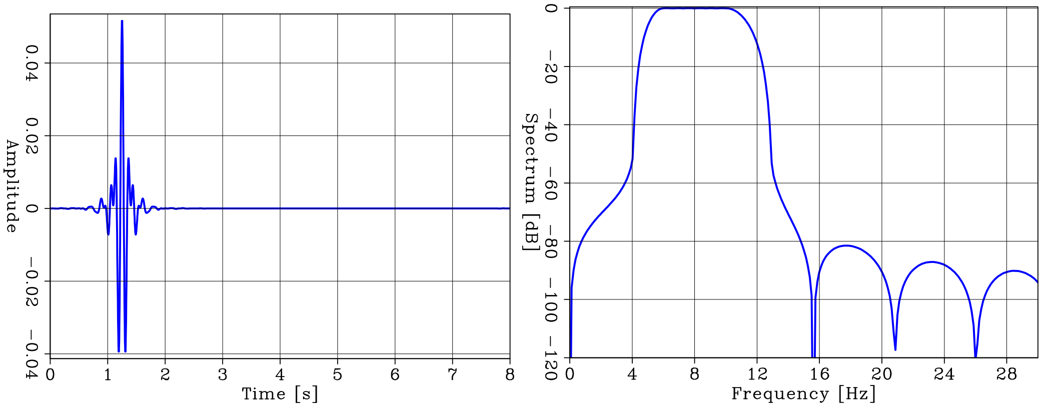

(a) (b)

Figure 3.34: Explosive source used to generate the elastic pressure data on the elastic Marmousi2 model. Panel (a) and (b) show the time signature and frequency spectrum, respectively. [**ER**]

in Figure 3.35, the mentioned reflections present greater amplitudes than the transmitted waves. This presence of these reflected events represents the ideal application scenario for the redatuming technique. The linearized waveform inversion process can map the AVO of the reflected events within the extended image space.

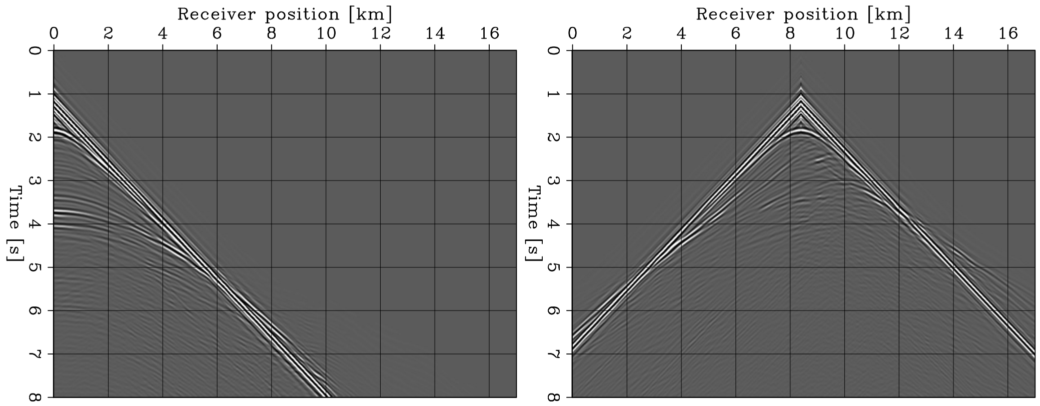

(a) (b)

Figure 3.35: Representative elastic pressure shot gathers for sources placed at (a) $x = 0.0$ km and (b) $x = 8.5$ km on the Marmousi2 model. [**ER**]

The initial elastic parameters are obtained by applying a moving average filter to the true model (Figure 3.36). This process produces an accurate initial elastic model and mitigates the possibility of falling into a non-useful local minimum given the chosen frequency content. Additionally, all the short-wavelength features of all the reservoirs present within the subsurface are entirely missing from the initial guess.

The full bandwidth of the data is simultaneously injected, and the three elastic parameters are jointly inverted within an elastic FWI procedure. Moreover, I apply the model-space multi-scale approach described in the previous chapter in order to mitigate the presence of local minima and mitigate any spatial artifacts that may arise during the inversion process. Three sequentially refined spline grids are employed, namely, 100 m, 50 m, and 25 m spacing, while the propagation is performed with a 5 m sampling in both directions. For each spline grid, the elastic FWI process employs the L-BFGS optimization method, and the inversion is stopped when an appropriate step-length value cannot be found. The convergence curve obtained using the described elastic FWI workflow is shown in Figure 3.37. The first spline grid reaches the closest local minimum after 90 iterations and achieves a relative objective function decrease of more than 80%. The final elastic model is then projected onto a finer spline grid, and other 35 iterations are employed to further diminish the objective function. The spline refinement is performed again to obtain an additional objective function decrease.

The panels in Figure 3.38 show the final elastic parameters obtained at the end of the described elastic FWI workflow. The P-wave velocity is the parameter accurately retrieved and does not present any evident artifacts. On the other hand, the S-wave velocity is affected by some inversion artifacts and a potential cross-talk positioned at $x = 3.0$ km and $z = 1.0$ km. However, overall this parameter is in agreement with the true one shown in Figure 3.33b. The density parameter is also in good agreement with the true one, and the anomaly associated with the gas reservoir is correctly retrieved.

To evaluate the quality of the inverted elastic model, I display the predicted and the observed data within the same plot to compare the amplitude and timing of the reflected event. The representative shot gather is located at $x = 4.190$ km, and only the positive offsets are compared. Figure 3.39a shows this comparison when the observed data are plotted along with the predicted pressure obtained using the initial elastic model. All the reflected events are not modeled from the initial guess, and a clear mismatch in the long offset events is evident. On the contrary, after applying the FWI workflow, the predicted data using the inverted elastic parameters are in excellent agreement with the observed events.

Despite the elastic FWI workflow's ability to retrieve accurate elastic subsurface parameters from surface data, the overall computational cost makes the method hardly applicable to 3D field datasets. In fact, in this 2D synthetic example, each model point evaluation, which comprised of an objective function and gradient evaluations, took approximately 3 hours on an Intel(R) Xeon(R) Gold 6126 CPU @ 2.60GHz connected to 4 Nvidia Tesla V100-PCIe-16GB graphics processing units (GPUs). In the reported example, 180 model points have been tested, making the total elapsed time approximately 540 hours, corresponding to almost 23 days of computation.

This test shows the high computational cost associated with solving an elastic FWI problem. In

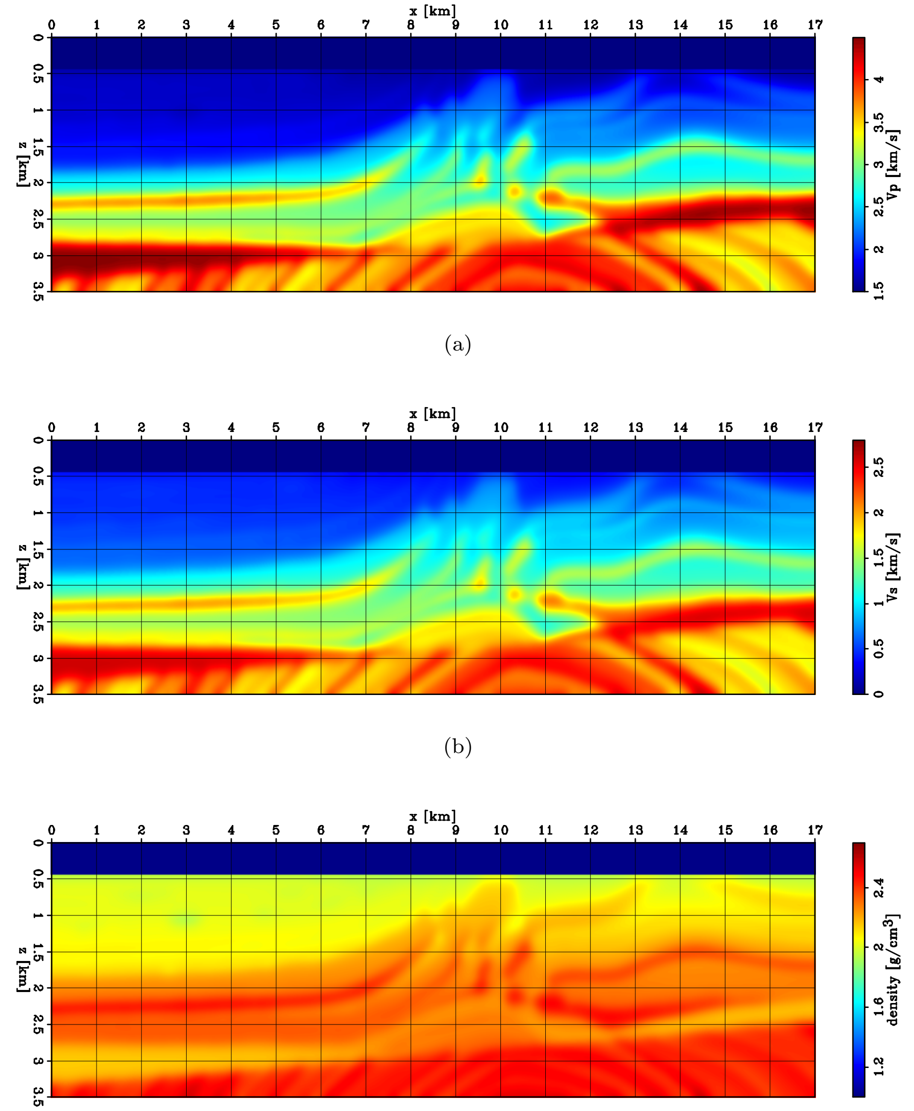

(a)

(b)

(c)

Figure 3.36: Initial elastic parameters obtained by smoothing the sediments composing the Marmousi2 model. From top to bottom: (a) P-wave velocity, (b) S-wave velocity, (c) density. [**ER**]

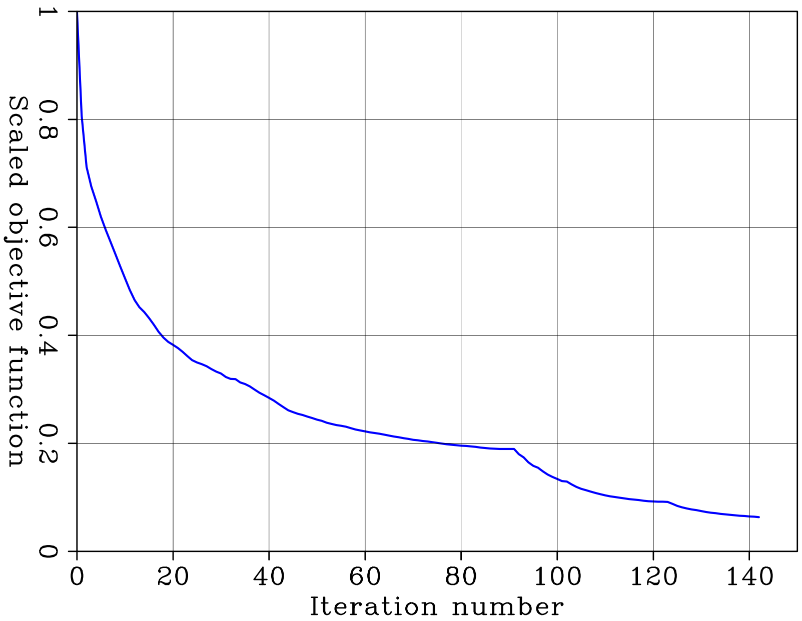

Figure 3.37: Convergence curve of the Marmousi2 elastic FWI problem. The two changes in convexity of the curve at 90 and 125 iterations are due to the change in spline grid of the elastic parameters. [**CR**]

field applications, higher frequencies than those used in this test may contain valuable information on the subsurface. However, the increase of the computational cost as the fourth-power of the maximum frequency highly limits elastic FWI methodologies' applicability at high frequency. The proposed target-oriented technique has the potential of overcoming this limitation. In fact, high-resolution elastic parameters need to be found only within potential areas of interest or hazard (e.g., over-pressured zones, gas pockets, and natural resource reservoirs). These subsurface targets are recognizable from images generated from surface data, making the image-space redatuming and target-oriented elastic FWI subsequent steps of an exploration project.

As previously mentioned, the goal of this test is to characterize the elastic properties associated with a gas-bearing reservoir placed within the faulted anticline structure. The panels on the left column of Figure 3.40 display the elastic parameters of the target structure located at z = 1100 m and x = 10300 m. A clear value-decrease within the P-wave velocity and density parameters is noticeable, while the S-wave velocity does not present such variation. The initial elastic model is obtained by extracting the same parameters from the ones shown in Figure 3.36 and are shown in the panels on the right panels of Figure 3.40.

The smoothed P-wave velocity parameter of Figure 3.36a is employed to solve an acoustic extended linearized waveform inversion of the surface elastic pressure data. I apply 500 iterations of

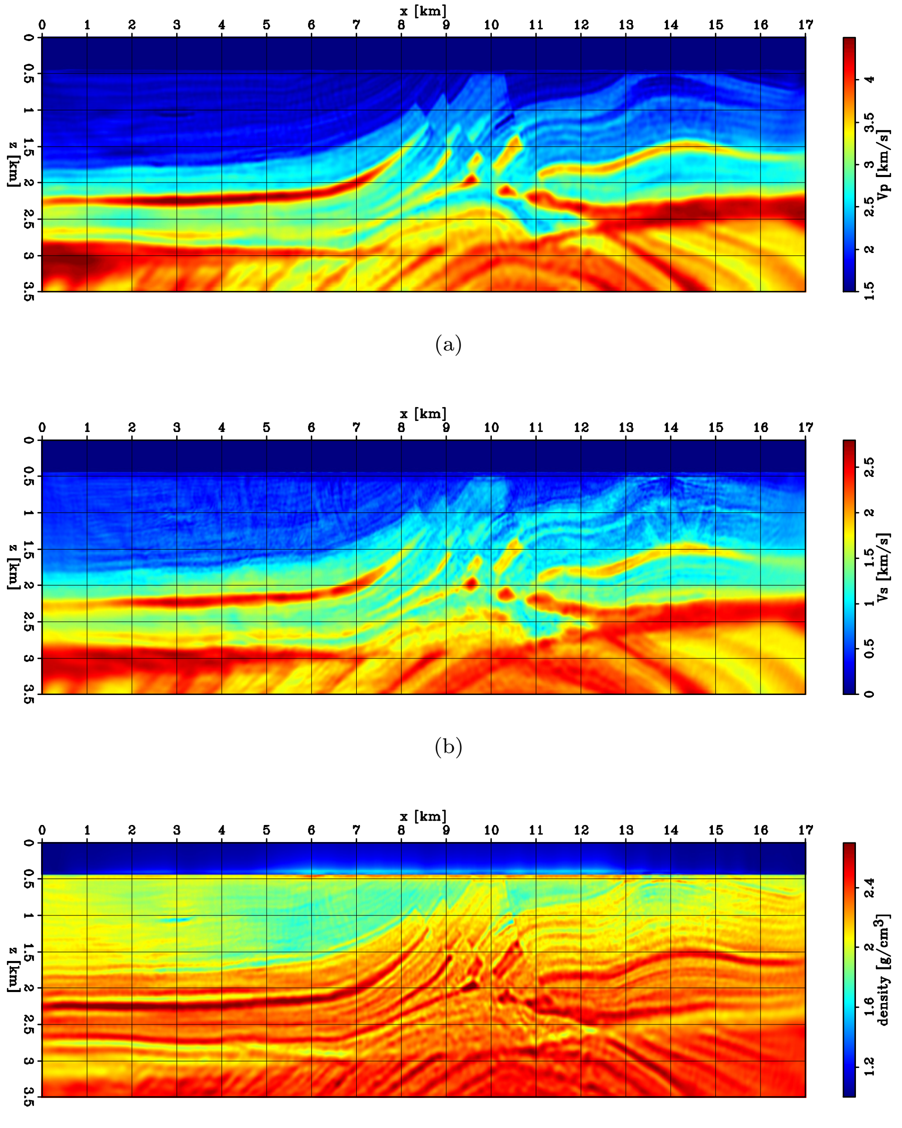

(a)

(b)

(c)

Figure 3.38: Inverted elastic parameters obtained by solving the elastic FWI defined on the Marmousi2 model. From top to bottom: (a) P-wave velocity, (b) S-wave velocity, (c) density. [**ER**]

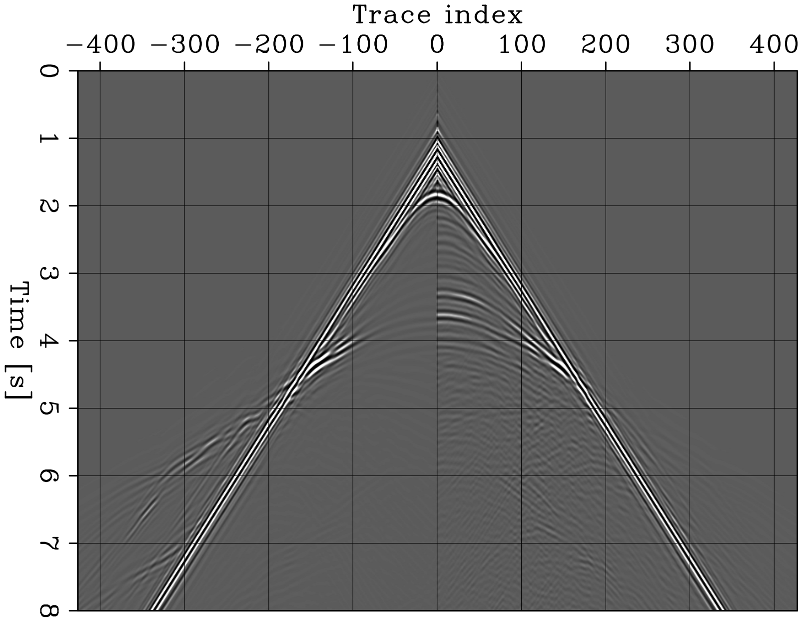

(a)

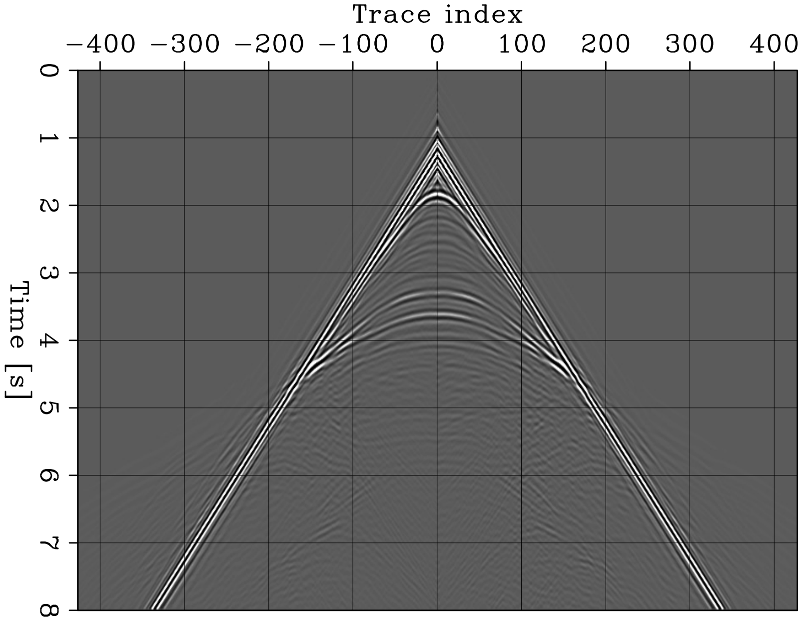

(b)

Figure 3.39: Comparison between the predicted and observed elastic pressure data on the initial (a) and inverted (b) models, respectively. The negative trace indices indicate the predicted data, while the positive ones denote the observed data. [**CR**]

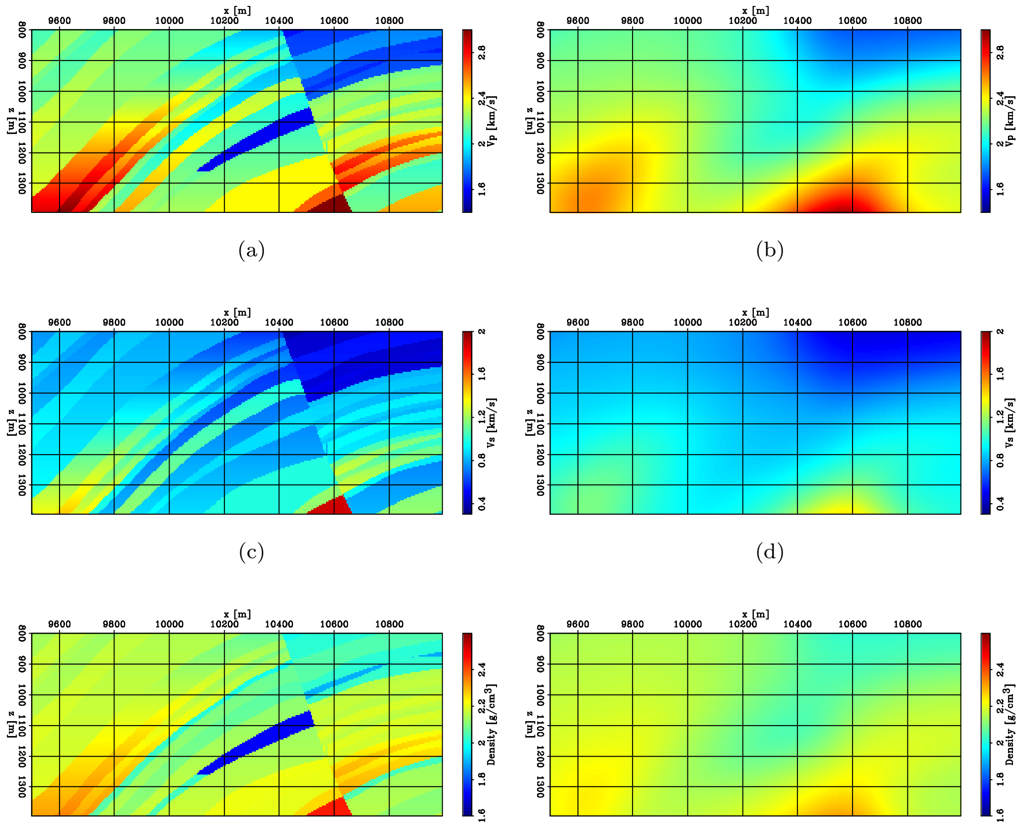

(a) (b)

(c) (d)

(e) (f)

Figure 3.40: True and initial elastic model parameters of the target area plotted on the left and right columns, respectively: (a-b) P-wave velocity, (c-d) S-wave velocity, and (e-f) density. [**ER**]

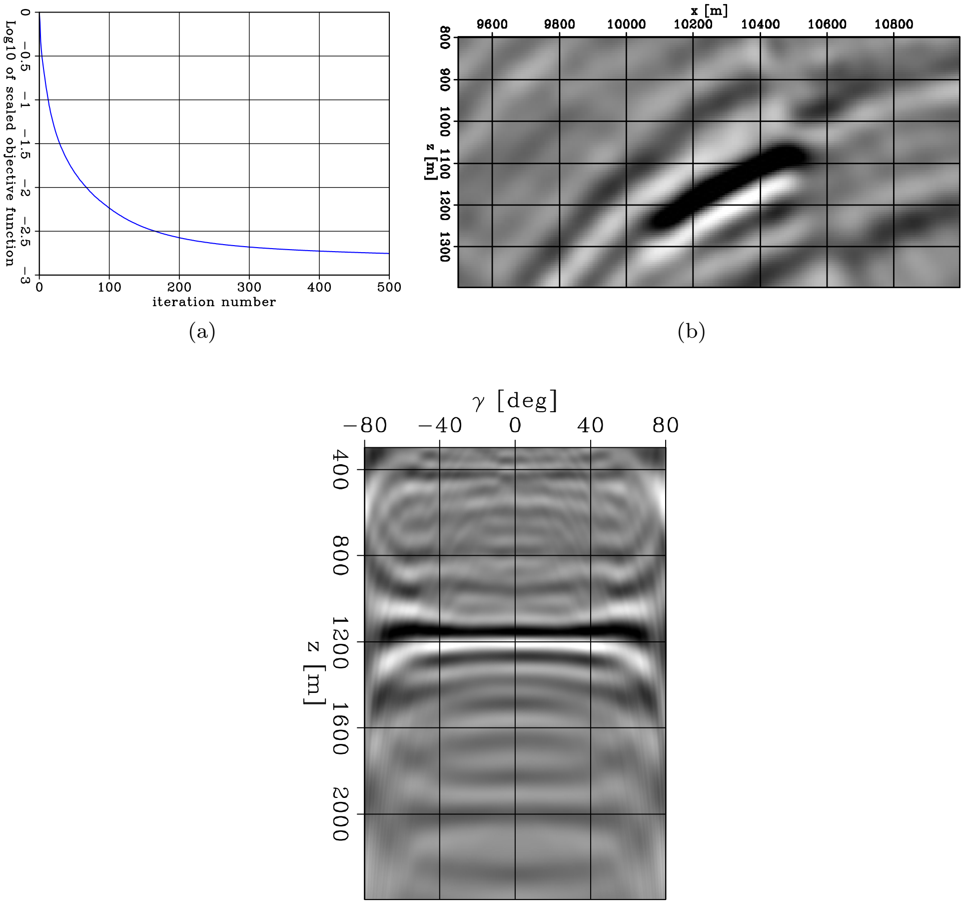

(a)

(b)

(c)

Figure 3.41: (a) Convergence curve of the extended linearized waveform inversion of the elastic data generated on the Marmousi2 model. (b) Zero-subsurface offset image of the target area. (c) ADCIG extracted at $x = 10.3$ km highlighting a high-amplitude event at $z = 1.2$ km associated with the gas reservoir. [**CR**]

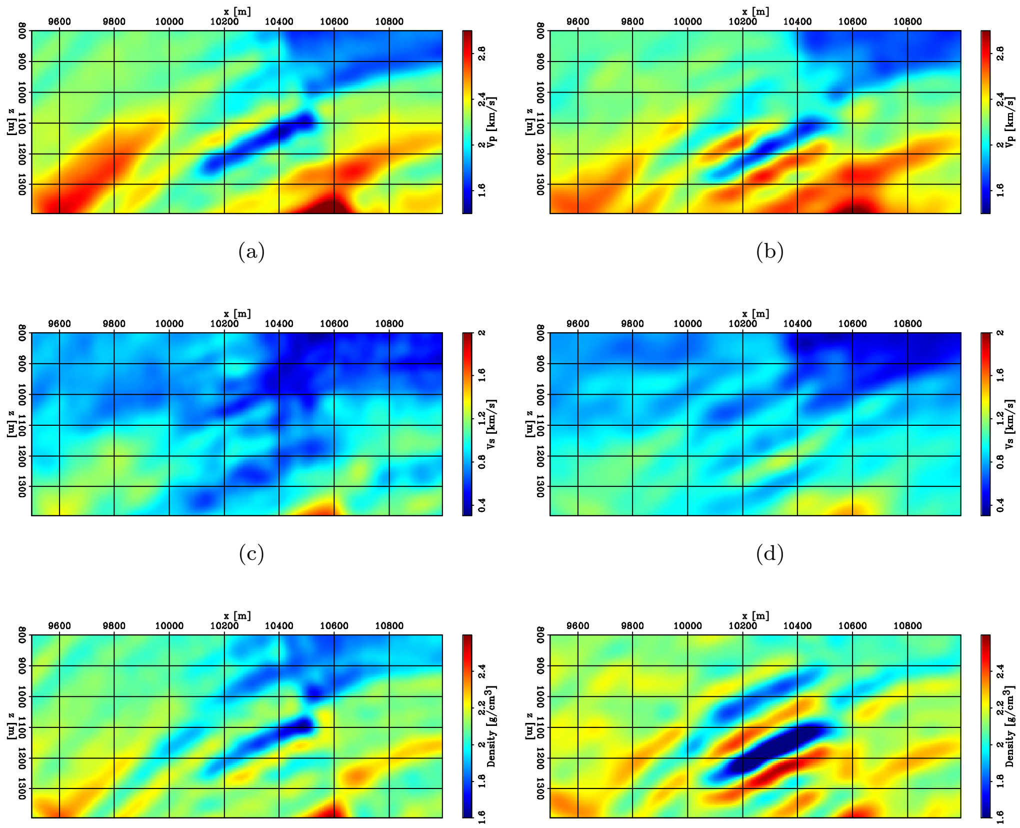

(a) (b)

(c) (d)

(e) (f)

Figure 3.42: Inverted elastic parameters of the target area obtained from the surface data (left column) and the target-oriented approach (right column): (a-b) P-wave velocity, (c-d) S-wave velocity, and (e-f) density. [**CR**]

the linear conjugate-gradient method and to reach the numerical minimum of the problem (Figure 3.41a). Within the zero-subsurface offset image of the target area a high-amplitude response is associated with the reservoir (Figure 3.41b). Additionally, the subsurface structures are correctly imaged since an accurate velocity model has been employed. This observation is also supported by the flat response of ADCIG extracted at $x = 10.3$ km (Figure 3.41c).

The extended image of the target area is demigrated to synthesize the elastic data as if the acquisition geometry was placed in the reservoir's proximity. The elastic pressure is reconstructed assuming 33 sources and 67 fixed receivers spaced every 60 m and 30 m, respectively, and recorded for 4 s. To retrieve the target's elastic parameters, I employ a similar elastic FWI workflow as for the surface data (Figure 3.42). In this case, I only use two spline grid refinements; namely, 50 and 25 m sampling. Overall, 20 iterations of BFGS have been applied to invert the elastic pressure on each spline grid (Figure 3.43). A decrease of 98% is reached after only 40 iterations instead of the 145 needed for the surface-data inversion to achieve the same data fitting level. The P-wave and density parameters of the reservoir gas anomaly are correctly retrieved. No leakage of the gas anomaly is observed in the inverted S-wave parameter. An increase in all three parameters is present right below the reservoir. This artifact is related to the limited frequency range used during the imaging step. Moreover, different regularization weights and image masks applied during the linearized waveform inversion step can diminish this artifact's impact. This test demonstrates the target-oriented approach's ability to retrieve the gas anomaly's elastic parameters and their spatial extent. Compared to the elastic FWI applied to the surface data, the target-oriented inversion is approximately 200 times computationally cheaper, including the migration process, leading to a memory usage decrease of 25 folds. The main computation speed-up is due to the target-oriented inversion workflow's ability to significantly diminish the simulation domain's size compared to the one where the data have been acquired. The imaging step is not as intensive as the elastic inversion. In fact, in the 2D case, the computational cost of elastic Green's function is approximately 12 times higher than the one of acoustic wavefields. This observation is also valid for the 3D case, where this factor can be 30. Moreover, the decrease domain size greatly simplified the implementation of inversion methods because the elastic wavefields can be stored within the computer memory, avoiding the need for applying checkpointing techniques (Anderson et al., 2012). Finally, the computational and memory cost-saving factors can allow the application of elastic FWI methodologies to high-frequency data to reasonable processing time.

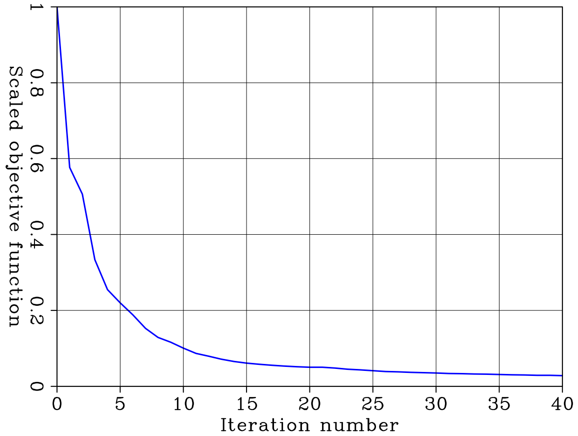

Figure 3.43: Convergence curve of the target-oriented elastic FWI problem. [**CR**]

3.3 Summary

I started this chapter by highlighting the extended image space's ability to preserve the elastic AVO information of pressure data recorded at the surface. Using two synthetic models, I compare the AVA response of the images obtained by solving an extended linearized waveform inversion with the theoretical Zoeppritz PP reflection coefficient and demonstrated their agreement in both examples. Then, I applied the proposed image-based redatuming step to the single-interface case and illustrated some of this process's properties. Finally, I compared the elastic subsurface properties obtained using the proposed target-oriented waveform inversion and a surface-data elastic FWI methodology. This test showed the proposed approach's ability to retrieve the elastic parameters of a potential target for a fraction of the computational cost of inverting the entire surface dataset.

Chapter 4

Deep-water ocean-bottom-node field-data application

In this chapter, I apply the methods described in the previous two chapters to actual data and analyze the improvements in image quality over existing methods. Specifically, I demonstrate the performance of target-oriented elastic FWI workflow to retrieve geophysical parameters of the subsurface using the pressure component of an ocean-bottom-node (OBN) dataset. First, I describe the dataset, and pre-processing steps followed to apply the proposed workflow. Then, I use an acoustic FWI procedure to improve the initial velocity for the proposed method's necessary imaging step. Finally, I synthesize the elastic pressure data generated by a potential prospect positioned on the salt-diapir flank and retrieve estimates of its elastic properties by applying an elastic 3D FWI method.

I employ the inverted elastic parameters to compute two fundamental rock physical parameters (i.e., Vp/Vs ratio and acoustic impedance). I argue the presence of a potential gas-sand prospect positioned on the salt flank. This field-data test illustrates the proposed method's ability to estimate the elastic parameters of target areas within the subsurface using surface seismic data.

4.1 Dataset overview

The field dataset used in this example was acquired within the Gulf of Mexico (GOM) by Shell Exploration and Production Company in 2010. The area sits in the Garden Banks region, about 362km south-west of New Orleans, Louisiana (Figure 4.1). This data aims to illuminate prospects belonging to a producing field to improve the subsurface images around the diffuse salt bodies by leveraging the full wide-azimuth capability of an OBN geometry. The area has been subjected to diffuse diapirism and presents multiple salt bodies making its exploration potentially challenging from a seismic perspective (Murray, 1966; Thompson and Oftebro, 2011).

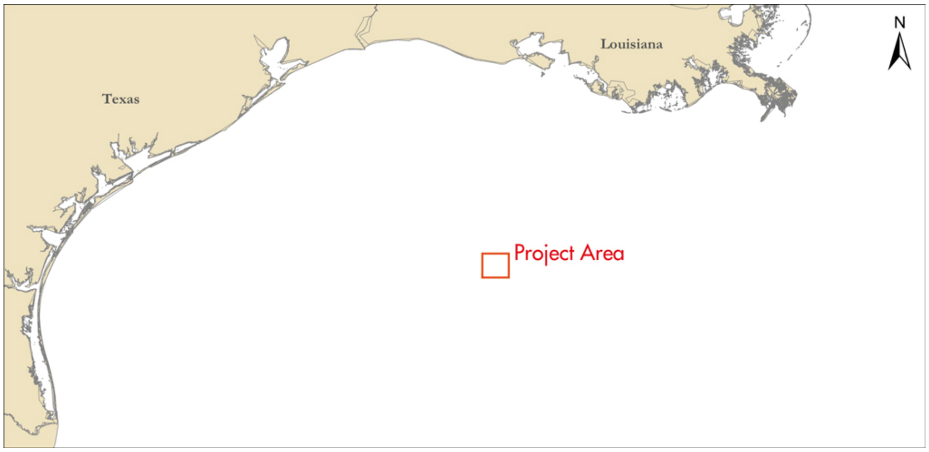

Figure 4.1: Geographic map highlighting the portion of the Gulf Mexico in which the OBN dataset was acquired. [**NR**]

From the entire dataset, I select 255 nodes that recorded multi-component seismic data generated by 41000 air-gun sources covering an area of 100 km^2. Figure 4.2 shows the sources' and nodes' x-y positions overlaid on a depth slice of the initial velocity model depicting a salt diapir (i.e., high-velocity circular portion). The sources have been acquired using a flip-flop acquisition geometry with a source interval of approximately 25 m whose depth is 9.8 m. The sail lines are aligned with the x-axis, and their interval on the cross-line or y-axis is approximately 100 m. From Figure 4.2a, it is clear where the source vessel had to divert its trajectory to abide by the acquisition restrictions in the proximity of production platforms. The multi-component nodes are placed at the seabed, and their depth varies between 0.83 and 1.0 km. Their spatial x-y interval is approximately 250 m in both directions.

4.2 Data description and pre-processing steps

I now show representative plots of the dataset's pressure component and highlight crucial pre-processing steps followed. Applying different high-cut filters to a representative shot-binned common-receiver gather shows that no useful energy is recorded below 2 Hz (Figure 4.3). In contrast, the SNR increases between 3 and 4 Hz. Therefore, the lowest frequency used in this field example is 3 Hz.

To compute a proxy of the direct arrival waveform, I apply a hyperbolic moveout (HMO) correction to all the nodes using a constant velocity of 1.5 km/s (Yilmaz, 2001). By stacking all the traces belonging to a representative common-receiver gather, I obtain the signal depicted in Figure 4.4a. A strong peak is present on the signal's onset, which is then followed by the typical bubble response

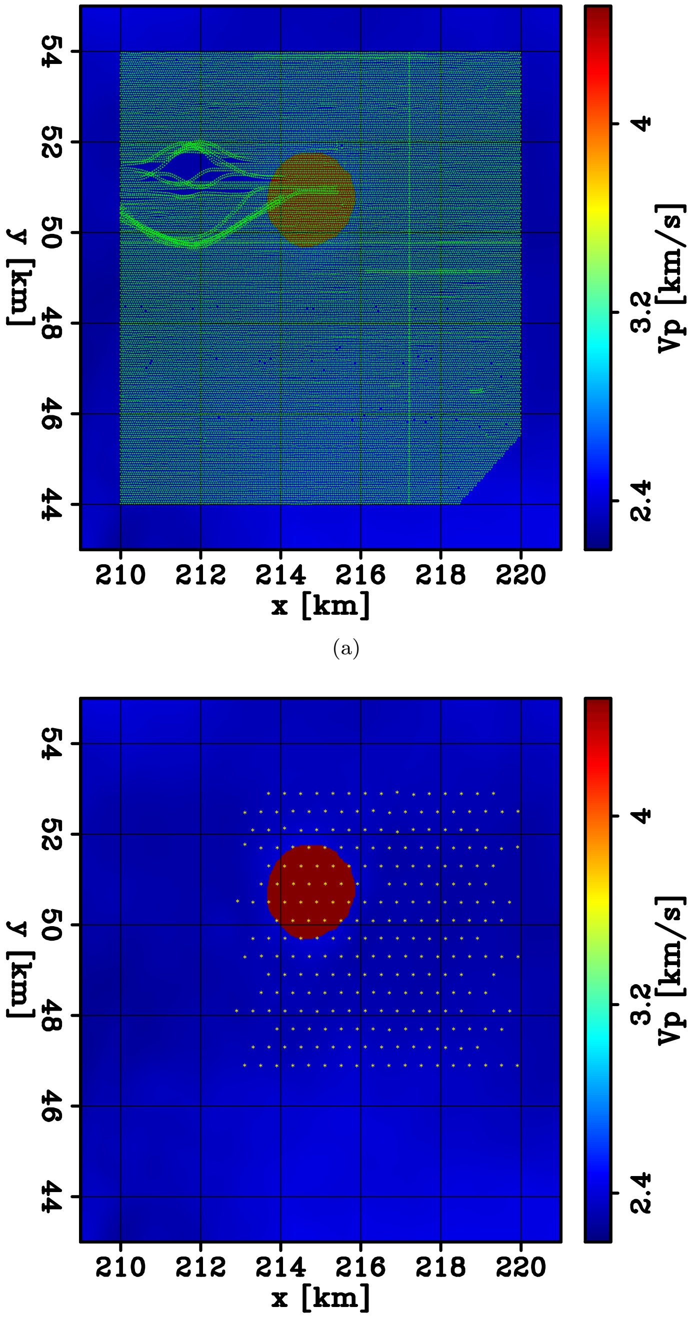

(a)

(b)

Figure 4.2: (a) Sources' and (b) receivers' x-y positions overlaid on the initial velocity model depth slice extracted at $z = 2.5$ km. The high-velocity portion is associated to the presence of a salt diapir. [**ER**]

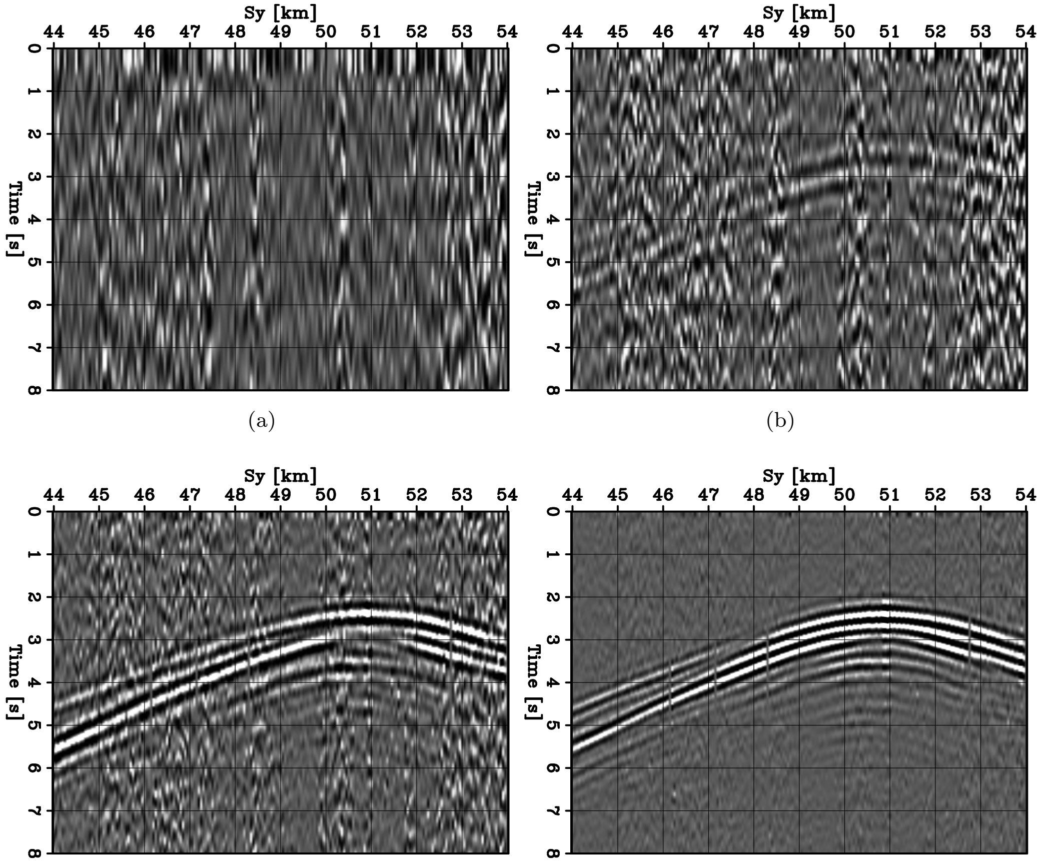

(a) (b)

(c) (d)

Figure 4.3: Representative shot-binned common-receiver gather for $S_x = 214.8$ km on which a low-pass filter has been applied with high-cut frequency of (a) 1, (b) 2, (c) 3, and (d) 4 Hz. [**CR**]

commonly generated by air-gun sources (Watson et al., 2019). The frequency spectrum presents multiple notches due to the source-side ghost and the bubble response (Figure 4.4b). Additionally, the frequency content rapidly decreases after 40 Hz, and very limited energy is present above 160 Hz.

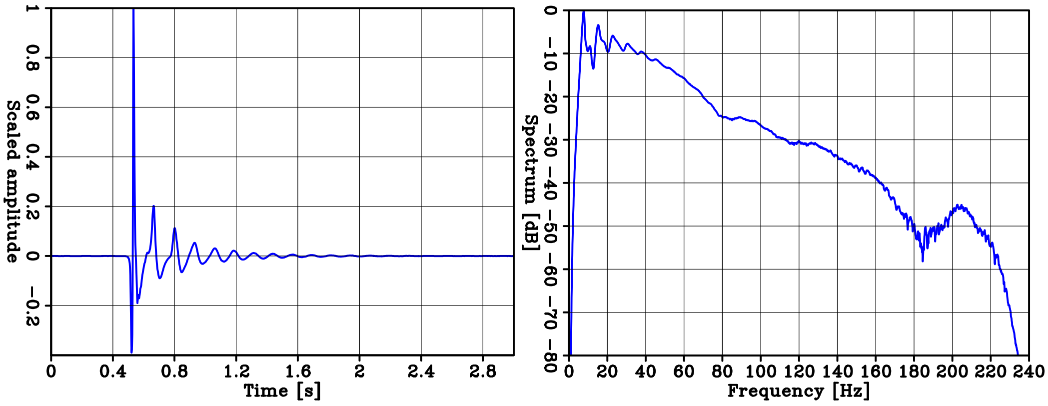

(a) (b)

Figure 4.4: (a) Time- and (b) frequency-domain signature for the observed direct-arrival signature for a representative receiver gather obtained after applying the described HMO correction and stacking procedures. [**CR**]

Shell provided the elastic stiffness components C_{11}, C_{33}, C_{13}, C_{44}, and C_{66} and a constant density value of the sediment layers. It also provided the salt-body edges' positions obtained by interpreting subsurface images of the area. From the stiffness components, I construct an initial P-wave velocity model based on the provided inputs assuming an isotropic medium (Mah and Schmitt, 2003). Figure 4.5 shows representative sections of the 3D volume of the velocity model. The initial sediment velocity does not present any distinguishable geological feature. A salt diapir, reaching the seabed floor depth, is located close to the center of the area of interest whose P-wave velocity is set to 4.5 km/s and is assumed to be homogeneous, a common assumption based on field observations (Zong et al., 2015).

The initial model is used to compute an estimate of the observed data using an acoustic isotropic 3D approximation. I use this pressure prediction to calibrate the modeling operator on the datasets' observed amplitudes and reshape the data response. This step is performed by applying the same HMO correction previously described to both the observed and initially predicted datasets. For each common-receiver gather, I compute the direct arrival proxy following the stacking procedure and shape the observed signal into the predicted one using a frequency-domain Wiener filtering operation. The panels of Figure 4.6 show plots of the observed, initial predicted, and shaped data. The shaping procedure removed the bubble response from the observed data and made the direct arrival waveforms consistent between the initial predicted pressure and the observed data.

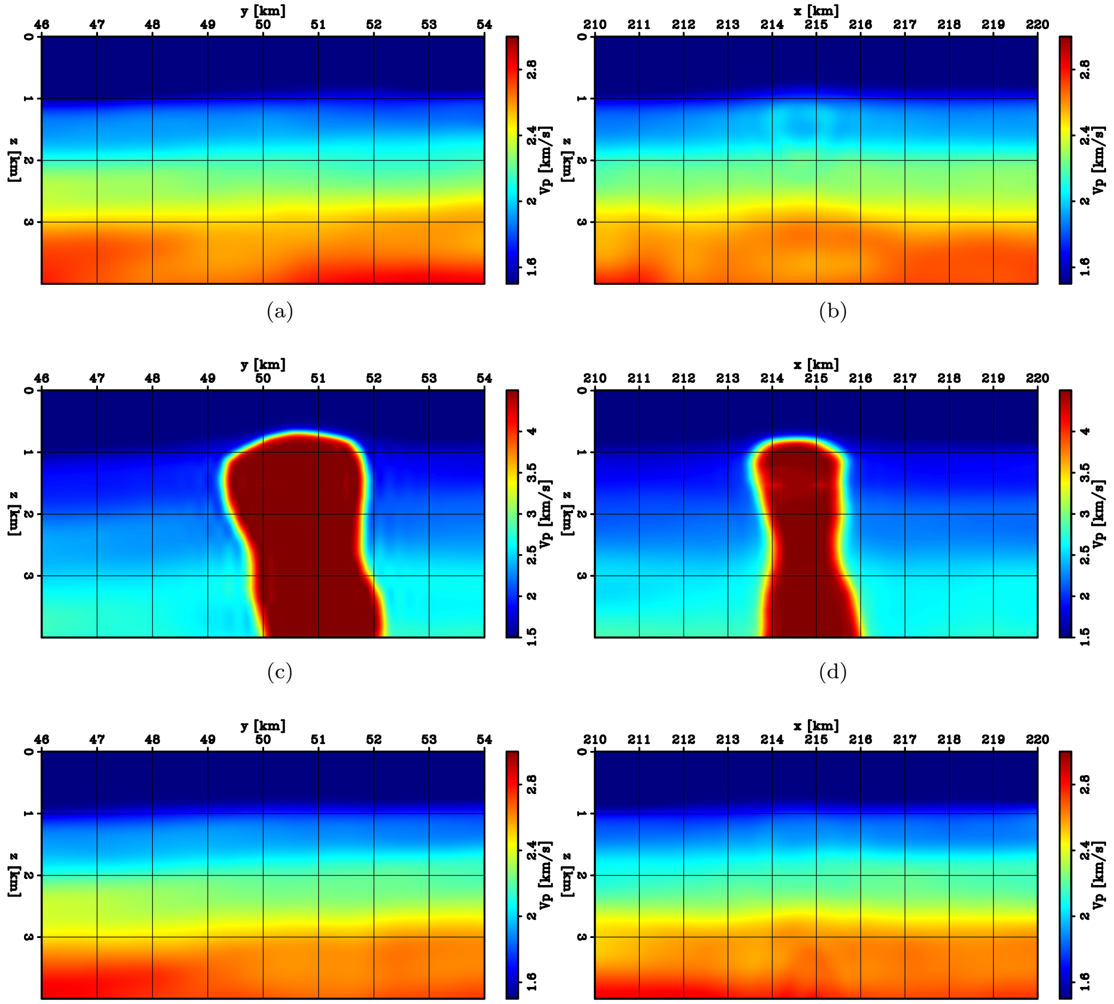

(a)

(b)

(c)

(d)

(e)

(f)

Figure 4.5: Initial interpreted P-wave velocity model of the GOM field application: Cross-line slices at $x = 212$ km (a), $x = 214.8$ km (c), and $x = 217$ km (e). In-line slices at $y = 49$ km (b), $y = 51.5$ km (d), and $y = 52.5$ km (f). [**CR**]

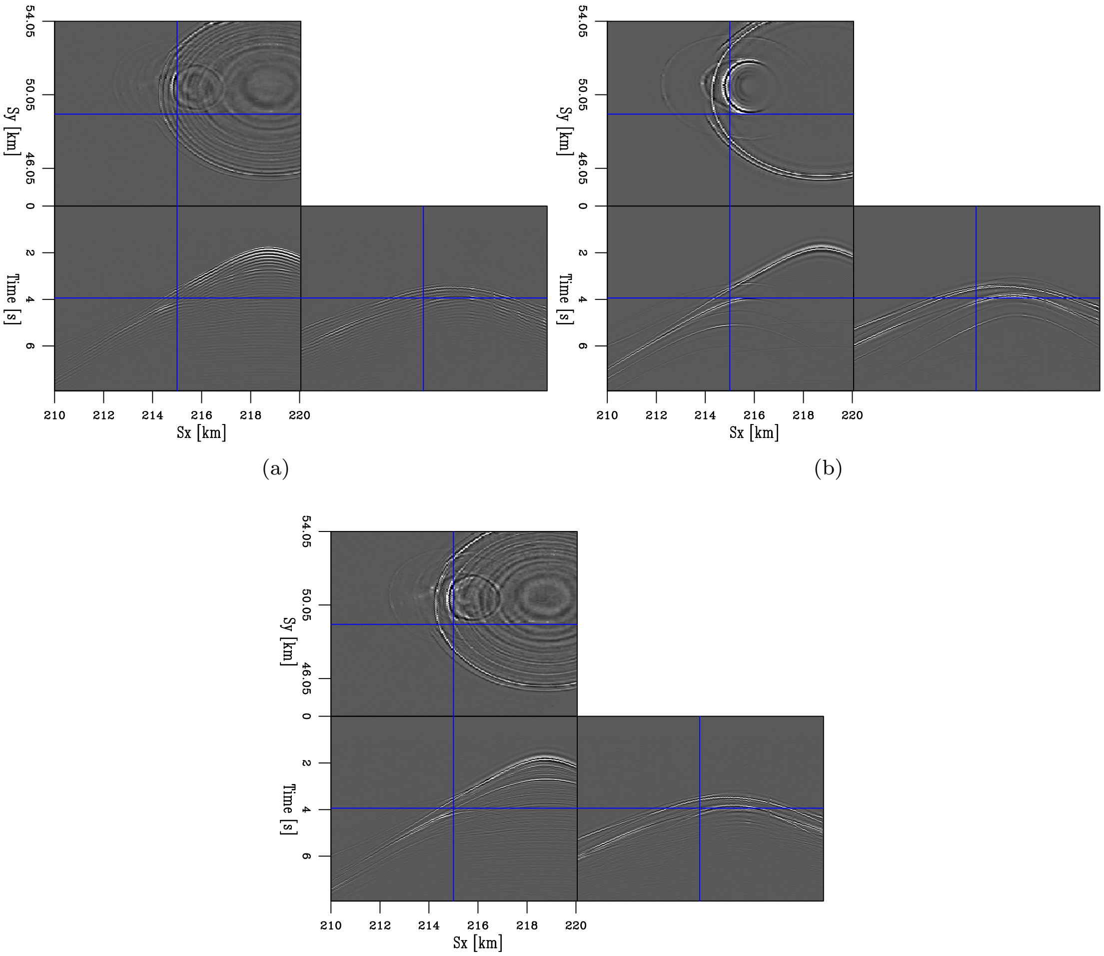

(a)

(b)

(c)

Figure 4.6: Representative common-receiver gather from the (a) observed pressure data, (b) initial prediction, and (c) after the described waveform shaping filtering procedure. The maximum frequency of the plotted data is 20 Hz. [**CR**]

4.3 Initial RTM images and geological scenario description

The shaped data is employed to compute RTM images using the initial P-wave velocity model. These images provide information on the geological subsurface structures present in this area. To simultaneously utilize the up- and down-going energy recorded by the nodes, I perform the acoustic Green's function computation using a free-surface condition at the water surface during the imaging procedure (Robertsson, 1996). This choice avoids the necessity of performing an up-down separation step (Schalkwijk et al., 1999). Moreover, I apply a source-side illumination compensation to diminish any acquisition artifacts within the subsurface image volume (Kaelin and Guitton, 2006).

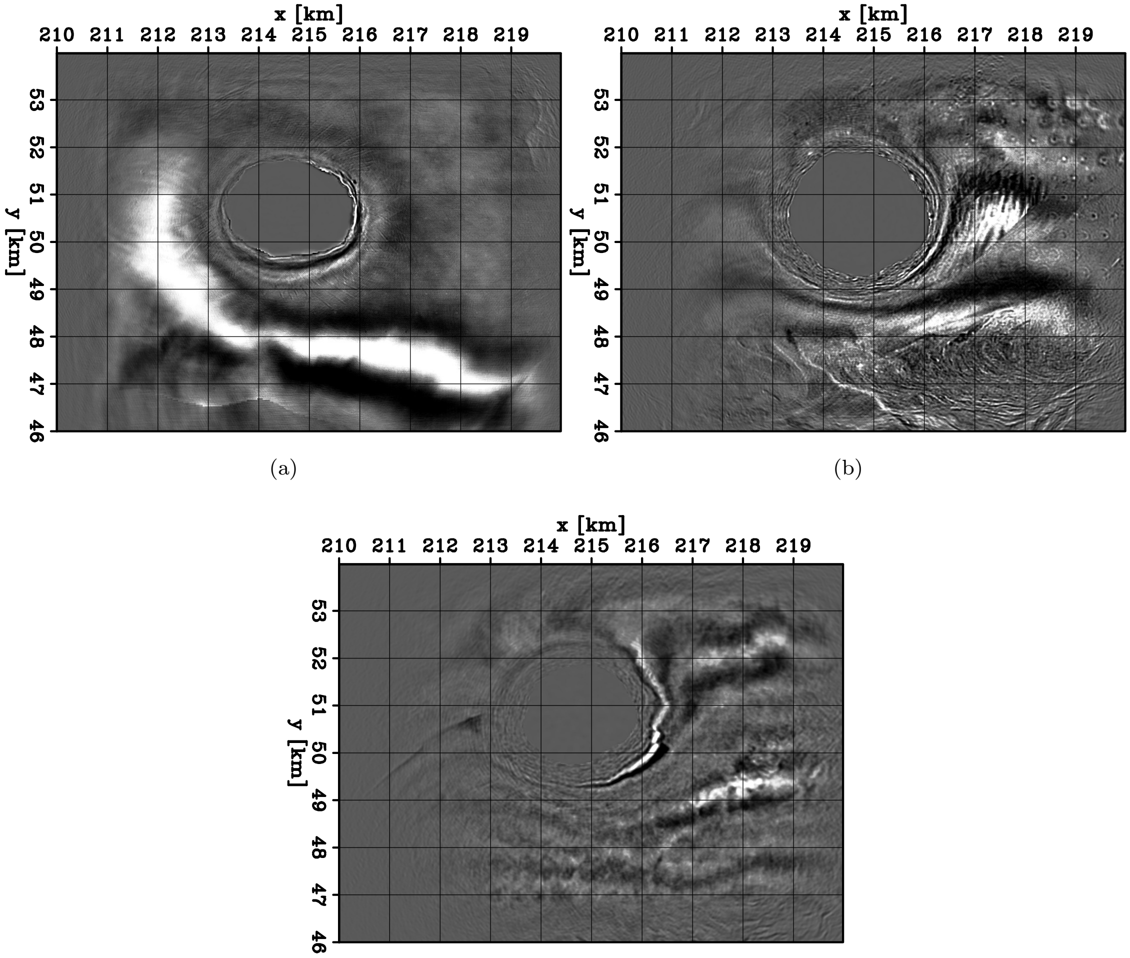

(a) (b)

(c)

Figure 4.7: Depth slices from the 30Hz RTM obtained using the initial provided velocity model. The slices are extracted at: $z = 0.9$ km (a), $z = 1.69$ km (b), and $z = 2.865$ km (c). [**CR**]

Figure 4.7 shows depth slices extracted from the RTM image obtained using the initial velocity model. From the depth section extracted at $z = 0.9$ km (Figure 4.7a), the top edges of the diapir are recognizable as well as radially distributed features around it. These structures are commonly observed in areas where diapirism is present and are due to the presence of radially distributed faults caused by the rising of the salt diapir (Stewart, 2006; Coleman et al., 2018). Furthermore, within deeper sections, multiple structures associated with turbidite sequences can be observed (Berg, 1982). The panel of Figure 4.7b shows an example of such structures on the bottom-right corner of the depth slice. Mild acquisition-footprint artifacts are present despite the application of source-side compensation during the migration process. Finally, in even deeper portions of the image volume, high-amplitude features are visible close to the diapir flanks. For instance, in the depth section extracted at $z = 2.865$ km a noticeable faulted structure is present. Such image features are potentially associated with hydrocarbon prospects (Harding and Lowell, 1979; Tiapkina et al., 2008).

4.4 Acoustic FWI

As shown in the previous chapter, the redatuming process previously described relies on the knowledge of an accurate overburden velocity model. Thus, to improve the initial velocity model, I apply an acoustic isotropic constant-density FWI process to the field pressure data. To mitigate the inaccuracy of the modeling operator of correctly predicting the observed event amplitudes, I employ the objective function proposed by Shen (2010), where a trace-by-trace normalization is applied to both modeled and observed data vectors before computing their difference. It can be easily shown that the minimization of such objective function corresponds to the maximization of the zero-lag cross-correlation between the predicted and observed data. Furthermore, I invert the data using a data-space multiscale approach (Bunks et al., 1995), where progressively wider frequency bands undergo the inversion procedure. The chosen frequency bands are the following: $3-6$, $3-9$, $3-12$, and $3-18$ Hz. For the first three bands, the modeling is performed with an FD grid size of 35 m in the three dimensions, while, for the last band, the modeling is performed with a grid size of 25 m. To mitigate the introduction of any inversion artifacts, I parameterize the model on spline grids with x-y sampling of 175, 105, and 50 m for each band, respectively. The spline grid in the z-axis is as fine as the FD sampling. Finally, I employ the acoustic reciprocity theorem so that the 255 nodes act as sources and the 41000 sources as receivers (Aki and Richards, 2002).

Overall, 216 iterations of BFGS are performed to invert the data up to 18 Hz. Figure 4.8 displays the convergence curve of the acoustic FWI problem. The discontinuities in the curve correspond to the changes in the frequency band during the inversion. For the two central bands, a decrease of approximately 70% is achieved by the minimization algorithm.

From the final P-wave velocity I extract the same cross- and in-line sections from the 3D volume as the ones in Figure 4.5 (Figure 4.9). The inverted model by the FWI scheme shows geologically

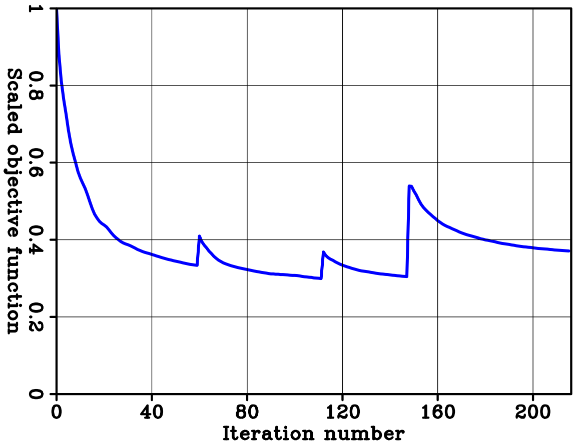

Figure 4.8: Normalized objective function convergence curve. The discontinuities in the curve corresponds to changes in the frequency content of the inverted data. [**CR**]

consistent features. For instance, the panel in Figure 4.9a presents a discontinuity potentially indicating the presence of a fault at $y = 50.2$ km and $z = 3$ km. Moreover, a clear low-velocity anomaly is placed on the salt flank at $z = 2.8$ km (Figure 4.9d). This decrease in velocity could be related to gas accumulation at the top of a hydrocarbon reservoir sealed by the salt body. Finally, the same inclusion reported by Dahlke (2019) is retrieved by the acoustic FWI workflow (Figure 4.9c). In addition, other velocity variations are present at the top of the diapir.

The inversion is affected by artifacts due to the limited acquisition geometry (left sides of Figure 4.9a and 4.9f). Moreover, low-velocity anomalies are placed at depths greater than 3 km. These features are probably due to the convergence to a local minimum of the optimization algorithm. Thus, I limit my area of search for any potential target to 3 km of depth.

In addition to the inclusion shown in Figure 4.9c, the FWI workflow placed a low-velocity anomaly close to the top of the diapir (Figure 4.11). This velocity decrease could be associated with salt-encased sediment packages included during the diapir formation (Fernandez et al., 2017). As a quality control (QC) step, I compare the phase matching between the predicted and the observed pressure data before and after the inversion process is applied. Figure 4.11 shows the phase matching when one of the source-spatial positions is fixed. The phase matching between modeled and observed data for both long- and short-offset traces improves after applying the FWI workflow. When a time slice is extracted from the modeled and the observed data and the phases of the two are compared (Figure 4.12), an excellent match is found using the final FWI acoustic model to generate the pressure data. On the other hand, the accuracy of the matching diminishes for recording time greater than 5 s for the mid- and short-offset ranges.

Besides the satisfactory phase matching between the predicted and observed data, the quality of the RTM image greatly improves thanks to the more accurate velocity retrieved by the FWI process

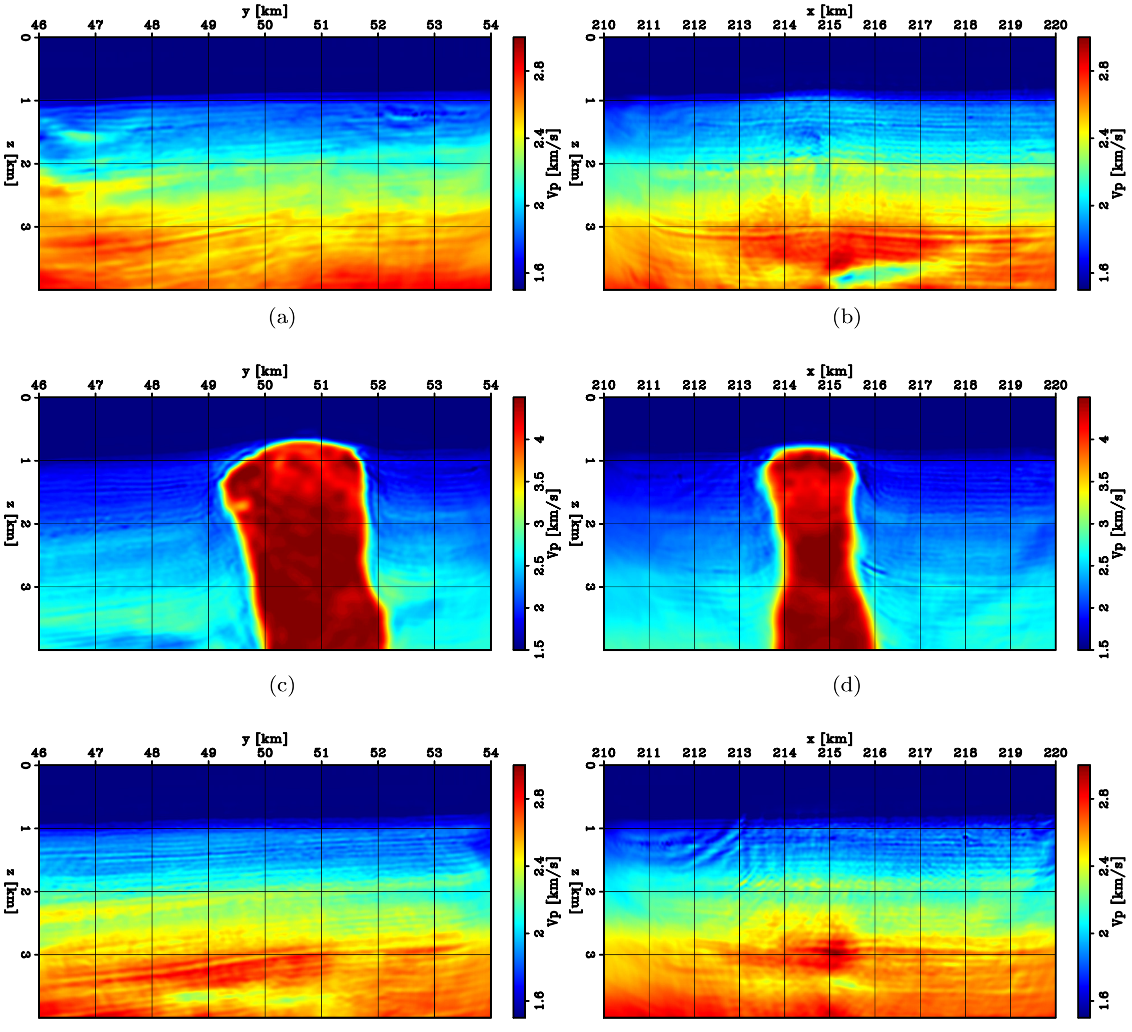

(a) (b)

(c) (d)

(e) (f)

Figure 4.9: Cross- (left column) and in-line (right column) slices extracted from the inverted acoustic FWI velocity model at (a) $x = 212$ km, $y = 49$ km (b), $x = 214.8$ km (c), $y = 51.5$ km (d), $x = 217$ km (e), and $y = 52.5$ km (f). [**CR**]

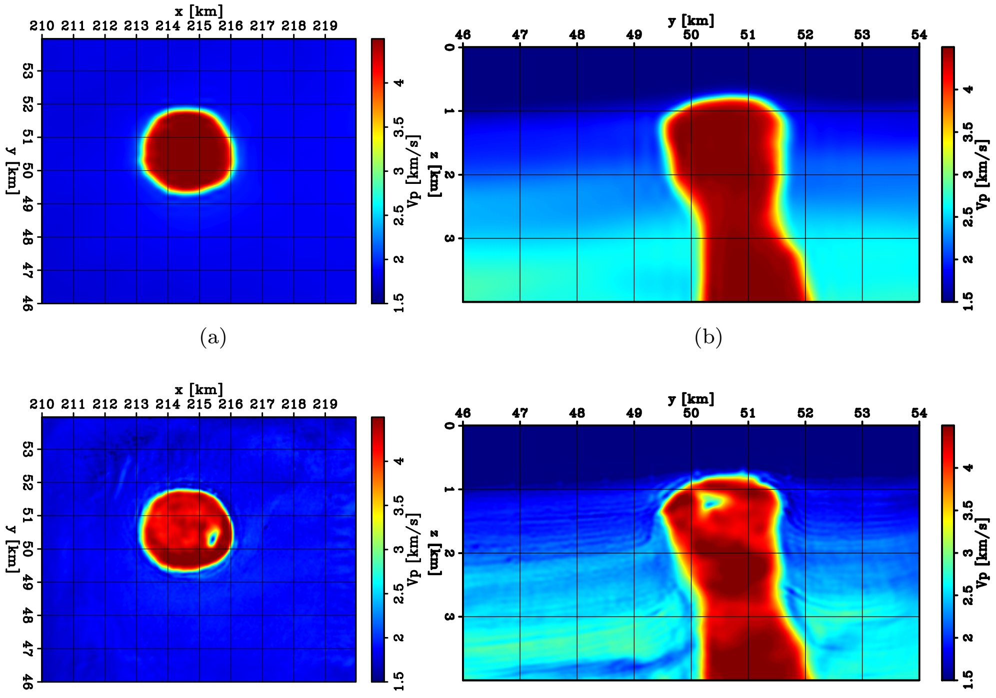

(a) (b)

(c) (d)

Figure 4.10: Comparison between the initial (top panels) and the inverted (bottom panels) acoustic velocity models for (a-c) $z = 1.2$ km and (b-d) $x = 215.5$ km. [**CR**]

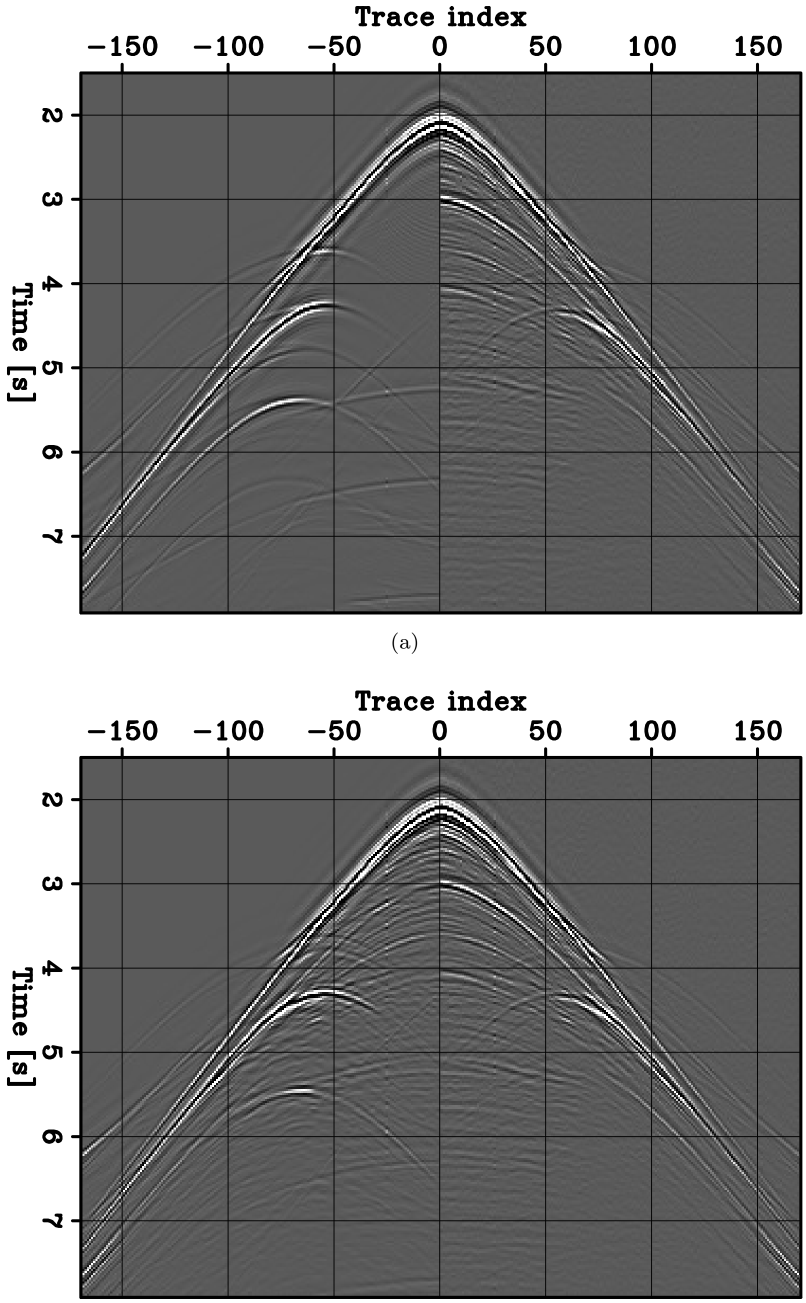

(a)

(b)

Figure 4.11: Comparison between the predicted and observed pressure data on the initial (a) and inverted (b) models, respectively. The negative trace indices indicate the predicted data, while the positive ones denote the observed data. The noisy traces are due to the shot-binning process. Only the traces for $S_x = 49.0$ km are plotted. [**CR**]

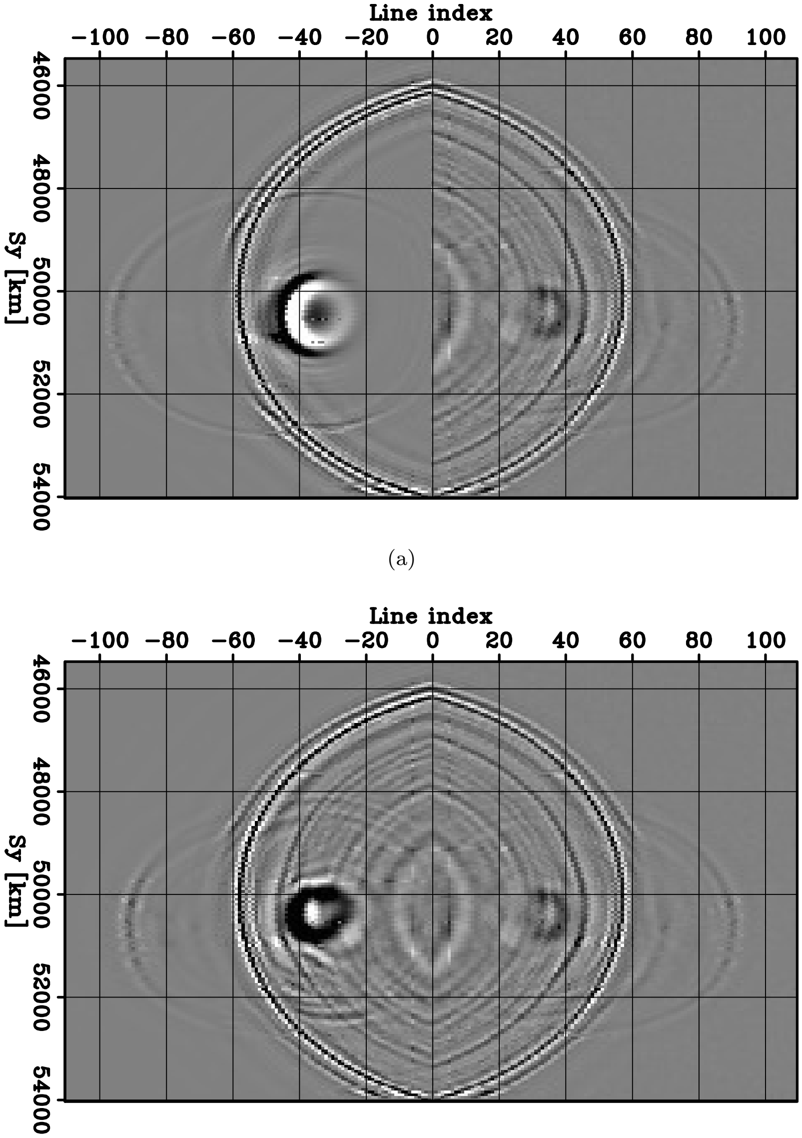

(a)

(b)

Figure 4.12: Comparison between the predicted and observed pressure data on the initial (a) and inverted (b) models, respectively. The negative trace indices indicate the predicted data, while the positive ones denote the observed data. The noisy traces are due to the shot-binning process. The time slices are extracted at $t = 4.0$ s. [**CR**]

(Figure 4.13). In fact, by comparing Figures 4.13a and 4.13c, the fault planes between $y = 49.8$ and $y = 51.5$ km are more visible within the RTM image obtained on the FWI velocity model. For the sections passing through the salt diapir (Figures 4.13b and 4.13d), the overall reflectors' continuity is improved for the RTM image generated on the FWI model; especially, for the reflectors close to the top of the salt body. Moreover, some of the high amplitude reflectors present a more consistent contact point with the salt flanks within the FWI-related RTM image. One interesting geological feature present on the left side in both sections of Figures 4.13b and 4.13d is the sigmoidal shaped reflectors at $z = 2.0$ km. These events are due to the presence of the turbidite deposits previously described.

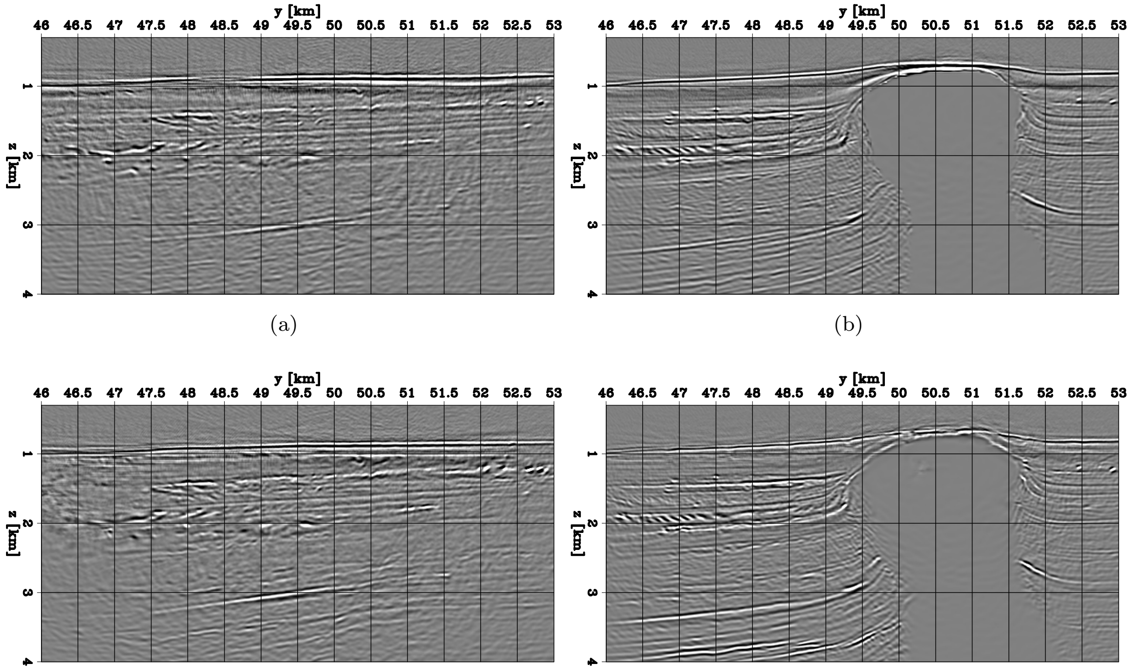

(a) (b) (c) (d)

Figure 4.13: Comparison between the 30 Hz RTM images obtained using the initial (a-b) and the final FWI (c-d) models. The left and right panels are the cross-line sections extracted at $x = 212$ km and 215.5 km, respectively. [**CR**]

4.5 Target-oriented elastic FWI of a potential prospect

By analyzing the RTM image volume obtained using the final FWI velocity model, I identify a clear high-amplitude reflector in the proximity of the salt flank (Figure 4.14). As I described in the previous section, this response could be related to gas accumulation at the top of a hydrocarbon reservoir (Mazzotti, 1990). Therefore, I apply the redatuming technique, followed by an elastic FWI workflow, to retrieve this potential prospect's elastic properties.

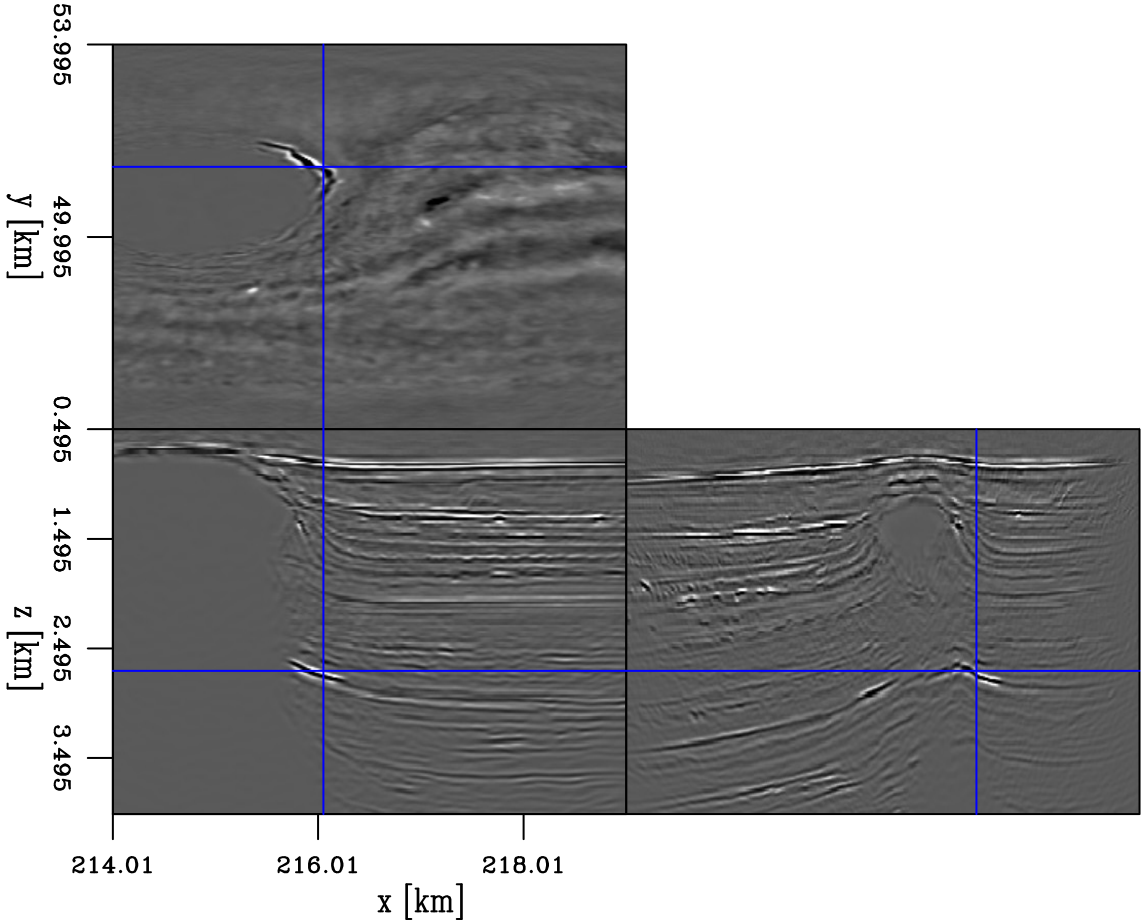

Figure 4.14: 30 Hz RTM images obtained using the final FWI model showing sections passing through the potential target reservoir. [**CR**]

The first step is to solve an extended acoustic linearized inversion of the observed data to obtain an extended 3D image volume. I limit the observed data's maximum frequency to 12 Hz to make the least-squares process feasible with the available computational resources. The FD grid is set to 35 m in each direction. Moreover, given the acquisition's full-azimuth nature, I employ h_x and h_y subsurface-offset extensions of 9 points in each direction, resulting in a maximum absolute subsurface offset of 140 m. Finally, a DSO regularization term is added to improve the image focusing, and its weight is chosen on a heuristic basis. I focus the iterative process on inverting the data component stemming from the target area by employing a mask tailored for the potential prospect. After 30 iterations of a linear CG algorithm, an acceptable numerical minimum of the objective function is reached given the selected parameters (Figure 4.15a). When extracting the zero-subsurface offset image within the target, an evident high-amplitude reflector is visible (Figure 4.15b).

The focusing of the ODCIGs of the target area provides an additional QC step for assessing the migration velocity model's accuracy during the linear inversion process. A representative ODCIG extracted from the target volume is displayed in Figure 4.16a, which presents a clear focus around the zero-subsurface offset axes. Furthermore, by converting this ODCIG into the angle-azimuth domain and I extract the ADCIG for an azimuth of 45° (Figure 4.16b), the angle gather presents a flat response across reflection angles. These two observations suggest that the acoustic FWI process can retrieve an accurate overburden velocity.

I employ this extended image volume to synthesize the elastic pressure data with a new redatumed acquisition geometry placed at $z = 2.1$ km. The sources' and receivers' x-y positions are shown in the panels of Figure 4.17. I employ 150 sources and 8444 receivers, with the latter regularly sampled and spaced by 25 m in each direction. This new acquisition is chosen based on how the original OBN geometry has illuminated the target. I purposely avoid placing acquisition devices on the salt body, given the limited illumination of the target by the original OBN geometry present in that section of the model. Figure 4.18 shows a representative shot gather where an increase in amplitude for the first reflected event is noticeable for receivers at a further distance from the source position. This behavior is a potential indication of an AVO signature from the chosen prospect.

The entire model domain is approximately $10 \times 10 \times 4$ km^3, while the target domain size is approximately $1.5 \times 3 \times 1$ km^3, making the target computational domain approximately 67 times smaller compared to the original one.

The target area's initial P-wave velocity model is obtained by mildly smoothing the acoustically inverted FWI P-wave velocity. The initial density parameter is simply computed using Gardner's equation (Gardner et al., 1974). Finally, the starting guess for the S-wave velocity is obtained using the provided stiffness tensor components. Figure 4.19 shows different panels extracted from the initial elastic parameters of the target area.

I apply an elastic FWI workflow to the redatumed dataset to estimate the target area's elastic parameters. The entire bandwidth of the reconstructed data is simultaneously injected (i.e., $3 - 12$ Hz), and the three elastic parameters are jointly inverted. The total recording time is 4.5 s, which is almost half of the original 8 s data. The elastic FD operator is based on a 20 m grid to abide by the dispersion and stability conditions. However, the inverted model is parameterized using a spline grid of 100 m in the x and y axes, while the z-axis has the same sampling as the FD grid. As in the acoustic FWI step, the spline parameterization effectively acts as regularization and avoids the introduction of spurious features during the inversion.

After minimizing the L2-norm difference between the predicted and the synthesized elastic pressure data with a BFGS optimizer for 10 iterations, I retrieve the elastic parameter cubes shown in Figure 4.20. The inversion procedure introduces most of the changes within the P-wave and density

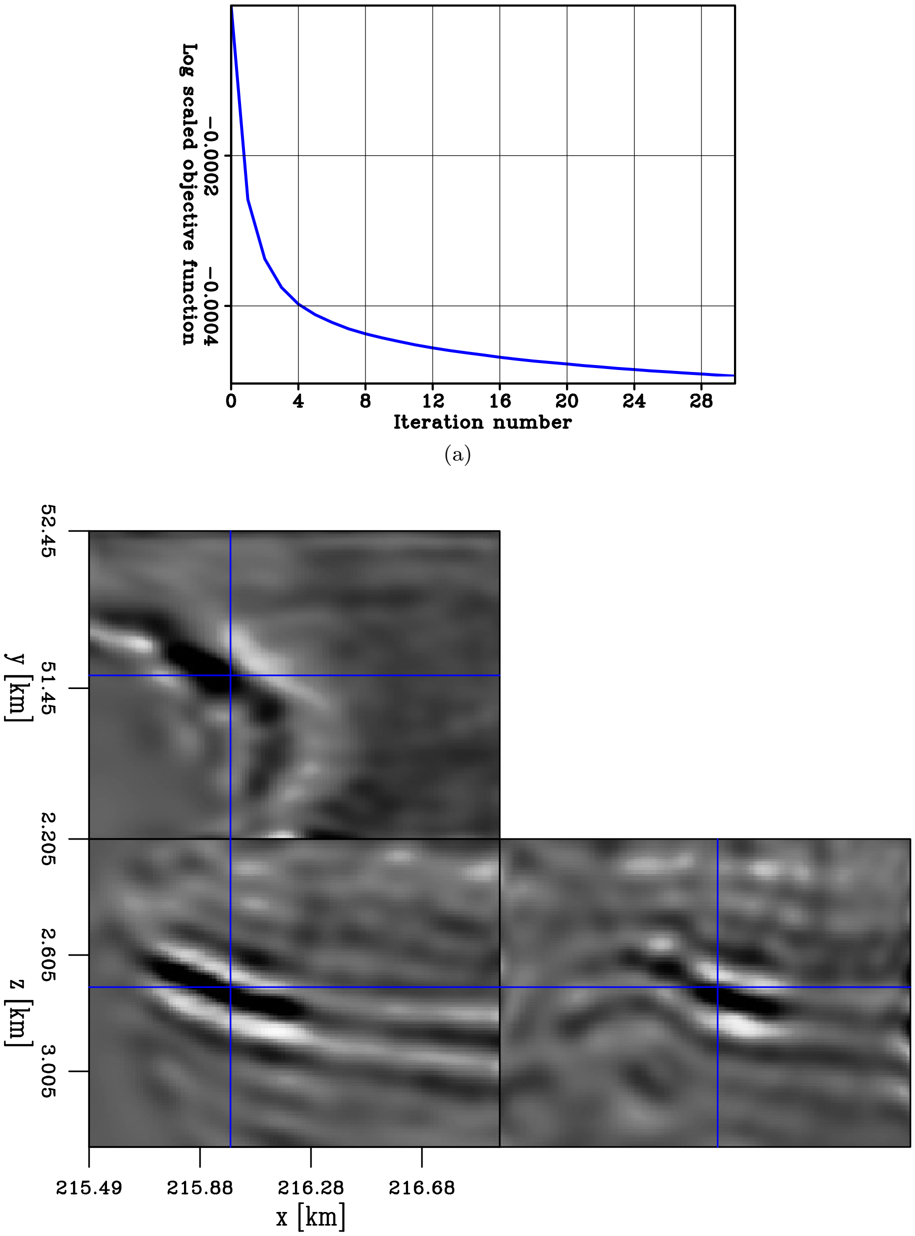

(a)

(b)

Figure 4.15: (a) Convergence curve of the extended linearized waveform inversion problem of the GOM dataset with maximum frequency of 12 Hz. (b) Closeup of the target extracted at $h_x = h_y =$ 0.0 km. [**CR**]

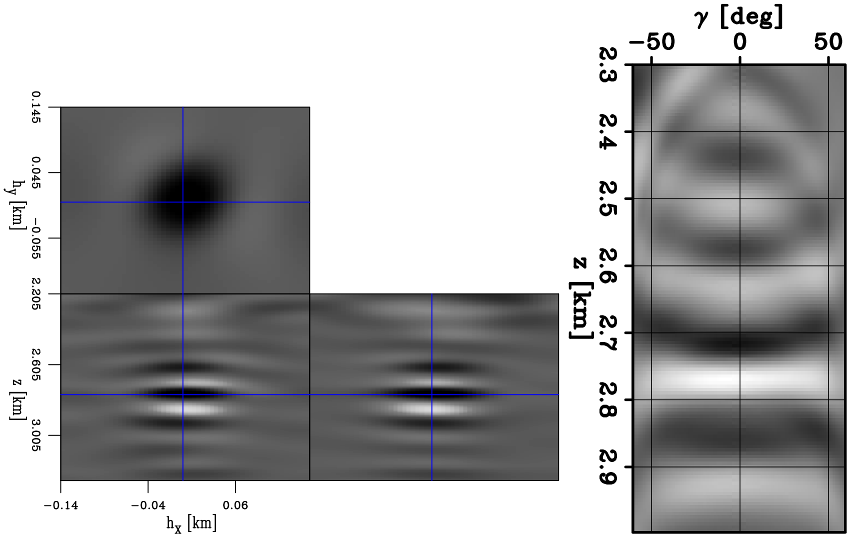

(a) (b)

Figure 4.16: (a) ODCIG of the potential prospect extracted at $x = 216.1$ and $y = 51.5$ km. (b) ADCIG extracted at $x = 216.1$ and $y = 51.5$ km for an azimuth of 45° [**CR**]

parameters. A noticeable decrease in both is observed at the same position as the high-amplitude anomaly observed in the RTM image of Figure 4.14. On the contrary, no significant updates are placed within the S-wave parameter, although similar geometrical features are present within the inverted parameter.

To highlight how the elastic FWI process updates the three parameters, I plot the difference between the inverted and the initial models in Figure 4.21. As expected, an evident decrease at the target's position is observed within the P-wave and density parameters. On the other hand, the S-wave model does not present such a reduction in the same position and displays slightly different structures than the other two parameters. Moreover, the updates in the S-wave parameter is an order of magnitude smaller compared with the P-wave velocity. This behavior provides more confidence with the ability of the process of not introducing cross-talk artifacts.

Using the elastic parameters obtained by the target-oriented inversion, I compute two standard rock physics attributes; namely, the Vp/Vs ratio and the acoustic impedance (AI) (Figure 4.22). The average Vp/Vs ratio and AI of the low-velocity and low-density anomaly are approximately 1.7 and 4.8 $g/cm^3 * km/s$, respectively. These values are consistent with a potential gas-charged sand (Gardner et al., 1968; Ødegaard and Avseth, 2003).

The field application of the proposed target-oriented elastic FWI workflow demonstrates its ability to estimate a potential prospect's elastic properties. In fact, it can retrieve the elastic parameters of a possibly gas-charged reservoir located on the flank of the salt diapir. Moreover, the

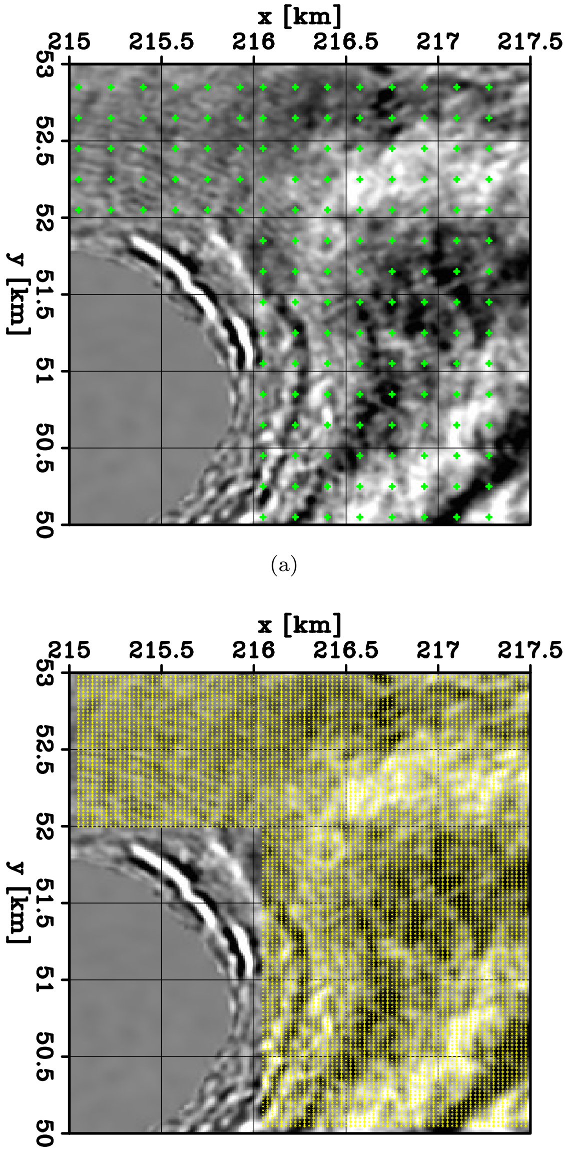

(a)

(b)

Figure 4.17: (a) Sources' and (b) receivers' x-y positions for the target-oriented inversion overlaid on the 30 Hz RTM image depth slice extracted at $z = 2.6$ km. [**CR**]

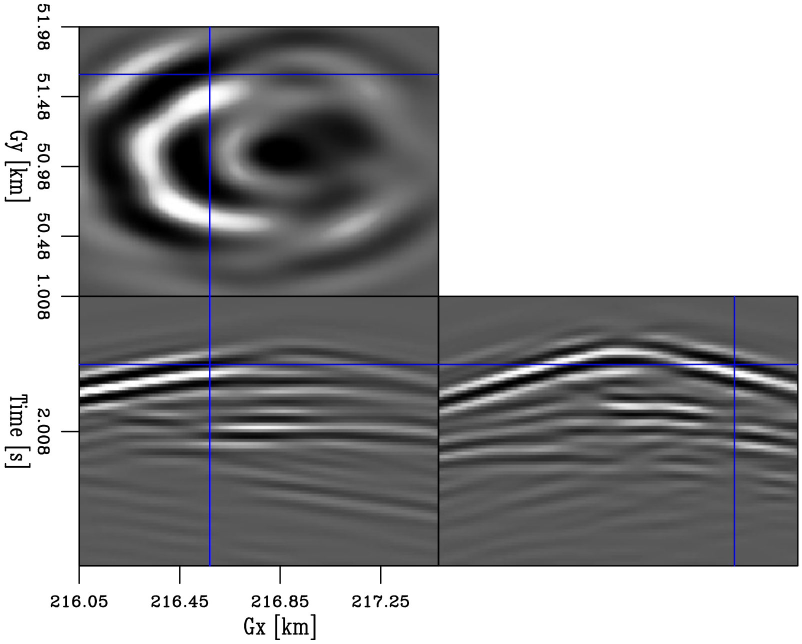

Figure 4.18: Representative shot gather for $Sx = 216.9$ and $Sy = 51.05$ km. Only part of the receivers is plotted. [**CR**]

method's ability to limit the computational domain to only the target area allows the application of a wave-equation estimation method such as FWI. Applying an elastic FWI on the entire 100 km^2 domain is a challenge given the computational cost of solving the elastic wave equation. Using the same resources described within the Marmousi2 test, the elapsed time for performing a single iteration is 133 minutes. I estimate a computational speed-up factor ranging from 500 to 1000 between the original and the target-oriented inversions for this specific example.

4.6 Summary

This chapter showed the application of the proposed target-oriented elastic FWI approach on 3D field data acquired in the GOM by Shell. From the entire OBN datasets, I extracted a subset of the nodes and sources that I believed illuminated subsurface areas of interest. First, I applied filtering techniques to limit the data's frequency content and shaped the observed waveforms to remove the source-bubble reverberations. Then, I compute initial RTM images to understand the geological scenario of the subsurface in this area. To improve the initial P-wave velocity model's accuracy, I employed an acoustic FWI methodology to invert the selected observed pressure data. I assessed the accuracy of this step by comparing the phase-matching between the observed and predicted traces. Furthermore, I highlighted the salt-flank image improvements by comparing RTM sections obtained

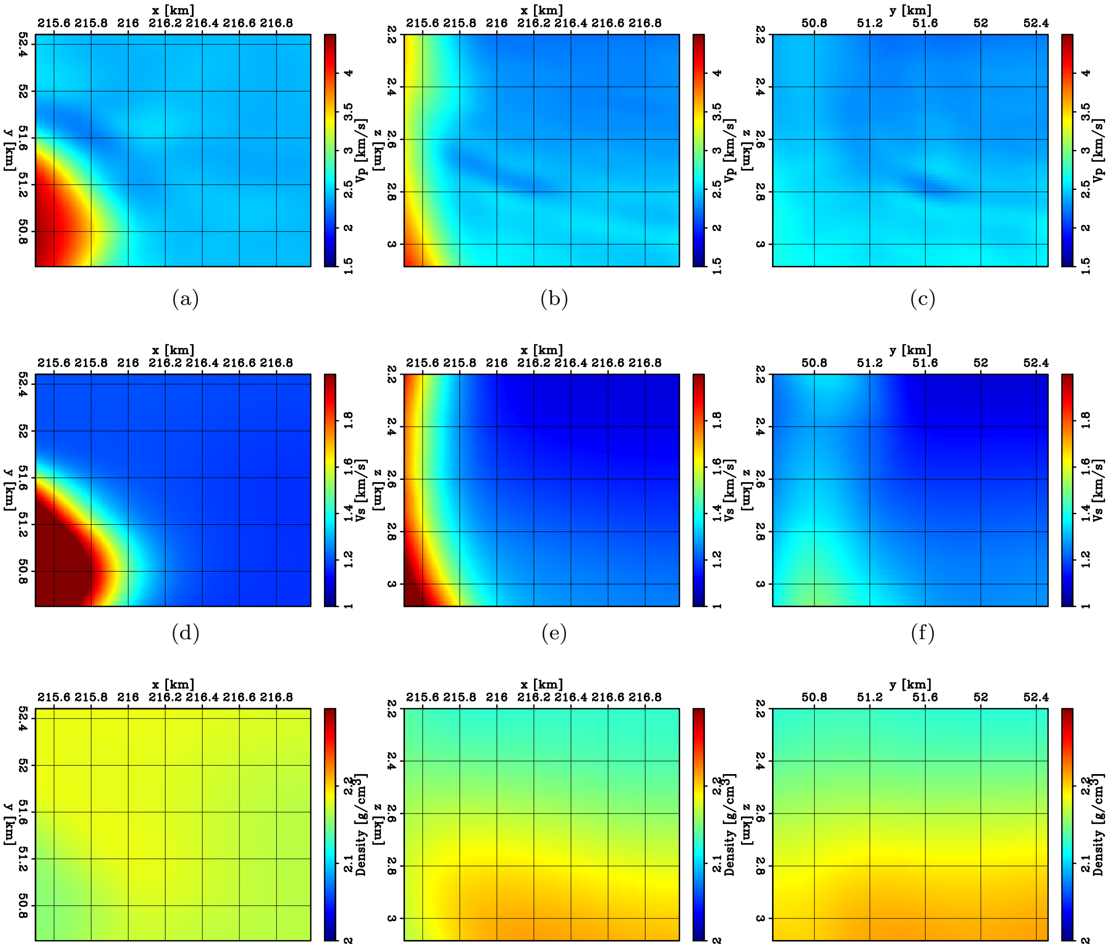

(a) (b) (c)

(d) (e) (f)

(g) (h) (i)

Figure 4.19: Initial elastic parameters of the target area. The top row displays slices extracted from the P-wave velocity cube. The middle row shows panels from the S-wave velocity cube. The bottom row displays slices from the density model cube. On each row, from left to right, the panels are extracted at $z = 2.6$ km, $y = 51.5$ km, $x = 216.1$ km, respectively. [**CR**]

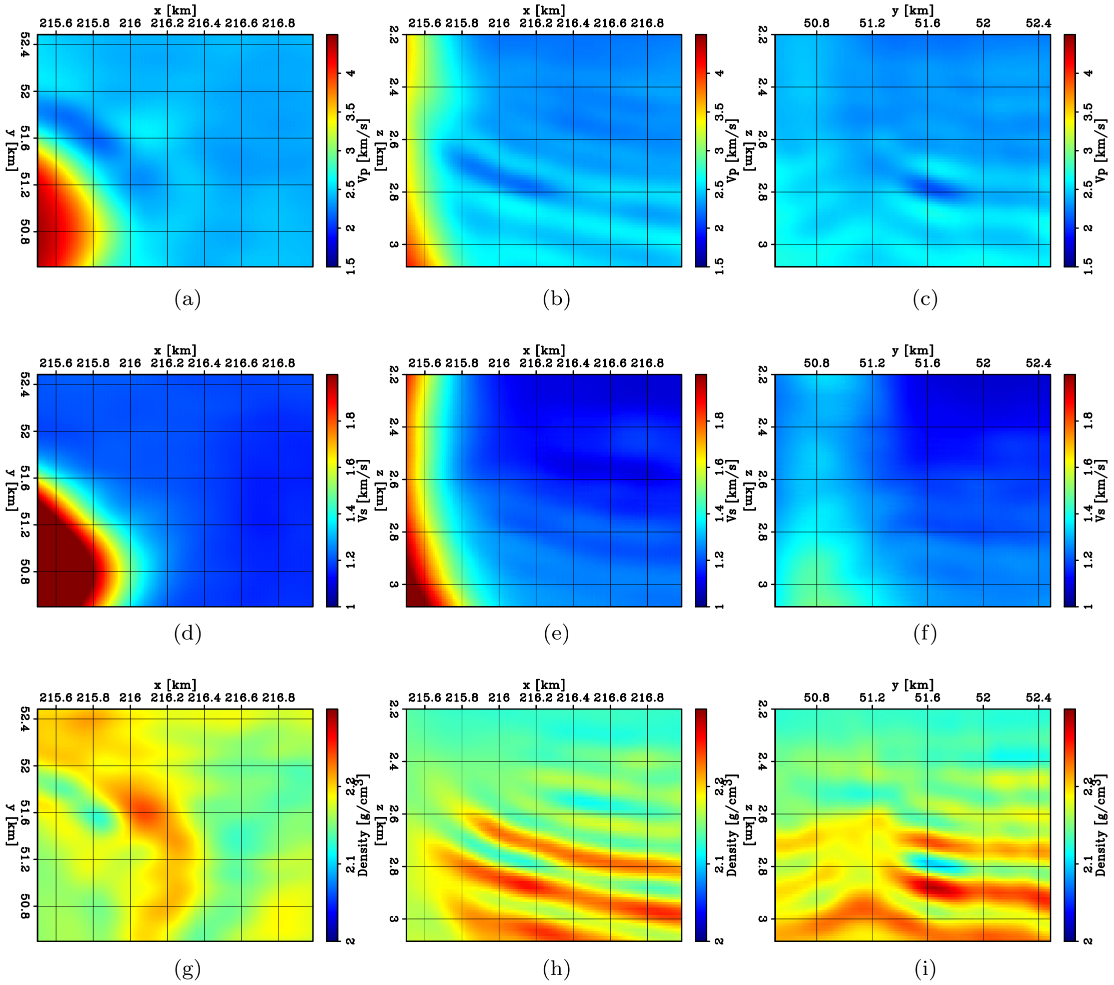

(a) (b) (c)

(d) (e) (f)

(g) (h) (i)

Figure 4.20: Inverted elastic parameters of the target area using the target-oriented elastic FWI workflow. The top row displays slices extracted from the P-wave velocity cube. The middle row shows panels from the S-wave velocity cube. The bottom row displays slices from the density model cube. On each row, from left to right, the panels are extracted at $z = 2.6$ km, $y = 51.5$ km, $x = 216.1$ km, respectively. [**CR**]

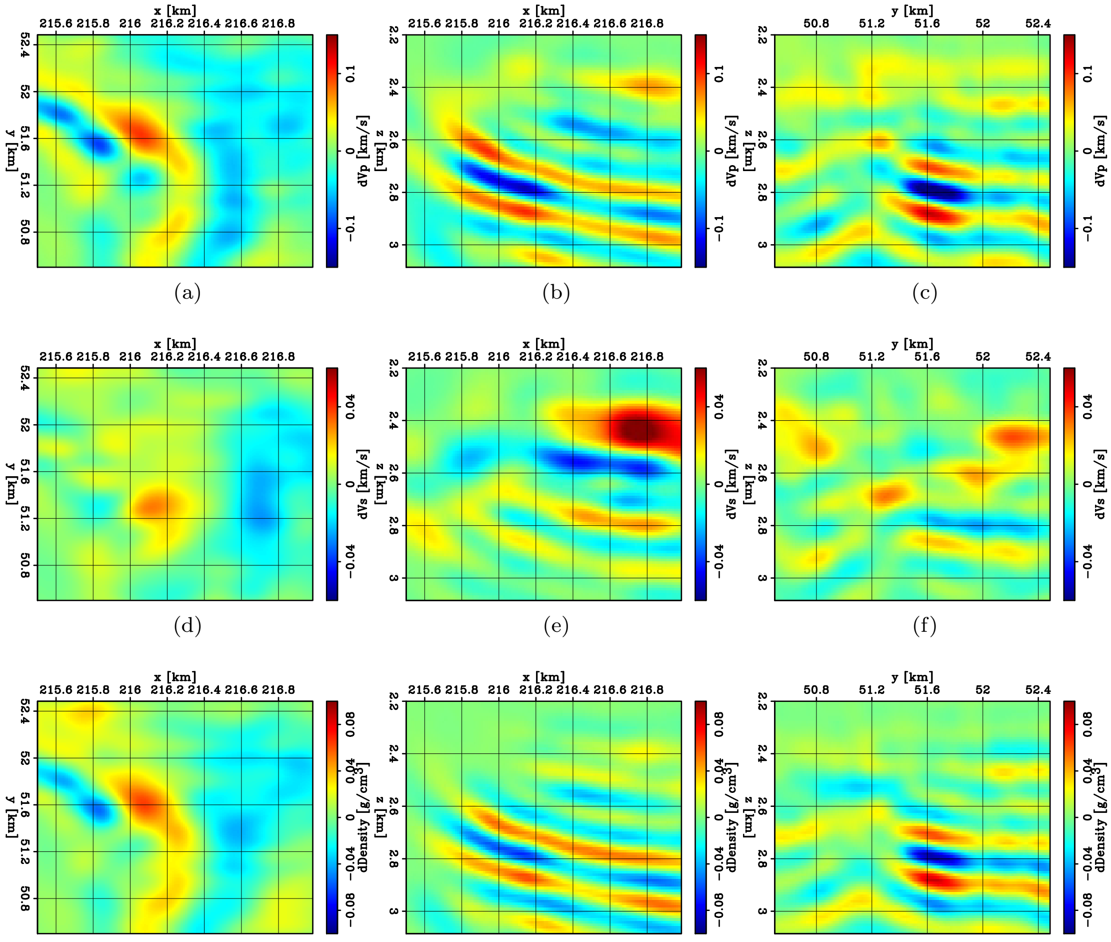

(a) (b) (c)

(d) (e) (f)

(g) (h) (i)

Figure 4.21: Elastic parameter difference between the final and the initial elastic FWI model. The same slices from Figure 4.20 are shown in these panels. [**CR**]

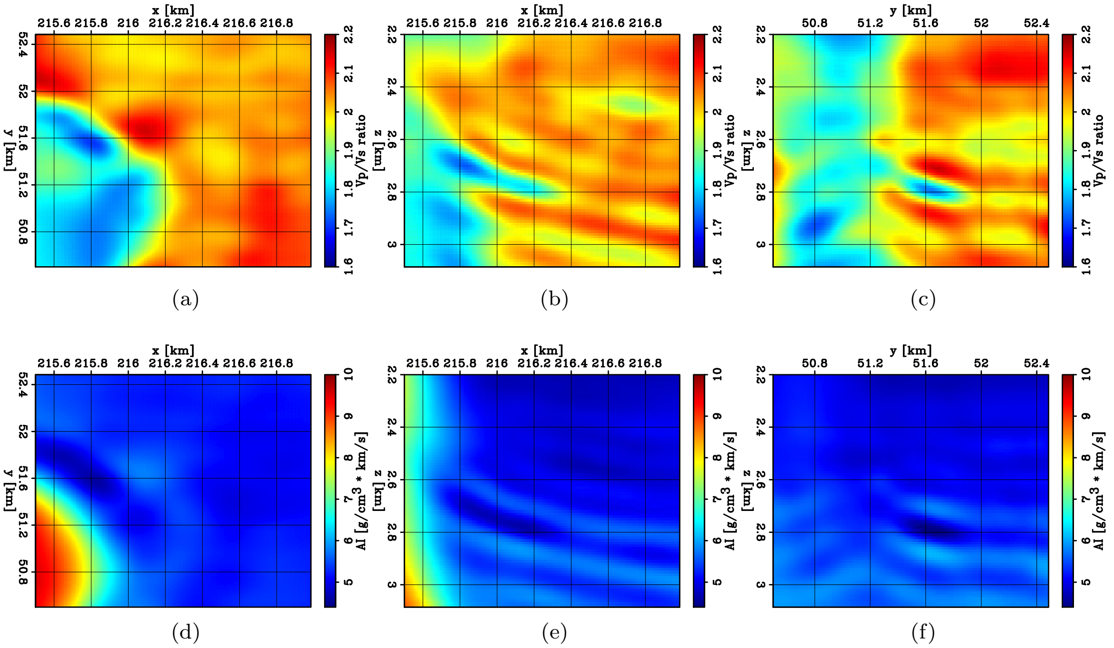

(a) (b) (c)

(d) (e) (f)

Figure 4.22: Rock physics attributes computed using the final. The top and bottom rows display the Vp/Vs ratio and the AI, respectively. The same slices from Figure 4.20 are shown in these panels. [**CR**]

using the initial and the FWI-inverted P-wave models. Finally, using the subsurface RTM images, I identified a potential prospect positioned on the salt diapir's flank. On this target, I applied the proposed elastic waveform methodology to estimate its material proprieties. The rock-physics parameters computed using the estimated properties suggested the existence of a gas-bearing sand reservoir. This field-data application demonstrated the proposed method's potential to retrieve the subsurface elastic parameters using a wave-equation based approach.

Acknowledgement

I would like to acknowledge Shell Exploration and Production Company for permission to show the obtained results and providing the field dataset and the initial elastic model.

Chapter 5

Conclusions

I describe the general framework behind wave-equation operators and their use within the inversion of seismic data. I derive linear and non-linear acoustic and elastic wave-equation modeling operators and employ them to solve linearized and full-waveform inversion problems.

First, I show the ability of an extended linearized waveform inversion to correctly retain the elastic amplitude variations of reflected events even in complex geological scenarios, such as subsalt reservoir horizons. Secondly, based on the solution to an extended linearized waveform inversion problem, I devise a novel redatuming technique in which elastic pressure data can be synthesized as if the acquisition geometry was placed in proximity of a target area. This datumed dataset is then used within an elastic FWI method to estimate a subsurface target area's elastic parameters. This target-oriented elastic FWI workflow limits the computational area to a limited portion of the subsurface, dramatically diminishing the inversion procedure's computational cost. This procedure's computational speed up permits the application of elastic FWI methodologies to seismic exploration 3D field datasets.

I demonstrate the extended image space's efficacy at retaining the elastic amplitude variation on various synthetic examples. On the Marmousi2 synthetic model, I apply the target-oriented elastic FWI procedure to characterize a gas-bearing sand lens's elastic properties. In this 2D application, a computational speed up factor of approximately 200 is achieved compared to the surface elastic pressure's inversion. Finally, I apply the proposed workflow on the pressure component of an OBN dataset recorded in the Gulf of Mexico. I first show the effectiveness of an acoustic FWI workflow to obtain an accurate and data-consistent P-wave velocity model. The updated velocity model can produce more geologically consistent RTM images; especially, close to the salt diapir's sides. Using the produced RTM image, I identify a potential reservoir prospect positioned on the salt flank and apply the target-oriented inversion to estimate its elastic parameters. I speculate the possibility of being associated with gas accumulation within a sand formation from the retrieved properties.

I have applied the proposed target-oriented elastic inversion methodology to only the pressure component of the recorded data. However, the theory for extended migration and inversion can be modified to include multi-component data to exploit all the events recorded by modern OBN acquisitions fully. Additionally, a future study on how to apply the methodology to converted waves might be a viable direction to explore. Finally, one of the obvious future applications of the method is on time-lapse seismic experiments were only known portions of the subsurface are changing as physical processes are occurring. In fact, the method would make computationally affordable the monitoring of the elastic properties of specific subsurface areas. This fact is of great importance given the increasing interest in monitoring carbon capture and sequestration sites.

Appendix A

The adjoint-state method

Introduction

The adjoint-state method is a mathematical technique that allows for efficient computation of derivatives of partial-differential-equation (PDE) constrained optimization problems. This class of inverse problems arises in many different applications where physical systems of PDEs must be solved in order to generate observed data. For instance, in seismology and seismic exploration, usually, a wave equation must be solved in order to obtain simulated recorded traces, or within the field of fluid dynamics, the solution to complex fluid-flow equations must be found to generate modeled data. The caveat associated with finding the derivative of a PDE-constrained objective function is the computational cost of the Jacobian of the governing equation or operator. In fact, the model vector usually contains millions of variables, making the usage of a finite-difference approximation of the gradient unfeasible during a minimization process. The adjoint-state method completely avoids the computation of such Jacobian and thus making the gradient computation efficient. For the continuous case, I follow a similar discussion as Fichtner (2010), but I extend it to the discrete case.

Mathematical background

In this section, I define and review some useful mathematical concepts that can help understand the following derivations. First of all, it is necessary to define the inner product between real functions. Given two functions $f(\mathbf{x})$ and $g(\mathbf{x})$, their inner product can be defined as follows:

$$\langle f, g \rangle = \langle g, f \rangle = \int_{\Omega} f(\mathbf{x}) g(\mathbf{x}) \mathbf{dx}, \tag{A.1}$$

where Ω represents the domain of the functions where the integral of their product is computed. It is also important to define linear operators that transform input functions and can be expressed as follows:

$$h(\mathbf{x}) = Af(\mathbf{x}), \tag{A.2}$$

where A represents a given linear operator that maps $f(\mathbf{x})$ into $h(\mathbf{x})$. Examples of such operators are the Laplacian (∇^2), the gradient (∇), the divergence ($\nabla\cdot$), or the curl ($\nabla\times$). Given these two concepts I can now define the adjoint of a linear operator in the continuous case. For any f and g, a linear operator A and its adjoint A^* are related by the following equality:

$$\langle f, Ag\rangle = \int_\Omega f(\mathbf{x})Ag(\mathbf{x})\mathbf{dx} = \int_\Omega A^* f(\mathbf{x})g(\mathbf{x})\mathbf{dx} = \langle A^* f, g\rangle. \tag{A.3}$$

For example, I derive the adjoint operator of a simple derivative operator in one dimension using this definition. I write the operator D as follows:

$$h(t) = Dg(t) = \frac{dg(t)}{dt} = g'(t). \tag{A.4}$$

To find the adjoint D^*, I use equation A.3 and write the following expression:

$$\langle f, Dg\rangle = \int_0^T f(t)g'(t)dt = [f(t)g(t)]_0^T - \int_0^T f'(t)g(t)dt, \tag{A.5}$$

where I integrated by parts the integral expression. I can see from equation A.5 that the adjoint of the derivative operator is given by a negative derivative operator plus a constant factor, $[f(t)g(t)]_0^T$. In many applications, the constant factor can be neglected by choosing certain boundary conditions (e.g., $f(T) = f(0) = 0$). Therefore, under these conditions, I can write that the adjoint of the derivative operator $D = \frac{d}{dt}$ is given by the following:

$$D^* = -\frac{d}{dt}. \tag{A.6}$$

Theory

I start by first describing the general theory behind the adjoint-state method in the continuous case and then I show how it is translated when I deal with the discrete functions. In both cases, I first define a residual function and show how it is used to form an objective function. Finally, I describe how the gradient of such cost function is computed using the adjoint-state method.

Adjoint-state method: continuous formulation

When dealing with geophysical inverse problems, a residual function is commonly defined as follows:

$$r(m) = d_{pre}(\mathbf{x}; m) - d_{obs}(\mathbf{x}) = \int_\Phi [u(\boldsymbol{\zeta}; m) - u_{obs}(\boldsymbol{\zeta})]\delta(\boldsymbol{\zeta} - \mathbf{x})\mathbf{d}\boldsymbol{\zeta}, \tag{A.7}$$

where d_{pre} and d_{obs} are the predicted and observed data functions, respectively, and m denotes the physical model governing the physics of the predicted data. For example, the model function can represent the wave speed within the subsurface (i.e., $m = v(x, y, z)$). The data function is given by sampling the state or physical variables u and u_{obs}, which could be for instance the pressure or temperature fields. The sampling position of these functions is here represented by $\mathbf{x}$, which could be the time and spatial variables of any recording device. I represent the data extraction using a Dirac delta function δ and integrate the state variables over the physical domain Φ (e.g., (x, y, z, t)). Given the definition of the residual function, I can form an objective function using the inner product described by equation A.1. Using the residual function of equation A.7, I define the well-known L2 inverse problem as follows:

$$\phi(m) = \frac{1}{2}\int_{\Phi}\left\{\int_{\Phi}[u(\boldsymbol{\zeta}; m) - u_{obs}(\boldsymbol{\zeta})]\delta(\boldsymbol{\zeta} - \mathbf{x})\mathbf{d}\boldsymbol{\zeta}\right\}^2 \mathbf{dx} = \frac{1}{2}\langle r(m), r(m)\rangle_{\Phi}. \tag{A.8}$$

The objective function in this equation is a functional that maps a function to a real number (i.e., $\phi \in \mathbb{R}$). The variation of the objective function by a small change of the model function dm can be expressed by the following:

$$d\phi(m) = \frac{\partial\phi(m)}{\partial m}dm = \nabla_m\phi(m)dm, \tag{A.9}$$

where $\nabla_m\phi(m)$ represents the functional derivative with respect to the model function. Given the objective function definition of equation A.8, the functional derivative $\nabla_m\phi(m)$ can be written as follows:

$$\nabla_m\phi(m) = \nabla_m\frac{1}{2}\langle r(m), r(m)\rangle = \langle\nabla_m r, r\rangle = \langle\nabla_u r\nabla_m u, r\rangle, \tag{A.10}$$

in which I dropped the dependency of the functions with respect to the model and where I expanded the derivative of the residual function with respect to the predicted state variable u and the model function m. Also, I removed the integration domain Φ from the inner-product sign.

When a gradient-based method is employed to minimize a given cost function, the derivative of this function with respect to the model parameter must be evaluated. The problem is given by the derivative of the predicted state variable u with respect to the model function m (i.e,, $\nabla_m u$). In fact, in many geophysical applications, the predicted data are given by sampling the solution to a system of PDEs, which is usually numerically computed, and whose derivative might not have an explicit form. For certain simple inverse problems, I can compute $\nabla_m\phi$ using a finite-difference approach. However, it is generally unfeasible to perform such a computation given the number of parameters present within most geophysical inverse problems. This observation will be more evident in the discrete formulation of the adjoint-state method. The goal of the adjoint-state method is to avoid the computation of $\nabla_m u$ altogether.

The adjoint-state method is based on the fact that I can always express the dependency of the state variable u using the following equation:

$$H(u(m), m) = 0. \tag{A.11}$$

For instance, the acoustic isotropic wave equation can be written as follows:

$$H(u(m), m) = \left[\frac{1}{m^2(x,y,z)}\frac{\partial^2}{\partial t^2} - \nabla^2\right] u(x,y,z,t) - f(x,y,z,t) = 0, \tag{A.12}$$

where m is the wave speed within the medium, u is the pressure field, and f is a forcing term. The total differential of equation A.11 is given by the following expression:

$$\frac{dH}{dm} = \nabla_u H \nabla_m u + \nabla_m H = 0, \tag{A.13}$$

where I notice that the derivative $\nabla_m u$ appears. To give an example of this expression, I write the total differential of equation A.12:

$$\frac{dH}{dm} = \left[\frac{1}{m^2}\frac{\partial^2}{\partial t^2} - \nabla^2\right] \nabla_m u - 2\frac{1}{m^3}\frac{\partial^2 u}{\partial t^2}. \tag{A.14}$$

I now multiply equation A.13 by an arbitrary function $u^\dagger$ and integrate over Φ and write the following:

$$\langle u^\dagger, \nabla_u H \nabla_m u + \nabla_m H\rangle = \langle u^\dagger, \nabla_u H \nabla_m u\rangle + \langle u^\dagger, \nabla_m H\rangle = 0. \tag{A.15}$$

Now I add equations A.10 and A.15, without changing the former since I am adding a null function, and write:

$$\nabla_m \phi(m) = \langle \nabla_u r \nabla_m u, r\rangle + \langle u^\dagger, \nabla_u H \nabla_m u\rangle + \langle u^\dagger, \nabla_m H\rangle. \tag{A.16}$$

I focus on the first two terms on the right-hand side of equation A.16 and use the definition of adjoint operators (equation A.3). I can write these terms as follows:

$$\begin{aligned} \langle \nabla_u r \nabla_m u, r\rangle + \langle u^\dagger, \nabla_u H \nabla_m u\rangle &= \langle \nabla_u r^* r, \nabla_m u\rangle + \langle \nabla_u H^* u^\dagger, \nabla_m u\rangle \\ &= \langle \nabla_u r^* r + \nabla_u H^* u^\dagger, \nabla_m u\rangle. \end{aligned} \tag{A.17}$$

If I set $u^\dagger$ such that:

$$\nabla_u r^* r + \nabla_u H^* u^\dagger = 0, \tag{A.18}$$

I can write:

$$\langle \nabla_u r \nabla_m u, r\rangle_{+} \langle u^{\dagger}, \nabla_u H \nabla_m u\rangle = 0, \tag{A.19}$$

which allows us to remove the term $\nabla_m u$ from equation A.16. Therefore, the gradient $\nabla_m \phi$ (equation A.10), can be written as follows:

$$\nabla_m \phi(m) = \langle u^{\dagger}, \nabla_m H\rangle. \tag{A.20}$$

The term $u^{\dagger}$ is commonly referred to as the adjoint-state variable and equation A.18 as the adjoint-state equation.

Let me apply the adjoint-state method to the L2-norm objective function defined in equation A.8 and where the state variable u follows the physics described in equation A.12. To compute the gradient of this cost function, I simply need to determine the terms present in equations A.20 and A.18. Effectively, I need to know $u^{\dagger}$ and $\nabla_m H$. From equation A.13, I observe that:

$$\nabla_m H = -2\frac{1}{m^3}\frac{\partial^2 u}{\partial t^2}. \tag{A.21}$$

and:

$$\nabla_u H = \left[\frac{1}{m^2}\frac{\partial^2}{\partial t^2} - \nabla^2\right]. \tag{A.22}$$

Finally, the operator $\nabla_u r$ is given by:

$$\nabla_u r \cdot = \int_{\Phi} \cdot\, \delta(\boldsymbol{\zeta} - \mathbf{x})\mathbf{d}\boldsymbol{\zeta}, \tag{A.23}$$

which can be easily shown to be self-adjoint (i.e., $\nabla_u r = \nabla_u r^*$). Hence, the term $\nabla_u r^* r$ is simply the residual function of equation A.7. To find the adjoint-state variable $u^{\dagger}$, I need to solve the adjoint-state equation. To do so, I have to know the adjoint operator $\nabla_u H^*$. I obtain this operator by applying the same definition of equation A.3 and write:

$$\begin{aligned}\langle u_2, \nabla_u H u_1\rangle_{\Phi} &= \int_0^T \int_{z_0}^{z_1} \int_{y_0}^{y_1} \int_{x_0}^{x_1} u_2 \left[\frac{1}{m^2}\frac{\partial^2}{\partial t^2} - \nabla^2\right] u_1 dx\, dy\, dz\, dt \\ &= \int_0^T \int_{z_0}^{z_1} \int_{y_0}^{y_1} \int_{x_0}^{x_1} u_2 \frac{1}{m^2}\frac{\partial^2 u_1}{\partial t^2} - u_2 \nabla^2 u_1 dx\, dy\, dz\, dt.\end{aligned} \tag{A.24}$$

The first term within the integral can be written as:

$$\begin{aligned}\int_0^T \frac{u_2}{m^2}\frac{\partial^2 u_1}{\partial t^2}dt &= \frac{1}{m^2}\left\{\left[u_2\frac{\partial u_1}{\partial t}\right]_0^T - \int_0^T \frac{\partial u_2}{\partial t}\frac{\partial u_1}{\partial t}dt\right\} \\ &= \frac{1}{m^2}\left\{\left[u_2\frac{\partial u_1}{\partial t}\right]_0^T - \left[\frac{\partial u_2}{\partial t}u_1\right]_0^T + \int_0^T \frac{\partial^2 u_2}{\partial t^2}u_1 dt\right\},\end{aligned} \tag{A.25}$$

where I integrated by parts twice. The two boundary terms are both zero at $t = 0$ since $u_1(0) = u_1'(0) = 0$. On the other hand, for $t = T$, I have to set different boundary conditions to obtain the same result. The common strategy is to impose the following conditions $u_2(T) = u_2'(T) = 0$. By doing so, I can write:

$$\int_0^T \frac{u_2}{m^2}\frac{\partial^2 u_1}{\partial t^2}dt = \int_0^T \frac{u_1}{m^2}\frac{\partial^2 u_2}{\partial t^2}dt. \tag{A.26}$$

By following a similar procedure and imposing homogeneous spatial boundary conditions, I can show that:

$$\int_{z_0}^{z_1}\int_{y_0}^{y_1}\int_{x_0}^{x_1} u_2\nabla^2 u_1 dx\,dy\,dz = \int_{z_0}^{z_1}\int_{y_0}^{y_1}\int_{x_0}^{x_1} u_1\nabla^2 u_2 dx\,dy\,dz. \tag{A.27}$$

Therefore, I can rewrite equation A.24 as follows:

$$\begin{aligned}\langle u_2, \nabla_u H u_1\rangle_\Phi &= \int_0^T\int_{z_0}^{z_1}\int_{y_0}^{y_1}\int_{x_0}^{x_1} u_2\left[\frac{1}{m^2}\frac{\partial^2}{\partial t^2} - \nabla^2\right]u_1 dx\,dy\,dz\,dt \\ = \int_0^T\int_{z_0}^{z_1}\int_{y_0}^{y_1}\int_{x_0}^{x_1} & u_1\left[\frac{1}{m^2}\frac{\partial^2}{\partial t^2} - \nabla^2\right]u_2 dx\,dy\,dz\,dt = \langle \nabla_u H^* u_2, u_1\rangle_\Phi,\end{aligned} \tag{A.28}$$

which show that, for the acoustic isotropic wave equation, $\nabla_u H^*$ is the same PDE as the governing equation but with different time boundary conditions. Now that I know how to write $\nabla_u H^*$, I can define the adjoint-state equation (equation A.18) for the acoustic isotropic wave equation as follows:

$$\begin{gathered}\left[\frac{1}{m^2(x,y,z)}\frac{\partial^2}{\partial t^2} - \nabla^2\right]u^\dagger(x,y,z,t) = -r(x,y,z,t) \\ \text{subject to } u^\dagger(x,y,z,T) = \frac{u^\dagger}{\partial t}(x,y,z,T) = 0,\end{gathered} \tag{A.29}$$

where I see that $u^\dagger$ is given by the solution of the acoustic isotropic wave equation in which the residual function r is used as the forcing term. Using equation A.20, I can finally write the derivative of the objective function as follows:

$$\nabla_m\phi(m) = -\frac{2}{m^3}\int_0^T u^\dagger\frac{\partial^2 u}{\partial t^2}dt, \tag{A.30}$$

which shows that the gradient is given by the zero-lag correlation between the $u^\dagger$ and the second-order time derivative of state variable u scaled by a function of velocity model m.

Adjoint-state method: discrete formulation

In the discrete formulation, I write the residual vector $\mathbf{r}$ as follows:

$$\mathbf{r}(\mathbf{m}) = K\mathbf{u} - \mathbf{d}_{obs}, \tag{A.31}$$

where $\mathbf{m} \in \mathbb{R}^m$ represents the model-vector parameters, $\mathbf{u} \in \mathbb{R}^p$ is the discrete state variables (e.g., discrete temperature or displacement fields), $\mathbf{d}_{obs} \in \mathbb{R}^n$ is the observed data vector, and $K \in \mathbb{R}^{n\times p}$ represents a sampling matrix extracting the value of state variable at the recording position where the data where observed. In the discrete case, I define the L2-norm objective function as follows:

$$\phi(\mathbf{m}) = \frac{1}{2}\|\mathbf{r}(\mathbf{m})\|_2^2 = \frac{1}{2}\mathbf{r}(\mathbf{m})^*\mathbf{r}(\mathbf{m}), \tag{A.32}$$

where $\phi(\mathbf{m}) \in \mathbb{R}$ and * denotes the adjoint operation. As I discussed in the continuous case, I are interested in minimizing the cost function of equation A.32 by employing a gradient-based optimization algorithm. Therefore, I need to know the gradient of the objective function that is:

$$\nabla\phi(\mathbf{m}) = \left(\frac{\partial\mathbf{r}}{\partial\mathbf{m}}\right)^* \mathbf{r}(\mathbf{m}), \tag{A.33}$$

where $\nabla\phi(\mathbf{m}) \in \mathbb{R}^m$, and $\frac{\partial\mathbf{r}}{\partial\mathbf{m}}$ represents the Jacobian matrix of the residual vector with respect to the model parameters, which belongs to $\mathbb{R}^{n\times m}$. The Jacobian matrix can be written as follows:

$$\frac{\partial\mathbf{r}}{\partial\mathbf{m}} = K\frac{\partial\mathbf{u}}{\partial\mathbf{m}}, \tag{A.34}$$

where $\frac{\partial\mathbf{u}}{\partial\mathbf{m}} \in \mathbb{R}^{p\times m}$ and is the Jacobian matrix of the state variable with respect to the model vector. The goal of the adjoint-state method is to avoid the computation of this matrix, which can be nearly impossible when large systems of PDEs are solved to perform the computation of $\mathbf{u}$. For instance, m can be in the order of millions and p in the order of billions, making the storage of Jacobian matrix impossible even within modern computers or clusters. Additionally, when complex physics is employed to model the data, analytical expressions of this matrix might not be available or unfeasible to compute.

To remove $\frac{\partial\mathbf{u}}{\partial\mathbf{m}}$ from equation A.33, I employ the same steps I used in the continuous case. Again, I assume that $\mathbf{u}$ represents the solution of a PDE. As in equation A.11, I can write the following expression:

$$\mathbf{H}(\mathbf{u}(\mathbf{m}), \mathbf{m}) = \mathbf{0}, \tag{A.35}$$

where $\mathbf{H} \in \mathbb{R}^p$. For example, the acoustic isotropic wave equation, when a finite-difference approached is followed, can be written as follows:

$$\left[MD_t^2 - \nabla^2\right]\mathbf{u} - \mathbf{f} = \mathbf{0}, \tag{A.36}$$

where D_t^2 represents the second-order time derivative operator, ∇^2 is a discrete Laplacian matrix, and $\mathbf{f}$ is the forcing term. M is a diagonal matrix containing the inverse of the squares of the velocity model vector $\mathbf{m}$. By taking the derivative of $\mathbf{H}$ with respect to $\mathbf{m}$ I write the following:

$$\frac{\partial \mathbf{H}}{\partial \mathbf{u}}\frac{\partial \mathbf{u}}{\partial \mathbf{m}} + \frac{\partial \mathbf{H}}{\partial \mathbf{m}} = \mathbf{0}, \tag{A.37}$$

where $\frac{\partial \mathbf{H}}{\partial \mathbf{m}} \in \mathbb{R}^{p\times m}$ and $\frac{\partial \mathbf{H}}{\partial \mathbf{u}} \in \mathbb{R}^{p\times p}$. I now multiply equation A.37 by $\mathbf{u}^\dagger$ and write:

$$\left(\frac{\partial \mathbf{u}}{\partial \mathbf{m}}\right)^*\left(\frac{\partial \mathbf{H}}{\partial \mathbf{u}}\right)^*\mathbf{u}^\dagger + \left(\frac{\partial \mathbf{H}}{\partial \mathbf{m}}\right)^*\mathbf{u}^\dagger = \mathbf{0}, \tag{A.38}$$

where $\mathbf{u}^\dagger \in \mathbb{R}^p$. Following the same naming convention as before, I refer to $\mathbf{u}^\dagger$ as the adjoint-state variable or vector. If I add equations A.38 and A.33, I can write:

$$\begin{aligned}\nabla\phi(\mathbf{m}) &= \left(\frac{\partial \mathbf{u}}{\partial \mathbf{m}}\right)^* K^*\mathbf{r} + \left(\frac{\partial \mathbf{u}}{\partial \mathbf{m}}\right)^*\left(\frac{\partial \mathbf{H}}{\partial \mathbf{u}}\right)^*\mathbf{u}^\dagger + \left(\frac{\partial \mathbf{H}}{\partial \mathbf{m}}\right)^*\mathbf{u}^\dagger \\ &= \left(\frac{\partial \mathbf{u}}{\partial \mathbf{m}}\right)^*\left[K^*\mathbf{r} + \left(\frac{\partial \mathbf{H}}{\partial \mathbf{u}}\right)^*\mathbf{u}^\dagger\right] + \left(\frac{\partial \mathbf{H}}{\partial \mathbf{m}}\right)^*\mathbf{u}^\dagger,\end{aligned} \tag{A.39}$$

and if I choose $\mathbf{u}^\dagger$ such that:

$$K^*\mathbf{r} + \left(\frac{\partial \mathbf{H}}{\partial \mathbf{u}}\right)^*\mathbf{u}^\dagger = \mathbf{0}, \tag{A.40}$$

then the gradient of the objective function simplifies to:

$$\nabla\phi(\mathbf{m}) = \left(\frac{\partial \mathbf{H}}{\partial \mathbf{m}}\right)^*\mathbf{u}^\dagger, \tag{A.41}$$

in which the Jacobian $\frac{\partial \mathbf{u}}{\partial \mathbf{m}}$ can be completely neglected during the gradient computation. Ultimately, to determine the gradient of the objective function, it is necessary to compute $\mathbf{u}^\dagger$ and $\frac{\partial \mathbf{H}}{\partial \mathbf{m}}$.

Let me derive the form of equations A.40 and A.41 when the acoustic isotropic wave equation is assumed to predict the observed data (equation A.36). In this case, the term $\frac{\partial \mathbf{H}}{\partial \mathbf{m}}$ is given by:

$$\frac{\partial \mathbf{H}}{\partial \mathbf{m}} = \ddot{U}, \tag{A.42}$$

which represents the discretization of equation A.21, and can be derived by computing the partial derivative of each vector element of equation A.36 with respect to each model parameter. The adjoint-state equation can be written as follows:

$$\left[MD_t^2 - \nabla^2\right]^* \mathbf{u}^\dagger = -K^* \mathbf{r}, \tag{A.43}$$

which closely resembles equation A.29, where the residual vector is injected as the forcing term. The matrix $\left[MD_t^2 - \nabla^2\right]^*$ is solved according to the time- and space-boundary conditions chosen. If D_t^2 is a lower triangular matrix (i.e., same boundary condition described in the continuous case), then $\mathbf{u}^\dagger$ is found by applying backward substitution. The end-time boundary conditions in equation A.29 automatically arises in this case. A different approach is to choose the time- and space-boundary conditions such that the wave-equation matrix is self-adjoint; hence, the same modeling code can be use to compute both $\mathbf{u}$ and $\mathbf{u}^\dagger$. Finally, the gradient of the objective function is given by:

$$\nabla \phi(\mathbf{m}) = \ddot{U}^* \mathbf{u}^\dagger, \tag{A.44}$$

which also closely resembles the continuous case one (equation A.30).

Appendix B

Subsurface-offset to angle transformation

2D and 3D forward and adjoint operators

The transformation from the subsurface-offset domain (OD) into angle domain (AD) for the 2D case can be written as follows:

$$I_\gamma(x,z,\gamma) = \int_{-\infty}^{\infty} I_h(x, z+\tan(\gamma)h, h)dh, \tag{B.1}$$

where x and z represent the spatial dimensions, γ is the angle, and h the subsurface offset. Without loss of generality, I drop the dependency on x of the images I_γ and I_h. If I refer to the transformation of equation B.1 as the adjoint operator a^* (i.e., mapping the OD into the AD), then the goal of this appendix is to find the forward operator a, which maps the AD to the OD, such that:

$$\begin{aligned}\langle a^*(I_h), I_\gamma\rangle_{z,\gamma} = \int_{-\pi/2}^{\pi/2}\int_{-\infty}^{\infty} \left[a^*(I_h)\right]^* I_\gamma(z,\gamma)dzd\gamma = \\ \int_{-\infty}^{\infty}\int_{-\infty}^{\infty} (I_h)^* a(I_\gamma)(z,h)dzdh = \langle I_h, a(I_\gamma)\rangle_{z,h},\end{aligned} \tag{B.2}$$

where * represents the complex conjugate operation. To derive such operator I employ the Plancherel theorem that can be stated as follows:

$$\begin{aligned}\langle a^*(I_h), I_\gamma\rangle_{z,\gamma} = \langle A^*(\hat{I}_h), \hat{I}_\gamma\rangle_{k_z,\gamma} = \\ \langle \hat{I}_h, A(\hat{I}_\gamma)\rangle_{k_z,h} = \langle I_h, a(I_\gamma)\rangle_{z,h},\end{aligned} \tag{B.3}$$

where $\hat{I}_h$ and $\hat{I}_\gamma$ are the Fourier transformed images in the OD and AD along the z dimension, while A and A^* are forward and adjoint operators of the offset to angle transform in the Fourier domain, respectively. Therefore, to find the forward operator a I can derive the corresponding operator A and apply the inverse Fourier transform to go back to the spatial domain z.

First, I derive the operator A^* by substituting the the Fourier transformed I_h (i.e., $I_h(z,h) = \int_{-\infty}^{\infty} \hat{I}_h(k_z,h)e^{i2\pi k_z z}dk_z$) into equation B.1:

$$\int_{-\infty}^{\infty} I_h(z+\tan(\gamma)h,h)dh = \int_{-\infty}^{\infty} e^{i2\pi k_z z} \int_{-\infty}^{\infty} \hat{I}_h(k_z,h)e^{i2\pi k_z \tan(\gamma)h} dhdk_z, \tag{B.4}$$

which shows that:

$$\hat{I}_\gamma(k_z,\gamma) = A^*(\hat{I}_h)(k_z,\gamma) = \int_{-\infty}^{\infty} \hat{I}_h(k_z,h)e^{i2\pi k_z \tan(\gamma)h} dh. \tag{B.5}$$

I find the operator A by applying the definition in equation B.3 and by simple algebraic steps as follows:

$$\begin{aligned}&\int_{-\pi/2}^{\pi/2}\int_{-\infty}^{\infty} \hat{I}_\gamma(k_z,\gamma) \int_{-\infty}^{\infty} \left[\hat{I}_h(k_z,h)e^{i2\pi k_z \tan(\gamma)h}\right]^* dhdk_zd\gamma = \\ &\int_{-\infty}^{\infty}\int_{-\infty}^{\infty} \hat{I}_h^*(k_z,h) \int_{-\pi/2}^{\pi/2} \hat{I}_\gamma(k_z,\gamma)e^{-i2\pi k_z \tan(\gamma)h} d\gamma dk_z dh.\end{aligned} \tag{B.6}$$

Hence, the forward operator A is given by the following:

$$A(\hat{I}_\gamma)(k_z,h) = \int_{-\pi/2}^{\pi/2} \hat{I}_\gamma(k_z,\gamma)e^{-i2\pi k_z \tan(\gamma)h} d\gamma, \tag{B.7}$$

and the adjoint operator as the transform of equation B.5. Finally, by applying the inverse Fourier transform along the z axis on equation B.7, I can write the following expression:

$$\tilde{I}_h(x,z,h) = \int_{-\pi/2}^{\pi/2} I_\gamma(x,z-\tan(\gamma)h,\gamma)d\gamma, \tag{B.8}$$

which shows that the forward operator of equation B.1 is a slant-stack operation performed in the angle domain.

By following the same reasoning, I can write the forward and adjoint 3D OD to AD transformations as follow:

$$\tilde{I}_h(x,y,z,h_x,h_y) = \int_{-\pi/2}^{\pi/2}\int_0^{\pi} I_\gamma(x,y,z-\tan(\gamma)[\cos(\phi)h_x - \sin(\phi)h_y],\gamma,\phi)d\phi d\gamma, \tag{B.9}$$

$$\tilde{I}_\gamma(x,y,z,\gamma,\phi) = \int_{-\infty}^{\infty}\int_{-\infty}^{\infty} I_h(x,y,z+\tan(\gamma)[\cos(\phi)h_x - \sin(\phi)h_y],h_x,h_y)dh_xdh_y. \tag{B.10}$$

In equation B.9, the variable γ represents the reflection angle (i.e., the angle defined by the normal to the reflection plane and the source or receiver local ray), while ϕ is the reflection azimuth (i.e., the angle of the line defined by the intersection with the plane for $z = 0$ and of the plane containing the source and receiver rays) (Biondi and Tisserant, 2004).

2D pseudo-inverse operator

Whenever dealing with a domain transformation (e.g., Fourier transform), it is useful to find its pseudo-inverse operator. Under certain conditions, for the OD to AD transform I can defined the pseudo inverse in the Fourier domain as follows:

$$A^{\dagger} = (A^{*}A)^{-1}A^{*}. \tag{B.11}$$

Hence, the derivation of the pseudo-inverse operator of the subsurface offset to angle transform requires the knowledge of the inverse of $A^{*}A$. For the operators described in the previous section, I can write the following expression:

$$\begin{aligned} A^{*}A(\hat{I}_{\gamma})(k_z,\gamma') &= \int_{-\infty}^{\infty} e^{i2\pi k_z \tan(\gamma')h} \int_{-\pi/2}^{\pi/2} \hat{I}_{\gamma}(k_z,\gamma) e^{-i2\pi k_z \tan(\gamma)h} d\gamma dh \\ &= \int_{-\infty}^{\infty} e^{i2\pi p' h} \int_{-\infty}^{\infty} \frac{\cos^2(f(p))}{k_z} \hat{I}_{\gamma}(k_z, f(p)) e^{-i2\pi ph} dp dh \\ &= \frac{\cos^2(\gamma')}{k_z} \hat{I}_{\gamma}(k_z,\gamma'), \end{aligned} \tag{B.12}$$

where I define $p = k_z \tan(\gamma)$, $dp = d\gamma k_z / \cos^2(\gamma)$, $f(p) = \arctan(p/k_z)$, and employed the Fourier inversion theorem. If I assume that the image $\hat{I}_{\gamma}$ is equal to zero for $\gamma = \{-\pi/2, \pi/2\}$ and $k_z = 0$, I can write the pseudo-inverse operator as follows:

$$A^{\dagger}(\hat{I}_h)(k_z,\gamma) = \frac{k_z}{\cos^2(\gamma)} \int_{-\infty}^{\infty} \hat{I}_h(k_z,h) e^{i2\pi k_z \tan(\gamma)h} dh. \tag{B.13}$$

Finally, it is trivial to show that, in the space domain, the pseudo inverse can be written as follows:

$$a^{\dagger} = F^{*}(A^{*}A)^{-1}A^{*}F \tag{B.14}$$

where F represents the Fourier transform operator along the z axis. The same result can be obtained by using the ray parameter within the transform integrals (Liu and Luo, 2020).

3D pseudo-inverse operator

The derivation of the pseudo-inverse operator for the 3D OD to AD transform can be derived in a similar fashion as the 2D case. If A_{3D} denotes the Fourier-domain 3D AD to OD transform, then equation B.12 can be written as follows:

$$\begin{aligned}
&A^*_{3D}A_{3D}(\hat{I}_\gamma)(k_z,\gamma',\phi') = \\
&= \int_{-\infty}^{\infty}\int_{-\infty}^{\infty} e^{i2\pi k_z \tan(\gamma')[\cos(\phi')h_x-\sin(\phi')h_y]}\left[\int_{-\pi/2}^{\pi/2}\int_{0}^{\pi}\hat{I}_\gamma(k_z,\gamma,\phi)e^{-i2\pi k_z\tan(\gamma)[\cos(\phi)h_x-\sin(\phi)h_y]}d\phi d\gamma\right]dh_xdh_y \\
&= \int_{-\infty}^{\infty}\int_{-\infty}^{\infty} e^{i2\pi p'h_x}e^{-i2\pi q'h_y}\left[\int_{-\infty}^{\infty}\int_{-\infty}^{\infty}\frac{\cos^2(f(p,q))}{k_z^2\tan(f(p,q))}\hat{I}_\gamma(k_z,f(p,q),g(p,q))e^{-i2\pi ph_x}e^{i2\pi qh_y}dpdq\right]dh_xdh_y \\
&= \frac{\cos^2(\gamma')}{k_z^2\tan(\gamma')}\hat{I}_\gamma(k_z,\gamma',\phi'),
\end{aligned} \tag{B.15}$$

where $p = k_z\tan(\gamma)\cos(\phi)$, $q = k_z\tan(\gamma)\sin(\phi)$, $f(p,q) = \arctan(\sqrt{p^2+q^2}/k_z)$, $g(p,q) = \arctan(q/p)$, and $dpdq = k_z^2\tan(\gamma)/\cos^2(\gamma)d\phi d\gamma =$. Therefore, the pseudo-inverse operator can be written as follows:

$$A^\dagger_{3D}(\hat{I}_h)(k_z,\gamma,\phi) = \frac{k_z^2\tan(\gamma)}{\cos^2(\gamma)}\int_{-\infty}^{\infty}\int_{-\infty}^{\infty}\hat{I}_h(k_z,h_x,h_y)e^{i2\pi k_z\tan(\gamma)[\cos(\phi)h_x-\sin(\phi)h_y]}dh_xdh_y. \tag{B.16}$$

Equivalence of DSO regularization to smoothing along angles

In this section, I show how the minimization of a DSO-regularized extended image corresponds to enforcing a smooth constraint along the angle in the AD image. To simplify the discussion, I define the OD to AD transform in term of $p = tan(\gamma)$, an invertible change of variable in the domain of γ, and consider the 2D case. Thus, the equivalence can be expressed as follows:

$$\left\langle \frac{\partial\hat{I}_p(k_z,p)}{\partial p}, \frac{\partial\hat{I}_p(k_z,p)}{\partial p}\right\rangle_{k_z,p} \alpha\ \langle h\hat{I}_h(k_z,h), h\hat{I}_h(k_z,h)\rangle_{k_z,h}, \tag{B.17}$$

where $\hat{I}_p(k_z,p)$ is given by:

$$\hat{I}_p(k_z,p) = A^*(\hat{I}_h)(k_z,p) = \int_{-\infty}^{\infty}\hat{I}_h(k_z,h)e^{i2\pi k_zph}dh. \tag{B.18}$$

The derivative along the variable p is then written as follows:

$$\frac{\partial\hat{I}_p(k_z,p)}{\partial p} = i2\pi k_z\int_{-\infty}^{\infty}h\hat{I}_h(k_z,h)e^{i2\pi k_zph}dh = i2\pi k_zA^*(h\hat{I}_h)(k_z,p). \tag{B.19}$$

Using equation B.19, I write the left-hand side of equation B.17 as:

$$\begin{aligned}\left\langle \frac{\partial \hat{I}_p(k_z,p)}{\partial p}, \frac{\partial \hat{I}_p(k_z,p)}{\partial p} \right\rangle_{k_z,p} &= \left\langle i2\pi k_z A^*(h\hat{I}_h)(k_z,p), i2\pi k_z A^*(h\hat{I}_h)(k_z,p) \right\rangle_{k_z,p} \\ &= \left\langle h\hat{I}_h(k_z,h), (2\pi k_z)^2 AA^*(h\hat{I}_h)(k_z,h) \right\rangle_{k_z,h}.\end{aligned} \tag{B.20}$$

The application of the operator AA^* is obtained as follows:

$$\begin{aligned}AA^*(\hat{I}_h)(k_z,h) &= \int_{-\infty}^{\infty} e^{-i2\pi k_z ph} \int_{-\infty}^{\infty} \hat{I}_h(k_z,h') e^{-i2\pi k_z ph'} dh' dp \\ &= k_z^{-1} \hat{I}_h(k_z,h').\end{aligned} \tag{B.21}$$

Hence, equation B.20 yields:

$$\begin{aligned}\left\langle \frac{\partial \hat{I}_p(k_z,p)}{\partial p}, \frac{\partial \hat{I}_p(k_z,p)}{\partial p} \right\rangle_{k_z,p} &= 4\pi^2 \left\langle h\hat{I}_h(k_z,h), |k_z| h\hat{I}_h(k_z,h) \right\rangle_{k_z,h} \\ &\alpha \left\langle h\hat{I}_h(k_z,h), h\hat{I}_h(k_z,h) \right\rangle_{k_z,h},\end{aligned} \tag{B.22}$$

which shows the proportionality between the two norms and thus their equivalence when minimized. A similar derivation can be followed for the 3D case by defining $p = tan(\gamma)cos(\phi)$ and $q = tan(\gamma)sin(\phi)$. In this case the equivalence is written as follows:

$$\left\langle \frac{\partial^2 \hat{I}_p(k_z,p,q)}{\partial p \partial q}, \frac{\partial^2 \hat{I}_p(k_z,p,q)}{\partial p \partial q} \right\rangle_{k_z,p,q} \alpha \left\langle h_x h_y \hat{I}_h(k_z,h_x,h_y), h_x h_y \hat{I}_h(k_z,h_x,h_y) \right\rangle_{k_z,h_x,h_y}. \tag{B.23}$$

Bibliography

Aki, K., and Richards, P. G., 2002, Quantitative seismology: University Science Books.

Albertin, U., Yingst, D., Kitchenside, P., and Tcheverda, V., 2004, True-amplitude beam migration: SEG Technical Program Expanded Abstracts 2004, 949–952.

Alkhalifah, T., 2014, Scattering-angle based filtering of the waveform inversion gradients: Geophysical Journal International, **200**, no. 1, 363–373.

Alves, G. C., 2017, Elastic full waveform inversion of multicomponent data: Ph.D. thesis, Stanford University.

Anderson, J. E., Tan, L., and Wang, D., 2012, Time-reversal checkpointing methods for rtm and fwi: Geophysics, **77**, no. 4, S93–S103.

Aster, R. C., Borchers, B., and Thurber, C. H., 2018, Parameter estimation and inverse problems: Elsevier.

Averbuch, A., and Shkolnisky, Y., 2003, 3d fourier based discrete radon transform: Applied and Computational Harmonic Analysis, **15**, no. 1, 33–69.

Barnier, G., Biondi, E., and Clapp, R., 2019, Waveform inversion by model reduction using spline interpolation: SEG Technical Program Expanded Abstracts 2019, 1400–1404.

Bartels, R. H., Beatty, J. C., and Barsky, B. A., 1995, An introduction to splines for use in computer graphics and geometric modeling: Morgan Kaufmann.

Baysal, E., Kosloff, D. D., and Sherwood, J. W., 1983, Reverse time migration: Geophysics, **48**, no. 11, 1514–1524.

Berg, O. R., 1982, Seismic detection and evaluation of delta and turbidite sequences: their application to exploration for the subtle trap: AAPG Bulletin, **66**, no. 9, 1271–1288.

Berryhill, J. R., 1979, Wave-equation datuming: Geophysics, **44**, no. 8, 1329–1344.

Biondi, B., and Almomin, A., 2014, Simultaneous inversion of full data bandwidth by tomographic full-waveform inversion: Geophysics, **79**, no. 3, WA129–WA140.

Biondi, B., and Symes, W. W., 2004, Angle-domain common-image gathers for migration velocity analysis by wavefield-continuation imaging: Geophysics, **69**, no. 5, 1283–1298.

Biondi, B., and Tisserant, T., 2004, 3d angle-domain common-image gathers for migration velocity analysis: Geophysical Prospecting, **52**, no. 6, 575–591.

Brossier, R., Operto, S., and Virieux, J., 2009, Two-dimensional seismic imaging of the valhall model from synthetic obc data by frequency-domain elastic full-waveform inversion: SEG Technical Program Expanded Abstracts 2009, 2293–2297.

Buland, A., and Omre, H., 2003, Bayesian linearized avo inversion: Geophysics, **68**, no. 1, 185–198.

Bunks, C., Saleck, F. M., Zaleski, S., and Chavent, G., 1995, Multiscale seismic waveform inversion: Geophysics, **60**, no. 5, 1457–1473.

Castagna, J. P., and Backus, M., 1993, Avo analysis—tutorial and review: Offset-dependent reflectivity—Theory and practice of AVO analysis: SEG Investigations in Geophysics, **8**, 3–36.

Castagna, J. P., and Swan, H. W., 1997, Principles of avo crossplotting: The leading edge, **16**, no. 4, 337–344.

Chadwick, P., 1976, Continuum mechanics: Concise theory and problems(book): New York, Halsted Press, 1976. 174 p.

Chavent, G., Dupuy, M., Lemmonier, P., , et al., 1975, History matching by use of optimal theory: Society of Petroleum Engineers Journal, **15**, no. 01, 74–86.

Coleman, A. J., Jackson, C. A.-L., Duffy, O. B., and Nikolinakou, M. A., 2018, How, where, and when do radial faults grow near salt diapirs?: Geology, **46**, no. 7, 655–658.

Dahlke, T., 2019, Velocity model building using shape optimization applied to level sets: Stanford University.

De Boor, C., B (asic)-spline basics.:, Technical report, WISCONSIN UNIV-MADISON MATHEMATICS RESEARCH CENTER, 1986.

Fernandez, N., Duffy, O. B., Hudec, M. R., Jackson, M. P., Burg, G., Jackson, C. A.-L., and Dooley, T. P., 2017, The origin of salt-encased sediment packages: Observations from the se precaspian basin (kazakhstan): Journal of Structural Geology, **97**, 237–256.

Fichtner, A., Kennett, B. L., Igel, H., and Bunge, H.-P., 2008, Theoretical background for continental-and global-scale full-waveform inversion in the time–frequency domain: Geophysical Journal International, **175**, no. 2, 665–685.

Fichtner, A., 2010, Full seismic waveform modelling and inversion: Springer Science & Business Media.

Gardner, G., Harris, M., , et al., 1968, Velocity and attenuation of elastic waves in sands: SPWLA 9th Annual Logging Symposium, SPWLA 9th Annual Logging Symposium.

Gardner, G., Gardner, L., and Gregory, A., 1974, Formation velocity and density—the diagnostic basics for stratigraphic traps: Geophysics, **39**, no. 6, 770–780.

Garg, A., and Verschuur, D., 2020, From surface seismic data to reservoir elastic parameters using a full-wavefield redatuming approach: Geophysical Journal International, **221**, no. 1, 115–128.

Grana, D., and Della Rossa, E., 2010, Probabilistic petrophysical-properties estimation integrating statistical rock physics with seismic inversion: Geophysics, **75**, no. 3, O21–O37.

Gray, S. H., and Bleistein, N., 2009, True-amplitude gaussian-beam migration: Geophysics, **74**, no. 2, S11–S23.

Guo, Q., and Alkhalifah, T., 2019, Target-oriented inversion with least-squares waveform redatuming: SEG Technical Program Expanded Abstracts 2019, 1521–1525.

Harding, T., and Lowell, J. D., 1979, Structural styles, their plate-tectonic habitats, and hydrocarbon traps in petroleum provinces: AAPG bulletin, **63**, no. 7, 1016–1058.

Jaglan, H., Qayyum, F., and Hélène, H., 2015, Unconventional seismic attributes for fracture characterization: First Break, **33**, no. 3.

Kaelin, B., and Guitton, A., 2006, Imaging condition for reverse time migration: SEG Technical Program Expanded Abstracts 2006, 2594–2598.

Kelley, C. T., 1999, Iterative methods for optimization: SIAM.

Kuehl, H., and Sacchi, M., 2002, Robust avp estimation using least-squares wave-equation migration: SEG Technical Program Expanded Abstracts 2002, 281–284.

Kühl, H., and Sacchi, M. D., 2003, Least-squares wave-equation migration for avp/ava inversion: Geophysics, **68**, no. 1, 262–273.

Liu, H., and Luo, Y., 2020, Making true amplitude angle domain common image gathers using invertible radon transform: COMMUNICATIONS IN COMPUTATIONAL PHYSICS, **28**, no. 1, 128–140.

Lumley, D., 2010, 4d seismic monitoring of co 2 sequestration: The Leading Edge, **29**, no. 2, 150–155.

Mah, M., and Schmitt, D. R., 2003, Determination of the complete elastic stiffnesses from ultrasonic phase velocity measurements: Journal of Geophysical Research: Solid Earth, **108**, no. B1, ECV–6.

Martin, G. S., Wiley, R., and Marfurt, K. J., 2006, Marmousi2: An elastic upgrade for marmousi: The leading edge, **25**, no. 2, 156–166.

Mazzotti, A., 1990, Prestack amplitude analysis methodology and application to seismic bright spots in the po valley, italy: Geophysics, **55**, no. 2, 157–166.

Minson, S. E., and Dreger, D. S., 2008, Stable inversions for complete moment tensors: Geophysical Journal International, **174**, no. 2, 585–592.

Moczo, P., Kristek, J., Vavrycuk, V., Archuleta, R. J., and Halada, L., 2002, 3d heterogeneous staggered-grid finite-difference modeling of seismic motion with volume harmonic and arithmetic averaging of elastic moduli and densities: Bulletin of the Seismological Society of America, **92**, no. 8, 3042–3066.

Muerdter, D., and Ratcliff, D., 2001a, Understanding subsalt illumination through ray-trace modeling, part 1: Simple 2-d salt models: The Leading Edge, **20**, no. 6, 578–594.

——— 2001b, Understanding subsalt illumination through ray-trace modeling, part 3: Salt ridges and furrows, and the impact of acquisition orientation: The Leading Edge, **20**, no. 8, 803–816.

Mulder, W. A., and Plessix, R.-E., 2004, A comparison between one-way and two-way wave-equation migration: Geophysics, **69**, no. 6, 1491–1504.

Mulder, W. A., 2005, Rigorous redatuming: Geophysical Journal International, **161**, no. 2, 401–415.

Murray, G. E., 1966, Salt structures of gulf of mexico basin—a review: AAPG Bulletin, **50**, no. 3, 439–478.

Nocedal, J., and Wright, S., 2006, Numerical optimization: Springer Science & Business Media.

Ødegaard, E., and Avseth, P., 2003, Interpretation of elastic inversion results using rock physics templates: 65th EAGE Conference & Exhibition, 65th EAGE Conference & Exhibition, cp–6.

Operto, S., Gholami, Y., Prieux, V., Ribodetti, A., Brossier, R., Metivier, L., and Virieux, J., 2013, A guided tour of multiparameter full-waveform inversion with multicomponent data: From theory to practice: The Leading Edge, **32**, no. 9, 1040–1054.

Østmo, S., Mulder, W., and Plessix, R.-E., 2002, Finite-difference iterative migration by linearized waveform inversion in the frequency domain: SEG Technical Program Expanded Abstracts 2002, 1384–1387.

Prucha, M. L., and Biondi, B. L., 2002, Subsalt event regularization with steering filters: SEG Technical Program Expanded Abstracts 2002, 1176–1179.

Ravasi, M., 2017, Rayleigh-marchenko redatuming for target-oriented, true-amplitude imaging: Geophysics, **82**, no. 6, S439–S452.

Richard, V., Rocca, F., Bernasconi, G., De Nicolao, A., Drufuca, J., Lambaré, G., Spagnolini, U., Mazzotti, A., Mélis, A., Ravagnan, G., , et al., 1994, Seismic inversion and the impact of a priori information: Advanced geophysical modeling and inversion unification (agu): Final report of the geoscience project jouf-0037: Modeling the Earth for Oil Exploration, 525–636.

Rickett, J. E., and Sava, P. C., 2002, Offset and angle-domain common image-point gathers for shot-profile migration: Geophysics, **67**, no. 3, 883–889.

Robertsson, J. O., 1996, A numerical free-surface condition for elastic/viscoelastic finite-difference modeling in the presence of topography: Geophysics, **61**, no. 6, 1921–1934.

Ronen, J., 1987, Wave-equation trace interpolation: Geophysics, **52**, no. 7, 973–984.

Sava, P., and Biondi, B., 2004, Wave-equation migration velocity analysis. i. theory: Geophysical Prospecting, **52**, no. 6, 593–606.

Sava, P. C., and Fomel, S., 2003, Angle-domain common-image gathers by wavefield continuation methods: Geophysics, **68**, no. 3, 1065–1074.

Schalkwijk, K., Wapenaar, C., and Verschuur, D., 1999, Application of two-step decomposition to multicomponent ocean-bottom data: Theory and case study: Journal of seismic exploration zzzzzz 0963-0651, 8, 261–278: Web of Science.

Schleicher, J., Tygel, M., and Hubral, P., 1993, 3-d true-amplitude finite-offset migration: Geophysics, **58**, no. 8, 1112–1126.

Schuster, G. T., and Zhou, M., 2006, A theoretical overview of model-based and correlation-based redatuming methods: Geophysics, **71**, no. 4, SI103–SI110.

Shen, P., 2005, Wave equation migration velocity analysis by differential semblance optimization: Ph.D. thesis, Rice University.

Shen, X., 2010, Near-surface velocity estimation by weighted early-arrival waveform inversion: SEG Technical Program Expanded Abstracts 2010, 1975–1979.

Song, Z.-M., Williamson, P. R., and Pratt, R. G., 1995, Frequency-domain acoustic-wave modeling and inversion of crosshole data: Part ii—inversion method, synthetic experiments and real-data results: Geophysics, **60**, no. 3, 796–809.

Stewart, S., 2006, Implications of passive salt diapir kinematics for reservoir segmentation by radial and concentric faults: Marine and petroleum geology, **23**, no. 8, 843–853.

Symes, W., and Carazzone, J. J., 1991, Velocity inversion by differential semblance optimization: Geophysics, **56**, no. 5, 654–663.

Symes, W. W., and Kern, M., 1994, Inversion of reflection seismograms by differential semblance analysis: Algorithm structure and synthetic examples: Geophysical Prospecting, **42**, no. 6, 565–614.

Symes, W. W., 2008, Approximate linearized inversion by optimal scaling of prestack depth migration: Geophysics, **73**, no. 2, R23–R35.

Tarantola, A., 1984, Inversion of seismic reflection data in the acoustic approximation: Geophysics, **49**, no. 8, 1259–1266.

Thompson, L., and Oftebro, C., 2011, Salt gets in your eyes: the geological challenges and solutions to sub-salt exploration: First break, **29**, no. 3.

Tiapkina, O., Voitsytski, Z., Sydorenko, G., and Parkhomenko, T., 2008, Imaging and mapping of hydrocarbon traps in areas of complex salt tectonics in ukraine-case studies: 70th EAGE Conference and Exhibition incorporating SPE EUROPEC 2008, 70th EAGE Conference and Exhibition incorporating SPE EUROPEC 2008, cp–40.

Virieux, J., and Operto, S., 2009, An overview of full-waveform inversion in exploration geophysics: Geophysics, **74**, no. 6, WCC1–WCC26.

Virieux, J., 1986, P-sv wave propagation in heterogeneous media: Velocity-stress finite-difference method: Geophysics, **51**, no. 4, 889–901.

Wang, J., Kuehl, H., and Sacchi, M. D., 2005, High-resolution wave-equation ava imaging: Algorithm and tests with a data set from the western canadian sedimentary basin: Geophysics, **70**, no. 5, S91–S99.

Wapenaar, C., Cox, H., and Berkhout, A., 1992, Elastic redatuming of multicomponent seismic data 1: Geophysical prospecting, **40**, no. 4, 465–482.

Wapenaar, C. P. A., 2014, Elastic wave field extrapolation: Redatuming of single-and multi-component seismic data: Elsevier.

Watson, L. M., Werpers, J., and Dunham, E. M., 2019, What controls the initial peak of an air-gun source signature?: Geophysics, **84**, no. 2, P27–P45.

Williamson, P. R., and Worthington, M., 1993, Resolution limits in ray tomography due to wave behavior: Numerical experiments: Geophysics, **58**, no. 5, 727–735.

Woodward, M. J., 1992, Wave-equation tomography: Geophysics, **57**, no. 1, 15–26.

Yang, T., and Sava, P., 2009, Wave-equation migration velocity analysis using extended images: SEG Technical Program Expanded Abstracts 2009, 3715–3719.

Yilmaz, Ö., 2001, Seismic data analysis:, volume 1 Society of exploration geophysicists Tulsa, OK.

Zong, J., Stewart, R. R., Dyaur, N., and Myers, M. T., 2015, Elastic properties of rock salt: Lab measurements and well log analysis in the gulf of mexico: SEG Technical Program Expanded Abstracts 2015, 3095–3099.